Secondary phase selection during solidification of Mg-Y-Gd alloys.

Doctoral Thesis
(Dissertation)

To be awarded the degree
Doctor of Engineering (Dr. –Ing.)

Submitted by

Gábor Szakács Physicist-engineer
From Miskolc, Hungary

Approved by the Faculty of Natural and Materials Science,
Clausthal University of Technology

Date of oral examination
11. July 2019

Dean:

Prof. Dr. -Ing. habil Karl-Heinz Spitzer

Chairman of the examination board:

Prof. Dr. Ing. Dieter Meiners

Supervising tutor:

apl. Prof. Dr.-Ing. Rainer Schmid-Fetzer

Reviewer:

Prof. Dr.-Ing. Karl Ulrich Kainer, Helmholtz-Zentrum Geesthacht

Acknowledgements

I am greatly thankful for the technical and scientific support from all colleagues at Helmholtz-Zentrum Geesthacht.

Firstly, I would like to thank my supervisor Dr.-Ing. Norbert Hort, for giving me the opportunity to work on this topic, as well as for the guidance, helpful discussions and patient encouragement throughout my PhD and even after leaving the institute for another work opportunity.

The European Union FP7-PEOPLE-ITN-2011 program under REA Grant Agreement No 289163: MagnIM project for financial support, which provided me the financial background during my doctoral project.

Many people contributed to my doctoral thesis over the last three years. Especially, I would like to thank:

- My reviewers, Prof. Dr.-Ing. Rainer Schmid-Fetzer at TU Clausthal (Institute of Metallurgy - Thermochemistry & microkinetics) and Prof. Dr.-Ing. Karl Ulrich Kainer Magnesium at Helmholtz Zentrum (Innovation Center MagIC) to supporting me in my doctoral thesis.
- My former colleague from HZG-MagIC: Dr. Chamini L. Mendis for co-reviewing the thesis, as well as for her comment, guidance, support and motivation. Her contribution was essential to shape a thesis out from the several years long common work.
- My former colleague from HZG-MagIC and friend already from University: Dr. Domonkos Tolnai for teaching and introducing to me the major applied techniques for my thesis work, as well as for his comments, guidance and support.
- Prof. Dr. Regine Willumeit Römer for support guidance during and after the MagnIM project in which she was the leader and coordinator.
- Dr. Hajo Deringa from HZG-MagIC for support, guidance and even offering an extension and being my leader
- My former office mate and colleague at HZG: Dr. Björn Wiese, with whom I shared several workloads and education during my doctor candidate time.

- My co-workers in project MagnIM for the fruitful discussions and memorable meetings and travels: Maria Costantino, Andrea Gil Santos, Nezha Agha, Silvia Galli, Francesca Cecchinato, Marian Vlcek, Sepideh Mostofi, Inigo Marco, Sriveena Srinivasaiah, Anastasia Myrissa and Olga Charyeva
- Colleagues for reviewing my thesis: Dr. Sarkis Gavras and Dr. Franchesco D´Elia.
- Colleagues: Martin Wolff, GertWiese, Petra Fischer, Günter Meister and Alexander Reichart, for all help in the labs.
- Cesar Augusto Stüpp, Ricardo Buzolin, Dr. Marta Mohedano, for the nice time and cooperation in the Helmholtz-Zentrum Geesthacht.
- Former University friend and colleagues for some couple of fruitful discussion and support in hard times: Dr. Rimaszéki Gergö, Dr. Grega Oszkár, Dr. Svidro Péter, Dr. Fekete Tamás.

I want to acknowledge the Deutsches Elektronen-Synchrotron (DESY) for the provision of synchrotron radiation facilities within the framework of three proposals at the PETRA III.

Proposals No. at DESY:

• I-20120627

• I-20130434

However, on my way to this thesis, I got great amount of support from the professional side, but it could not reach the final shape without some non-scientific friends.

First and foremost, I would like acknowledge the Severnyák family from Geesthacht. Without their support and help in tough times in my life I could not be write my thesis. The support of other friends from home: Mariann Pozsonyi, Balázs Mang, András Huszár, Ádám Tóth, Dániel Fátay was also essential.

Last but not least, I would like to gratefully thank to my entire family. Without their support, I would not have come this far:

Anya, Apa, tesó, kersztanya, unitesók! Amint kezemben a papír végre, együtt iszunk majd mindannyiunk egészségére!!!

Nagyon szépen Köszönöm!!!

1 Introduction

After refinement of pure metal from metal ore, the first production step for magnesium is casting in which the molten metal solidifies into solid. The majority of the industrial application of magnesium alloys are in the form of castings, especially die castings [1, 2] Consequently their microstructure and their macroscopic mechanical properties are determined during solidification. The general solidification characteristics of magnesium alloys such as fluidity, lower susceptibility to hydrogen porosity and the much less affinity to iron (steel tools and devices) makes it more cast able compared to aluminium [3]. However, the additional costs of production such as melt protection, prize and availability of material and overall lower ultimate property profile of magnesium makes it less desirable than aluminium for wider range of application. Consequently, the amount of invested money into development and research on magnesium and its alloys have been also more limited, which resulted in a lack of proper information even in promising alloy systems such as Mg-RE alloys.

However, knowing the solidification mechanisms applicable for the chosen process path is necessary to control the microstructure formation and the resulting mechanical properties. In this study the major focus was on the sequence of phase formation during the solidification of Mg-15RE alloys (RE is rare earth elements) with the combined addition of gadolinium and yttrium where the total alloying additions were equal 15wt.%. Determine the role of cooling rate on the solidification behaviour of the ternary alloys and study the effect Gd/Y ratio on the forming intermetallic phases. The equilibrium thermodynamics provide some clues as to the phase fractions expected but the experimental investigations of solidification of these alloys show that equilibrium thermodynamics do not completely illustrate the microstructure and phase evolution observed during the casting process. However, the general method is to collect properties and microstructural information from cast or quenched stages (ex-situ) of observed phase transformations. In complex alloys the outcome cannot be explained only from these stages. Thus, obtaining information during dynamic studies would often be more appropriate. The continuous development of the X-ray acquisition systems at synchrotron sources provides a unique tool to characterize the phase formation and evolution during solidification in situ. Therefore, in situ

solidification experiments conducted with synchrotron radiation X-ray diffraction were utilised to follow the microstructural evolution of alloys from the Mg-Y-Gd system during simulated casting conditions. Thus, this method can gives the opportunity to optimize even process routes of investigated alloys in order to achieve the desired microstructure and property profile of a product for a wide range of applications. The experimental findings are going to be correlated thermodynamically assessments using equilibrium condition and Scheil-model for solidification.

2 Literature Review

2.1 Solidification

In the last decade of the 20th century 98% of the magnesium components were produced in the form of castings [4]. Therefore, the desired final properties of the product has to be achieved during the solidification. The general solidification characteristics of magnesium alloys such as fluidity, lower susceptibility to hydrogen porosity and the much less affinity to iron (steel tools and devices) makes it more cast able compared to aluminium [3]. However, the required melt protection, prize of production and the overall delivered ultimate property profile of magnesium still keep aluminium more attractive to industrial applications [2]. Consequently, the amount of invested money into development and research on magnesium and its alloys have been also more limited, which resulted in a lack of proper information even in promising alloy systems such as Mg-RE alloys. In this chapter the phase transformation and solidification theory will be discussed generally as well as with specific references to magnesium.

2.1.1 Casting of magnesium

Casting is the first step in the process path for producing any metallic part used in industrial settings today. Casting is purely a solidification process, which means the solidification phenomenon controls most of the properties of the final casting and all casting defects, as gas porosity and solidification shrinkage [5]. As already mentioned, casting is the major production path for magnesium products. The magnesium melt is more reactive compared to that of steel or aluminium, therefore casting facilities have to ensure proper melt protection. The possible melt protections are either flux process or protective gases [1, 4]. The most common casting processes with magnesium are:

- gravity casting (sand, permanent mould),
- pressure die casting: high (HPDC),
- low pressure die-casting,

- thixomolding,
- squeeze casting,
- permanent mould direct chill casting (PMDCC).

Generally, the major difference between casting techniques is the cooling rate, which is important for the subject of this study. During this study cooling rates of 20 and 100 K/min used to understand the effect of changing the cooling rate has on the phase evolution in different parts of a cast component. These cooling rates represents mainly: the sand or gravity casting methods.

2.1.2 Thermodynamics associated with solidification

Thermodynamics describes equilibrium states of a system as well as transitions from one equilibrium state to another. In the matter of solidification, a thermodynamic transition is described in which solid phase or phases are forming from liquid. The system can be explained by state variables, like: the number of components (***N***), the temperature (***T***), the pressure (***p***) and the volume (***V***) [5]. Applying the first and second law of the thermodynamics the system state extensive variables such as the enthalpy (***H***), entropy (***S***) or the Gibbs free energy (***G***) could be determined using the thermodynamic variables. These variables are allow us to determine property and phase diagrams. Phase diagrams are maps of equilibrium conditions, and they are considered as one of the most powerful tools for studying the development of microstructure. However they do not include kinetic effects (factors), for instance the nucleation undercooling and /or growth undercooling observed in practical solidification, but the equilibrium phase diagrams are indispensable to understand off equilibrium processes either [6]. Alloys are a mixture of more than one element, but their diagrams validated for constant pressure, therefore the state variables are: T and N. At particular state points the agglomeration of different atoms in the system may arrange themselves in various phases such as liquid, gas, varying type of crystal structures or in a combination of phases. In multiple phase regions the diagram provides the information about the existing equilibrium phases at each points and their ratio can be also determined by Lever rule. If the Lever rule is used to simulate a solidification, it assumes that diffusion is fast enough both in solid and liquid phase to reach immediate equilibrium state. That is the compositions of the solid and liquid become equals of the composition of the solidus

and liquids curves respectively. As a result of the model we can determine the final microstructures directly from the diagram. However, it often does not reflect the phases actually observed in the as-cast state of the alloys. This distinction is more pronounced if the appearing solid phases exhibit wide range of solid solubility and if solid state diffusion is relatively slow compared to the solidification rate. For non-equilibrium solidification the Scheil approximation is used widely as a much better description. It is often called the Scheil-Gulliver approximation, since the earlier contributor was Gulliver without giving explicit equation in his description [7]. In essence, Scheil–Gulliver model assumes no diffusion occurs in solid phase but perfect mixing (theoretically infinite diffusivity) in the liquid phase; so that liquid composition would always follow liquidus temperature as depicted by the equilibrium phase diagram, whereas solid composition would be less than the equilibrium solidus [8]. In reality, however, one would expect diffusion to take place both in solid and liquid phases; but generally the diffusion is several order of magnitude slower in solid phase than in liquid, which means more time is required to reach the equilibrium state. Consequently, the cooling rate, which determines the time available for the solidification, has the major impact on the decision whether the solidification process is close to equilibrium (Lever) or far from it (Scheil).

2.1.3 Nucleation

The solidification process starts with the creation of clusters of atoms of crystalline structure due to the random nucleation. These clusters are initially called embryos, whereas those that are sufficiently large to be stable are termed nuclei. In order to create these nuclei, the molten phase must be undercooled below the freezing temperature. The homogenous nucleation is based on a spontaneous appearance of the nuclei in the melt, and the conditions of the formation can be calculated by the change of the free energy (***ΔG***) of the system:

$$\Delta G = -V_S \Delta G_V + A_{SL} \cdot \gamma_{SL}$$

Where $\boldsymbol{V_s}$ is the volume of the forming solid phase, $\boldsymbol{G_v}$ is the Gibbs energy reduction, $\boldsymbol{A_{SL}}$ is the surface of the new phase with a $\boldsymbol{\gamma_{SL}}$ surface energy between solid and liquid phase. If we consider the nuclei as a sphere with a radius ***r***:

$$\Delta G_r = -\frac{4}{3}\pi r^3 \Delta G_V + 4\pi r^2 \gamma_{SL}$$

The equation is illustrated on Figure 1, with the separation of the two portions of the equation: interfacial- and volume free energy. The maximum point of the Gibbs free energy (ΔG*) provides the critical nuclei radius of the system. Any nuclei which have radii greater than r* it will grow as it results in a continuous Gibbs potential drop. However, those which are smaller than r*are embryos and do not participate in grain growth.

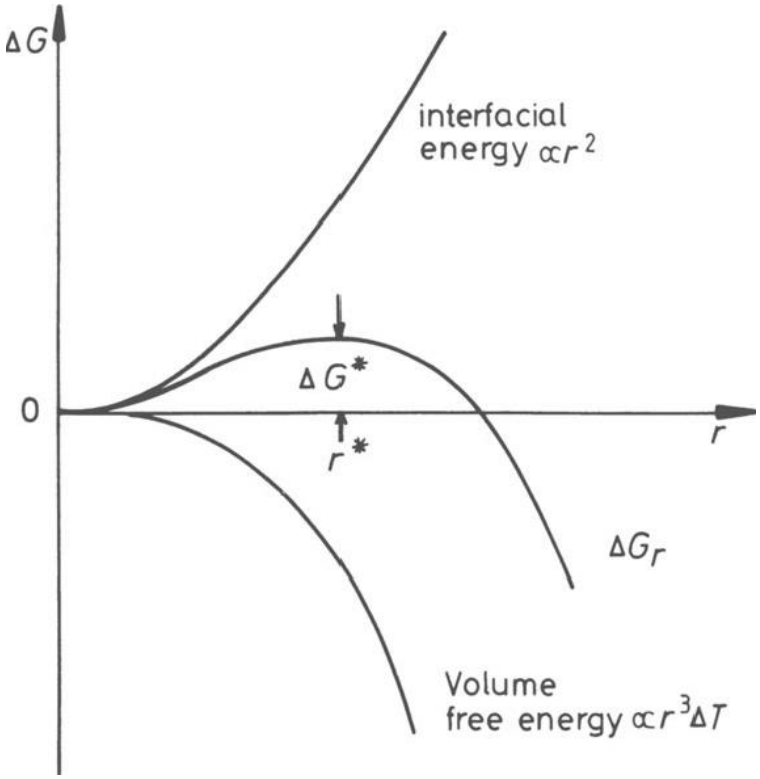

Figure 1. The free energy change in homogenous nucleation of a sphere of radius r [8].

The function has a local maximum at the critical radius, thus the differentiation of the function ($\frac{\mathbf{dG}}{\mathbf{dr}} = \mathbf{0}$) will allow as to determine ***r**** as:

$$r^* = \frac{2\gamma_{SL}}{\Delta G_V}$$

and $\boldsymbol{\Delta G^*}$ as:

$$\Delta G^* = \frac{16\pi\gamma_{SL}^3}{3 \cdot \Delta G_V{}^2}$$

The $\boldsymbol{\Delta G_v}$ can be estimated as a function of the system ΔT ($T\text{-}T_m$) undercooling:

$$\Delta G_V = \frac{L_V \cdot \Delta T}{T_m}$$

which allows to determine $\boldsymbol{r^*}$ and $\boldsymbol{\Delta G^*}$ as a function of the undercooling:

$$r^* = \left(\frac{2\gamma_{SL}T_m}{L_V}\right) \cdot \frac{1}{\Delta T}$$

and

$$\Delta G^* = \left(\frac{16\pi \cdot \gamma_{SL}^3 \cdot T_m^2}{3L_V^2}\right) \cdot \frac{1}{\Delta T^2}$$

Homogenous nucleation is a simple and accurate description of the solidification process itself, but typically heterogeneous nucleation takes place. During heterogeneous nucleation the nuclei form on a foreign particle or surface. The basic principle is the same, but the boundary conditions (nuclei is just a spherical cap) allows the formation of nuclei with a far smaller critical $\boldsymbol{\Delta G^*}$ (Figure 2). Thus, it requires a much smaller undercooling of the system. Consequently, the probability of heterogeneous nucleation is far greater than homogenous. However, it is much more dependent on the balance of the surface energies. The nuclei this case has common surface with the foreign particle and the liquid and there is surface energy between liquid and the foreign particle as well. If the surface energy between the surface, nuclei and liquid allows a contact angel $\Theta<90°$, the wetting conditions are favourable to initiate heterogeneous nucleation. Surface energy is highly

dependent on local chemistry (concentration) which can have a high fluctuation inside the melt due to diffusion and convection (kinetics) and alter solidification behaviour significantly.

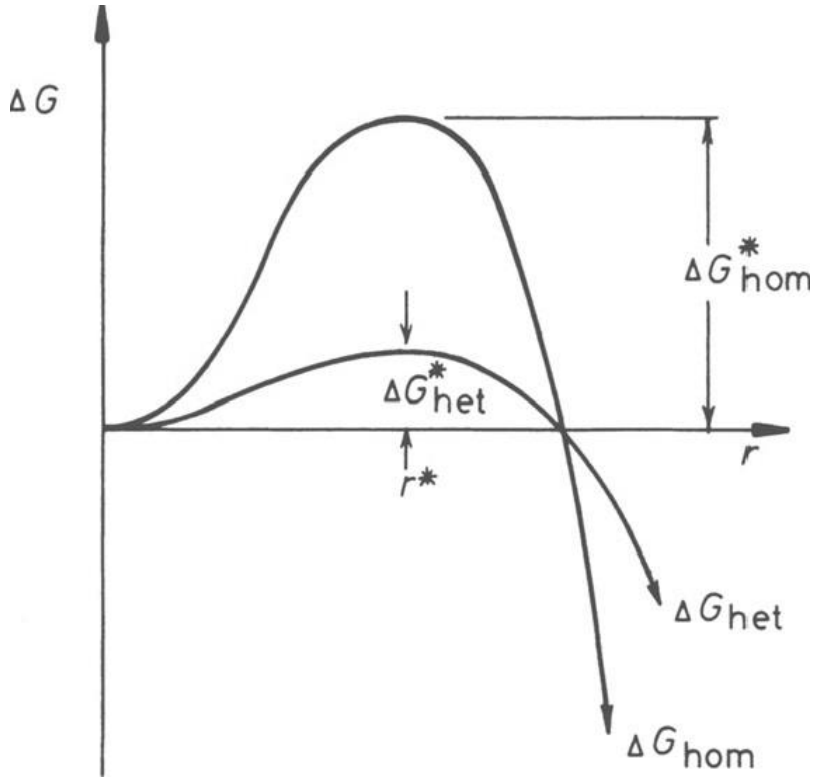

Figure 2. The excess Gibbs energy of solid clusters for homogenous and heterogeneous nucleation. Note r* is independent of the nucleation site [8].

2.1.4 Secondary phase selection

The secondary-phase selection during solidification and phase evaluation is a crucial factor that determines the microstructure of the cast product and consequently the mechanical property profiles. The presence of a phase in the microstructure depends on two main factors: thermodynamic stability and surface energy of the phases. The free energy change (***ΔG***) for a phase transformation can be summarized (based on the theory of nucleation) by the following equation [8]:

$$\Delta G = -V\Delta G_v + A \cdot \gamma + V\Delta G_s$$

Where $\boldsymbol{V}$ is the volume of the newly forming phase, $\boldsymbol{G_v}$ is the Gibbs energy reduction, $\boldsymbol{A}$ is the surface area of the new phase with a $\boldsymbol{\gamma}$ surface energy. Unfortunately, the ability to predict a phase transformation is limited as there is a lack of interfacial energy data for the formation of secondary phases and their relationship with the matrix [9]. Thus, the interfacial energies have a crucial role in the secondary phase selection during solidification.

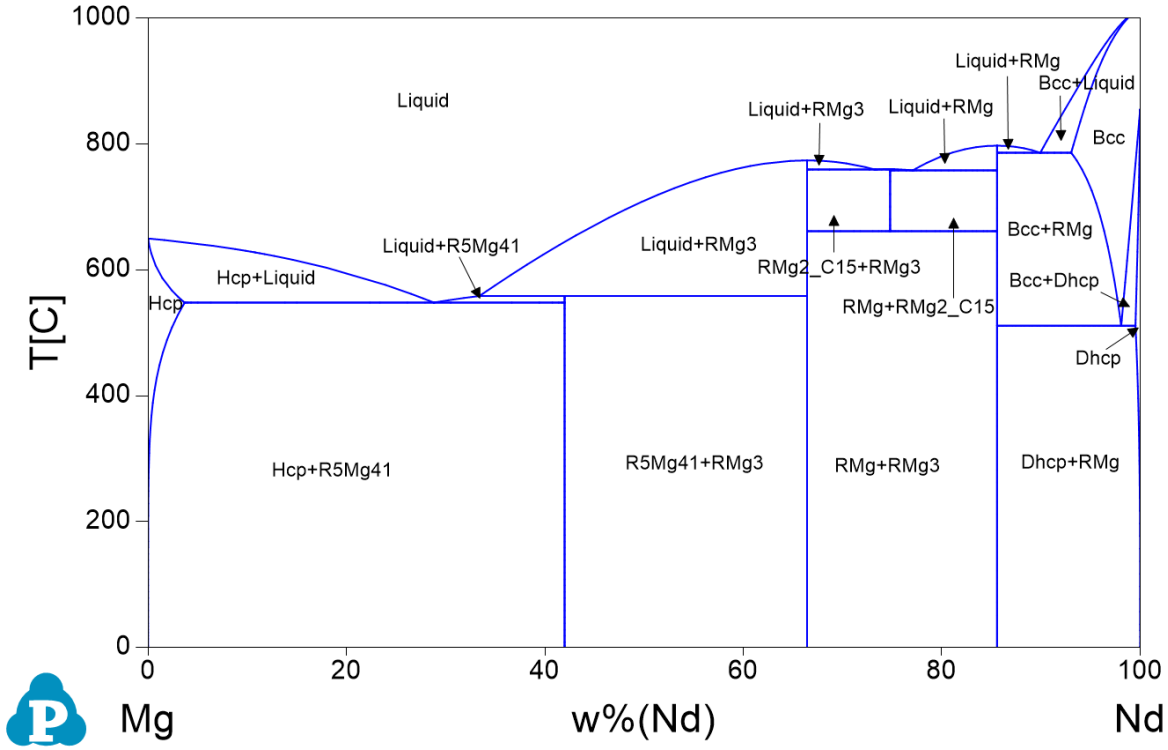

Figure 3. Binary phase diagram of Magnesium Neodymium [10].

Excellent example of the secondary phase selection dependency on the thermodynamics, structure selection and interfacial energy is the hypoeutectic alloys of the Mg-Nd binary system (Figure 3). It has been reported that the as cast binary alloys tend to form the $NdMg_{12}$ (tetragonal, tI26 $ThMn_{12}$ type [11]) phase at relatively slow cooling rates (sand castings) [12] or the $NdMg_3$ (cubic, cF16 BiF_3 type [11]) phase with more rapid cooling (high pressure die casting) [13].The thermodynamically stable intermetallic phase is Nd_5Mg_{41} (tetragonal, tI92 Ce_5Mg_{41} type [11]) which appears heat treatments [7, 8]. When Gd is added into the system (Mg-2.7Nd-1.2Gd wt%)

even the slow cooling rate forms RMg_3 (cubic, cF16 BiF_3 type [11]) phase and $Mg_{12}Nd$ type phases are not detected [14].

According to thermodynamic assessments, the energetically favourable phases have always lower undercooling, however thermodynamic calculations do not account for kinetics or lattice mismatches. Lattice mismatch affects the surface energy and thus phase transformation, is the lattice matching between the phases during solidification both solidification [8]. The Edge to Edge matching (E2EM) approach [15, 16] has been successfully applied recently to match planes and directions, the orientation relationship (OR) between phases to be identified and understanding or predicting the crystallographic features between adjacent crystalline phases [17]. The major parameters of the approach are:

- interatomic spacing misfit: $\boldsymbol{f_r}$,
- interplanar spacing mismatch: $\boldsymbol{f_d}$.

Using this approach in cooperation with thermodynamic calculation Easton et al [18] revealed the most logical reason for the variation in the intermetallic phase formation in the Mg-Nd system. The thermodynamic calculations expect the stable Nd_5Mg_{41} secondary phase formation at the equilibrium eutectic temperature of the system: 547.4 °C. If the phase formation is suppressed, $NdMg_{12}$ phase formation is expected at 541.8 °C with an undercooling ($\boldsymbol{\Delta T}$) of at least 5.6°C. However, if both phases are suppressed the $NdMg_3$ phase formation is expected at 533°C ($\boldsymbol{\Delta T}$=13.9°C). On the contrary, the E2EM method declared that $NdMg_3$ (fcc lattice, a=0.7399 nm) phase four possible OR with less than 10 % interatomic spacing misfit ($\boldsymbol{f_r}$), with the best one ($[\bar{1}2\bar{1}3]_{Mg}\|[31\bar{1}]_{NdMg3}$) being <0.5% which has an $\boldsymbol{f_d}$<0.5% as well. $NdMg_{12}$ (body-centered tetragonal (bct), a=b=1.031nm, c=0.593nm) has only one OR with $\boldsymbol{f_r}$<10% (~8.2%), while Nd_5Mg_{41} (bct, a=b=1.4741nm, c=1.0396nm) has none. The model predicts an incoherent high energy interface. The predicted ORs are in good agreement with previous work and explain the frequent appearance of the RMg_3 phase (fcc, BiF_3 type) in Mg alloys with faster cooling rates.

2.1.5 Techniques for understanding solidification

The experimental methods for measuring solidification paths are many, however those that investigate the microstructure development during solidification are limited. Thermo-analytical techniques are in one group, where differential scanning calorimetry (DSC) is one of the most used techniques, In DSC measurements the difference in the amount of heat required to change the temperature of a sample and reference is measured as a function of temperature. Both the sample and reference are maintained at nearly the same temperature throughout the experiment. Generally, the temperature program for a DSC analysis is designed such that the sample holder temperature increases linearly as a function of time. The reference sample should have a well-defined heat capacity over the range of temperatures to be scanned. The technique gives accurate temperature and heat capacity values (can supply data for phase diagrams). The nature of the phase transformation and the microstructural evolution must be investigated *ex situ* on interrupted experimental samples. Microstructure is generally characterized afterward by the combination of microscopy techniques (Light, scanning electron or transmission electron microscopy) and diffraction (explained in details later) methods (X-ray diffraction, transmission electron microscopy diffraction, neutron diffraction). Although DSC methodology is simple, the system has a temperature resolution limit, when investigating kinetics and in complex systems, phase formations and transformations peaks can overlap making it difficult to determine the real sequence of phase evolution.

Recently, the solidification sequences have been studied using *in situ* radiology [19, 20], X ray computed tomography (CT) or diffraction methods. Radiology and CT can reveal how the architecture of the microstructure develops during solidification, while in situ diffraction provides information about the structure of the phases, which evolve and will be discussed in a later section.

2.2 Magnesium

Magnesium was discovered by Sir Humphry Davy in 1808. In the periodic table it is placed in the second member of the alkaline earth metals (group II together with Be, Ca, Sr, Ba and Rd) with the atomic number of 12 and a molar weight of 24.31g [21]. The crystal structure of magnesium is a hexagonal closed packed (HCP) (Figure 4) with a lattice parameter of a=0.32092 nm and c=0.52105 nm [22], its atomic (covalent) radius is 141±7pm ($1.41 \cdot 10^{-12}$ m) [23].

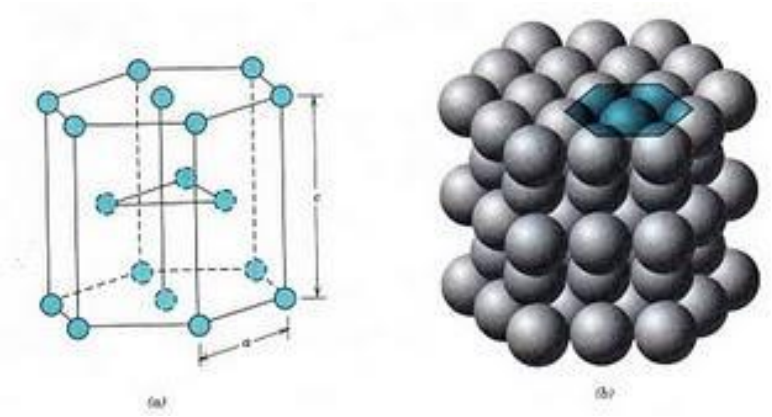

Figure 4. Illustration of a HCP structure [24].

Due to the high reactivity the first applications of the magnesium were fireworks and flashlights. But the low weight (approximately 1/4 the weight of steel and 2/3 the weight of aluminium) and relative ease of access made Mg an interesting structural material for application in automotive and aerospace industries in the early 20th century [25]. Additionally, the first trials of medical applications were already reported in the 19th century [26]. However, Mg alloys still reported to have relatively lower mechanical properties (Table 2-1.) and low corrosion resistance, which are some of the main obstacles that prevent the use of magnesium alloys in wider range of application [25].

Table 2-1. The mechanical properties of Mg and its alloys compare to that of Al alloys and Steel alloys.

Properties	Unit	Magnesium	Aluminium	Steel
Density	g/cm^3	1.74	2.7	7.87
Melting point	°C	650	660	1536
Hardness	HV	30-90	21-120	103
Tensile strength	MPa	98-245	39-570	192-955
Yield strength	MPa	90-230	10-98	98-870
Young modulus	GPa	45	68	206
Crystal Structure		hcp	fcc	bcc/fcc

The higher propensity for corrosion of the magnesium is the result of the high chemical activity of the metal and a non-continuous oxide layer, which is also observed in the molten stage. Therefore protective atmospheres are required during the processes of the magnesium-based alloy which makes the industrial mass production of magnesium products more complicated [27, 28, 29, 30].

Despite the above-mentioned challenges, magnesium and its alloys offer an outstanding specific mechanical property profile and it is 100% recyclable, which makes it more attractive for applications where weight reduction is a key issue. Consequently, several alloys have been already used in weight critical applications. These alloys are mainly the combination of multiple alloying elements such as: aluminium, zinc, manganese, calcium, zirconium or RE [22, 25].

The light weight of the metal is not the only unique feature of Mg for potential application. As an essential element of the human body, magnesium is one of the most if not the most promising material for bio-medical application. Thus, Mg has become even more attractive for biomedical application recently due to complete biodegradability of it with no appreciable toxicity to human physiology [26]. The mechanical properties are suit, along with the corrosion properties points to Mg being a perfect material for the production of temporary implants [26, 31]. Many studies have already reported that Mg-based materials generally show favourable results for toxicity and

inflammation of the host tissue while the degradation products are easily restorable by the body [32, 33].

Even with such high potential for application as a degradable biomaterial, the application ready alloys with optimised process parameters required significant amount of research. Only a few of the investigated alloys can be developed further for intended industrial applications. Unfortunately, in majority of the magnesium alloy development work first requires the development of new thermodynamic databases as the existing data only accurately describe binary phase diagrams and only few systems have developed to include ternary data. However the majority of the magnesium alloys developed currently are based on complex systems have not even been deeply studied yet. One of the most promising group of alloying elements for the development of degradable biomaterials are the Rare Earth (RE) elements.

2.2.1 Magnesium-Rare Earth alloys

The first commercial applications of magnesium alloys with rare earth metals (RE, R) related to the development of light structural materials having high strength both at room and at elevated temperatures. The Mg-RE alloys show the most promise as alloys targeted for structural application (where high temperature oxidation resistance or creep resistance is needed) in automotive or aerospace sectors [34, 35] and more recently for bio-medical application [26, 36]. The numbers of studies on Mg-RE alloys for bio application have exponentially increased recently [37, 38, 39, 40, 41]. Moreover, the first clinical trials on Mg implants has already commenced on Mg-RE based materials [42, 43]. Due to the large atomic size and wide range of solubility in magnesium, RE elements are far more effective for solution strengthening [44, 45] or precipitate hardening [46, 47] than any other industrially used elements (Al, Zn) [48, 49] in Mg alloys. The addition of Y (or Gd) to Mg reported to influence not only the atomic binding states between Y (Gd) and Mg atoms, but also between Mg atoms, resulting in anomalous solid solution strengthening [50]. Mg-RE alloys have received great attention due to their excellent creep resistant at elevated temperatures [51, 52, 53]. The beneficial effect of very small amount of RE on the relatively random texture development in extruded and rolled material makes them desirable addition from the perspective of wrought processing [54, 55]. The magnesium alloys with RE

additions enhance the mechanical properties while they also contribute to the decreased chemical reactivity, which results in a reduced flammability during casting [56, 57, 58] and also resulted in improved corrosion resistance [59, 60]. Mg-RE alloys are also the core of the recent major scientific interest: the formation and evaluation of long periodic stacking order (LPSO) structure and its effect on material properties [61, 62, 63]. This structure would be introduced in Mg-RE alloys via addition of Zn, Cu, Ni or Co.

Originally RE elements were used for alloying magnesium in the form of "mishmetal". This is a mixture of different rare earth metals with a higher concentration of Ce and Nd. RE were considered having the same effect on Mg. Leontis [35, 64] showed significant difference between RE alloys in terms of maximum solid solubility of various elements. Two groups of RE elements has been considered, one with low solubility and another with higher solubility at high temperatures. Recently especially in biomaterials research the work on individual RE addition have different characteristic in the human physiology [35, 65].

2.2.2 The Thermodynamic and Chemical background of Mg-RE systems

The term "rare earth metals" is used to classify the group of chemical elements with atomic number from 57 to 71, but yttrium (39) and scandium (21) are also recommended to be called RE [35, 66]. The rare earth metals are divided into two subgroups. The "cerium subgroup" so called "light" rare earth metals, which includes elements from lanthanum (atomic number 57) up to europium (63). The other one is the "yttrium subgroup" so called heavy rare earth metals and this group includes the rest of the elements, however scandium is not included in any subgroup. The two subgroups differ in the number of valence electrons (Ce: 2, Y: 3), which explains the different alloying behaviour and results wide range of solid solubility of the RE in Mg. The elements of the Ce subgroup (light RE elements) have a low solid solubility while the Y subgroup (heavy RE elements) have a much higher solubility range (except Yb). The solubility changes according to the atomic numbers are presents in Figure 5.

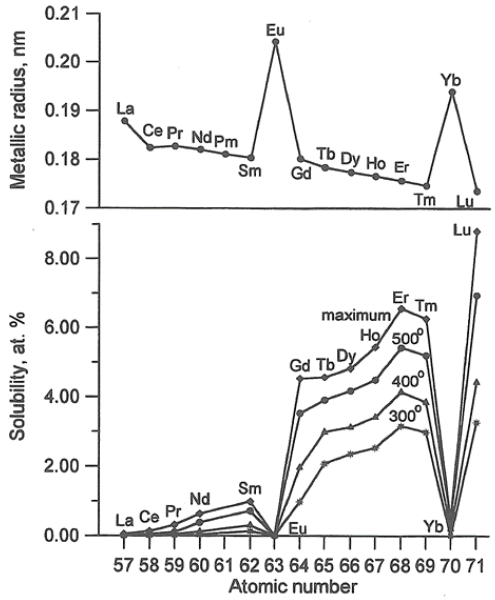

Figure 5. The RE atomic radius (upper) and RE solubility in solid Mg (lower) in function of atomic number [35].

The RE are chemically reactive and tend to form chemical compounds easily including hydrides, fluorides, chlorides, oxides, nitrides, carbides, silicide, salts of organic and inorganic acids, and complex compounds [35, 67, 68]. The formation of RE-hydrides during processing Mg alloys has been reported [69, 70]. Majority of the RE elements are not stable even at room temperature and they oxidise quickly. The properties of magnesium alloys with different RE metals are closely connected with respective binary phase diagrams [35]. Investigation of the binary phase diagrams of magnesium with individual rare earth metals were started in early 20th century continues to today. Rokhlin et al. shows the existence of regularities in the invariant equilibria of the Mg-RE systems with the atomic number of RE addition [71]. The established similarities are quite well known so that an unknown Mg-Re phase diagram might be predicted sufficiently reliably if the phase diagram of the systems with the closest neighbours of that RE had been previously studied. The compound formations of Mg-RE systems are presented in Figure 6.

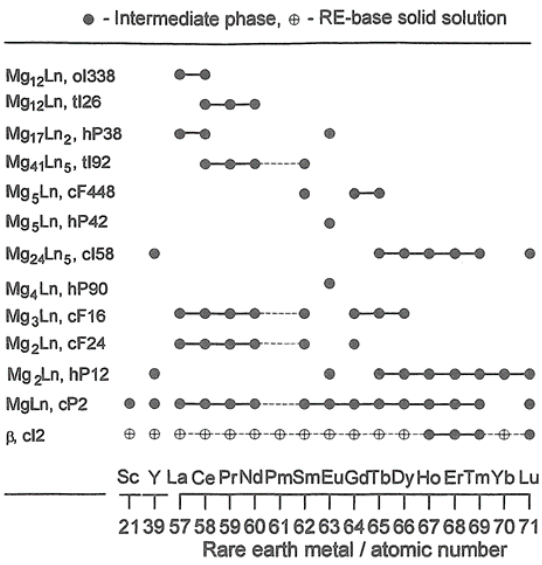

Figure 6. Summary of the intermediate phases formed in the binary Mg-RE systems [35].

The addition of heavy RE i.e. Y, Gd, Dy or combination of these elements allows tailoring the mechanical properties and corrosion behaviour of these alloys through heat treatment [72]. However, in many cases the microstructure evolution of ternary and complex alloys during casting or heat treatment is still known only at rudimentary level. The ternary systems of Mg-RE alloys show three similar features:

1. the mixture of RE element has not been reported to show any new phase formation,
2. two different RE elements show wide range of solubility in one compound,
3. the presence of two RE addition reduces the solid solubility of both in Mg.

2.2.3 Magnesium-Gadolinium

Among RE elements Gd (atomic number 64) shows one of the best biocompatibility [37, 65], and it is currently used safely in medicine as a contrast agent in magnetic resonance imaging [73]. Mg-Gd based alloys are promising candidates for novel precipitation hardened alloys having good creep resistance and specific strength at elevated temperatures, in which the precipitates play an important role in governing the mechanical properties. However, the experimentally observed precipitation sequences during isothermal aging of Mg-Gd based alloys is complex and involve the formation of metastable phases designated β'', β' and β [74, 75, 72]. The proposed sequence [72, 75] consist of Mg super saturated solid solution (SSSS)→β'' ($D0_{19}$ metastable) →β' (c-bco metastable) → β (fcc stable $GdMg_5$). These metastable phases are not presented in the equilibrium phase diagram. These precipitates are able to form during a natural aging even at room temperature with kinetics much slower than observed in complex aluminium alloys [47].

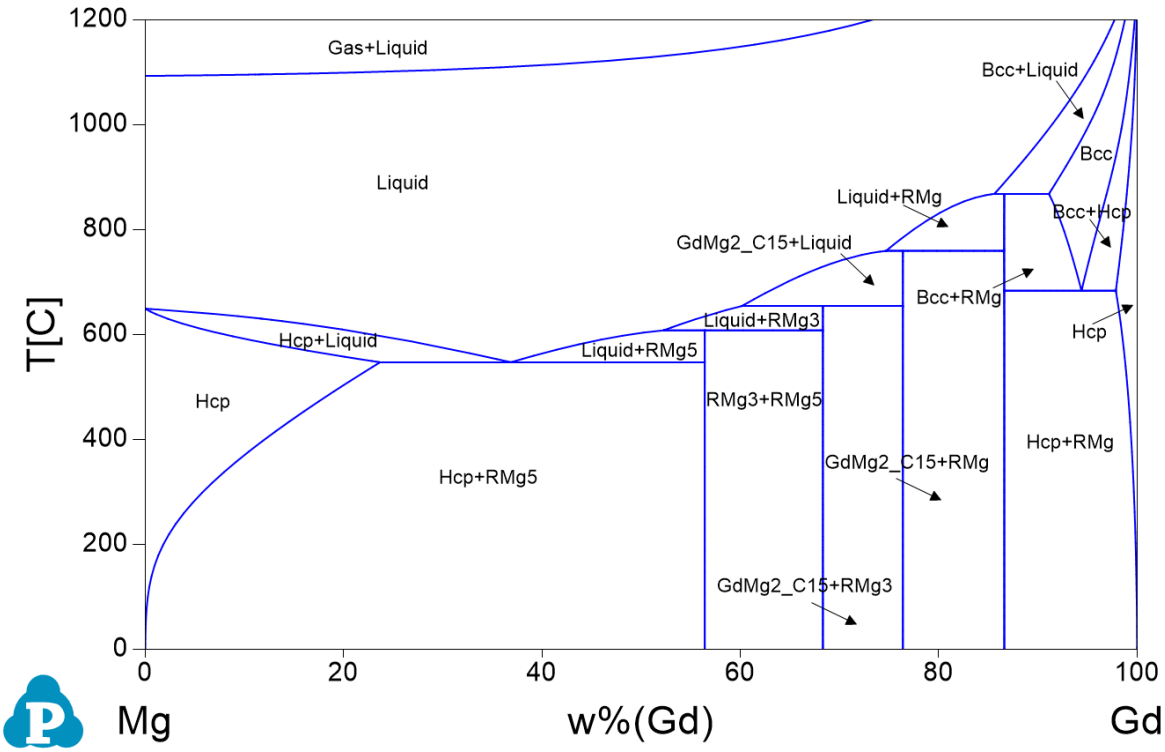

Figure 7. Binary phase diagram of magnesium-gadolinium (Mg-Gd) [10].

Phase equilibria and the thermodynamics of the binary Mg–Gd system have been extensively studied experimentally (Figure 7). The first experimental study of the binary Mg–Gd phase diagram was by Savitskii et al. [76] in 1961 using differential thermal analysis (DTA) and X-ray diffraction (XRD) coupled with hardness and micro hardness measurements. Four intermetallic phases; $GdMg_9$, $GdMg_3$, $GdMg_2$ and GdMg were reported in their investigations. These results were revised by Manfrinetti and Gschneidner [77] who determined the entire phase diagram, utilizing thermal, metallographic and X-ray analysis. Four intermetallic compounds $GdMg_5$ (cF448-$Cd_{45}Sm_{11}$ type, T_{max}= 642°C), $GdMg_3$ (cF16-BiF_3 type, T_{max}= 706°C), $GdMg_2$ (cF24-Cu_2Mg type, T_{max}= 755°C) and GdMg (cP2-CsCl type, T_{max}= 867°C) were observed and all form via a series of peritectic reactions. Each with lower formation temperature than the previous when described from the Gd rich side. Gd has a maximum solubility of 23.49 wt.% (4.53 at.%) at 548 °C in Mg [78] and offers wide range of possibilities to tailor the mechanical properties through controlled thermal profiling as the solid solubility decreased with decrease in the temperature. The amount of diluted Gd in the Mg matrix can change the asymmetry between tension and compression anelastic strain [79]. The original thermodynamic descriptions of the Mg-Gd system wes presented by Cacciamani et al. [80] (based on experimentally determined values by Manfrinetti and Gschneidner [77]) and most recently assessed by Hampl et al. [81]. A new thermodynamic description of Mg-Gd system is available [82] but did not show significant deviation from that predicted by Hample et al.. Although the detailed thermodynamic studies and the available thermodynamic assessments can predict accurately equilibrium conditions, casting experiments always provide unexpected results. Tong et al. reported the presence of MgGd, Mg_2Gd and even α-Gd phases in the segregated areas due to the significant segregation during conventional castings of Mg8Gd alloys due to gravity induced convections [83]. They claim that this is the result of the huge different in melting temperature and atomic weight between Gd and Mg and it can be avoided with the use of ultrasonic treatments of the melt. The probability of the formation of GdH_2 during casting is increased with an increased Gd concentration [70]. These differences cannot be predicted with thermodynamic calculations but can strongly affect the properties of the cast alloy and may have impact on the solidification behaviour.

Table 2-2. Thermodynamically stable phases [77, 81].

Phase (Stable)	Forming T [°C]	Structure	Lattice parameter [nm]
Mg_5Gd	<642	cF448, $Cd_{45}Sm_{11}$ type	a=2.2344
Mg_3Gd	<706	cF16, BiF_3 type	a=0.732
Mg_2Gd	<755	cF24, Cu_2Mg type	a=0.857
MgGd	<867	cP2, CsCl type	a=0.382

2.2.4 Magnesium-Yttrium

Yttrium is the lightest element of the Yttrium subgroup (atomic number 39). Yttrium is already one of the key component for several commercial alloys for aerospace castings application (e.g.:WE43, WE54) which makes it a commercially important additive. It is one of the most effective RE elements to improve mechanical properties of magnesium alloys through solid solution strengthening and precipitate hardening due to the large difference in solid solubility at high (550°C) and intermediate (~200°C) in Mg alloys [44, 84, 85]. However, Mg-Y system does not show the same sequences of precipitation as observed in alloys with other RE elements and it is the most widely used rare-earth alloying element in magnesium alloys to date. The creep rate of Mg-Y solid solution alloys at 550K is three orders of magnitude lower than those of Mg-Al alloys processed under similar conditions [85]. At room temperature the hardness of Mg-Y alloys increases with Y content following the empirical relationship Hv0.5 ($kg \cdot mm^{-2}$) = 31.12 + 13.23·(at.%) [84]. Y has been reported to improve the corrosion resistance of Mg alloy due to its special chemical activity, which has the same standard electro-chemical potential (-2.372 V) to that of Mg. Previous studies found that Y rich zone can induce galvanic corrosion, but in the same time net-Y-rich zone can provide some barrier effect [86]. Others reported that Y based alloys after T4 Heat-treatment induce Y_2O_3 layer on the surface of the samples [87, 88].

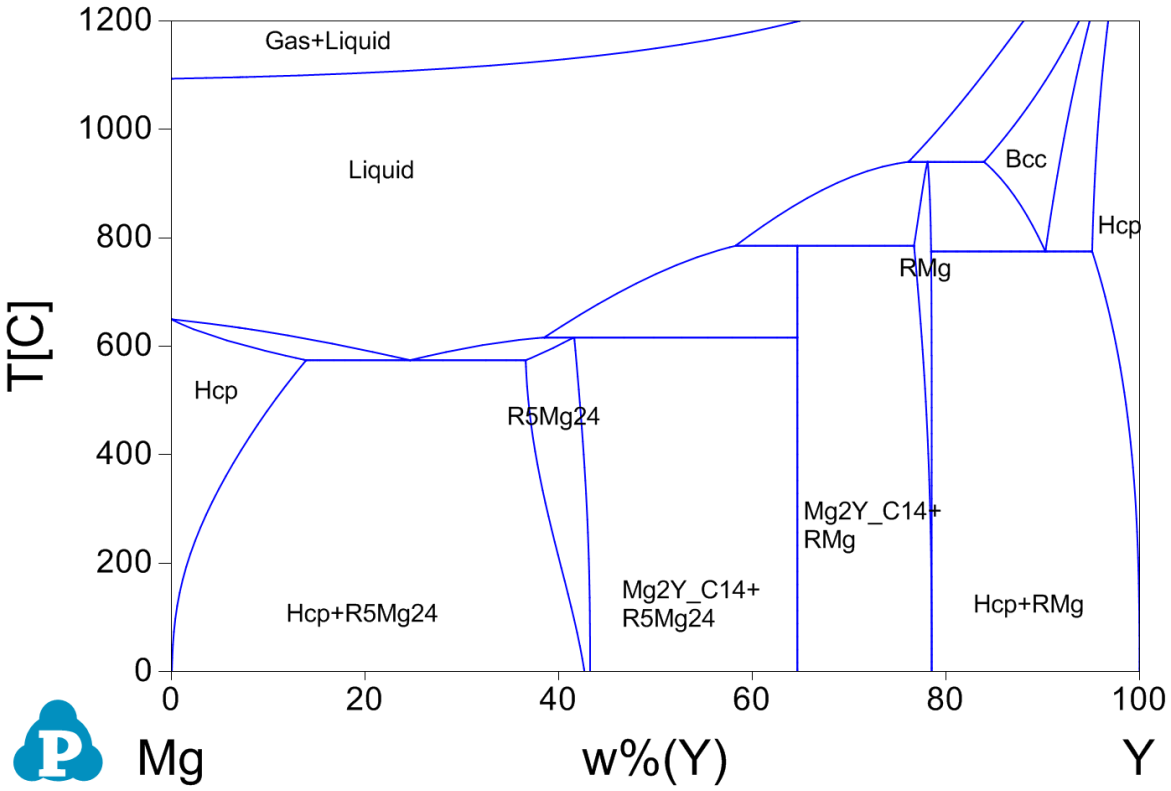

Figure 8. The Mg-Y binary phase diagram [10].

The Mg-Y phase diagram (Figure 8) was first determined Gibson and Carlson [89], then assessed by Nayeb-Hasheimi and Clark [90] and revised by Giovannini et al. [91]. They all reported the existence of three binary compounds, YMg (cP2-CsCl type, T_{max}= 935 °C); YMg_2 (hP12-$MgZn_2$ type, T_{max}= 780 °C); Y_5Mg_{24} (CI58-αMn, T_{max}= 605 °C), formed through a peritectic phase transformation [91] (Table 2-3). The Y_5Mg_{24} and YMg_2 phases were reported to have a range of Mg solubility. The solubility of Mg in the $Y_{5-x}Mg_{24}$ phase and the Y solubility in α-Mg has been determined by Zhao et al. [92]. These results are well consistent with the experimental data of Bermudez et al. [82, 93]. They reported that yttrium concentration changes in the intermetallic phases: 12.0-16.1 at.% and 24-30.1 at.% in $Y_{5-x}Mg_{24}$ and in $Y_{1-x}Mg_2$ respectively. It means that both intermetallic phases in the phase diagram shift to the Mg rich corner and small changes to the lattice parameters of the intermetallic phase may be caused by non-stoichiometric compositions. The maximum solubility of Y in Mg is 4.7 at.% (15.45 wt.%), which is higher than it is presented

in the phase diagram. However, these results are significantly different from thermodynamic modelling results so far and point out the need of a new thermodynamic modelling of the Mg-Y system [92]. The accurate determination of Mg-Y binary phase diagram is a fundamental to the design of novel Mg-Y-based ternary and multicomponent alloys [92]. Although there is confusing data available on the solubility, Mg-Y based alloys are still the most rapidly developing alloy family. The effect of the addition of other RE elements on the phase evolution in Mg-Y-RE systems have been investigated with thermodynamic modelling methods 97], based on the available experimental results from the literature. The Mg-Y based alloys have high specific strength at ambient and elevated temperatures, excellent creep resistance and good corrosion resistivity, as well as a considerable age hardening response [44, 46, 84] and significantly lower texture [98]. Additionally, yttrium is one of the most cost effective elements among the RE elements and definitely the lightest which makes it so attractive for industrial applications.

Table 2-3. Thermodynamically stable intermetallic phases in the Mg-Y binary system.

Phase (Stable)	**Forming T [°C]**	**Structure**	**Lattice parameter [nm]**
Y_5Mg_{24}	<605	CI58, αMn type	a=1.125
YMg_2	<780	hP12, $MgZn_2$ type	a=0.603, c=0.975
YMg	<935	cP2, CsCl type	a=0.378

2.2.5 Magnesium-Gadolinium-Yttrium

In most cases the addition of two or more RE elements can combine the benefit of the addition of single ones. Therefore the research on multicomponent alloys is in the major focus for industrial applications. However, the combination of RE elements always reduce combined solid solubility of two or more alloying addition compared with their individual solubility range, consequently ductility may significantly restricted but the Mg-Y-Gd ternary system is among the most promising because:

- both Gd and Y have a high solubility in magnesium,
- the maximum total solid solubility to remain relatively high despite the multicomponent nature of the ternary alloys.

There is only very limited amount of studies on Mg-Y-Gd system without other elemental addition such as Zn [99, 100]. However, investigation on the ternary system is prerequisite for further focused development of more complex multicomponent alloys based on this system. The investigations on the ternary alloys are generally focused on the possible mechanical or corrosion properties and not many investigations were conducted on the solidification behaviour and microstructure evolution control of which is the key to understanding further alloys development in the system. This is made difficult by recent work on Mg-Y system where the accuracy of the binary phase diagram is questioned [92]. All literature on thermodynamic description of the Mg-Y-Gd system considers only the equilibrium states and provide necessary information for thermodynamic assessments. The isothermal section of ternary Mg-Y-Gd system at 500°C was investigated by Giovannini et al. [101]. Their study reports that Y and Gd show mutual solubility in the binary intermetallic particles, and no new ternary phases form. The magnesium rich corner of the phase diagram was studied with alloys of 85 at. % Mg and 15 at. % RE. The study clarified three-phase region on the specimens after 168 hours of heat treatment at 500°C. Yongchun et al. also reported a study with 2 K/min cooling rates with alloys in the Mg rich corner of the Mg-Y-Gd system [102]. The alloys contained a combination of Y_5Mg_{24} and $GdMg_5$ phases. Based on the available experimental results, the thermodynamic description of the Mg-Y-Gd system was further investigated by Guo et al. [103] using the CALPHAD technique. It was also reported by

Giovaninni *et al*. [101] that after the rapid cooling of the specimens only R_5Mg_{24} (cI58-αMn) type intermetallic phase was possible to be detected with X-ray diffraction (XRD). This finding was reinforced by the investigations with a lower RE concentration alloys by Pang et al. [104]. In their study they investigated the effect of the cooling rate on the microstructure and mechanical properties of GW103K (10 wt% Gd, 3 wt% Y and 0.5 wt% Zr). This system is not clear ternary system but the presence of Zr does not affect the solidification and microstructure evolution as Zr refine the α-Mg grain size prior to the solidification of intermetallic phases through provision of heterogeneous sites for nucleation and refining the grain size of Mg. The cooling rates were determined between 0.7 to 3.6 °C/s (42-198 K/min). They could detect only the R_5Mg_{24} intermetallic with the use of XRD. Although the ternary system shows the same precipitate sequence as the Mg-Gd system during isothermal ageing, the age hardening response differ from the binary system [105, 106]. GW73K alloy showed significantly improved mechanical and corrosion property profile after aging temperatures of 200, 225 and 250 °C [105].

It should be noted that the diffusion coefficients of Gd and Y in Mg are similar to each other (~ 10^{-15} m^2/s at 440°C) and is about one order of magnitude lower than Al, Zn or the self-diffusion of Mg (~ 10^{-14} m^2/s at 440°C) [82]. The atomic radiuses of Gd and Y are similar to each other too: ~190 pm= $1.96 \cdot 10^{-12}$ m [107], while the Al (~121 pm), Zn (~122 pm) or the Mg (~141 pm) are significantly smaller. Thus diffusion driven changes shall take longer time in RE alloys than in AZ alloys, but interchange between the Y and Gd elements are expected during the formation of intermetallic phases.

This study focuses on the solidification behaviour and phase formation sequences in magnesium alloys with a total of 15 wt% RE addition, in which RE is the mixture of Gd and Y where xGd + (15-x)Y is 15wt% and x varies between 0-15.

2.3 X-ray Diffraction

X-ray diffraction (XRD) is a non-destructive method, which relies on the dual wave/particle nature of X-rays to obtain information about the structure of materials [108]. XRD is commonly used for X-ray crystallography which identifies and characterizes compounds based on their diffraction patterns [109]. Besides the basic background of the method the interaction of the X-ray with matter and its sources will be described briefly.

2.3.1 Interaction of X-rays with matter

Compared with visible light photons (λ~430-640 nm), X-rays have at least three orders of magnitude smaller wave lengths (λ~10-0.001 nm) which corresponds to an energy range of 5-5000 keV [110]. Photons are elementary particles (quanta of electromagnetic waves), exhibiting properties of both waves and particles. This dual feature (alongside with neutron and electron beams) makes it possible to use them for a wide range of different type of measurement methods [110]. The correlation between wavelength and energy of photos is given by the Planck equation: $\boldsymbol{E=hc/\lambda}$. Where $\boldsymbol{h}$ is the Planck constant ($6.626 \cdot 10^{-34}$ J·s), $\boldsymbol{c}$ is the speed of the light in vacuum ($2.9979 \cdot 10^{8}$ m/s), $\boldsymbol{\lambda}$ is the wavelength [nm] and the $\boldsymbol{E}$ is the energy of the photon [eV] (1 eV=$1.602 \cdot 10^{-19}$ J). The X-rays interact in four different ways with electrons:

- Photoelectric absorption; X-ray spectroscopy, Auger spectroscopy [111],
- Compton scattering (inelastic or incoherent scattering),
- Rayleigh scattering (elastic or coherent scattering); XRD,
- Pair production.

2.3.2 X-ray sources

X-ray tubes

X- ray tubes have been developed through the last century from the first ever used, but the basic principle remains the same. In a vacuum tube, high voltage is used to accelerate electrons released

by a hot cathode. The high velocity electrons hit the metal anode and create the X-rays. This radiation is generated by the bremsstrahlung (breaking radiation) effect. The maximum energy depends on the applied voltage, while the intensity is determined by the current flow. Beside the continuous photon spectrum from the bremsstrahlung effect, characteristic photo-radiations, is also generated. These characteristic peaks depend on the ***voltage*** and the ***material*** of the anode [110]. Generally, these characteristic and monochromatic K_α radiations are used for further investigations such as XRD or laboratory CTs.

Synchrotron Radiation

The basic principle behind the generation of synchrotron radiation is that charged particles emit electromagnetic radiation when accelerated. It was discovered by Heinrich Hertz already in the 19^{th} century. If charged particles moving at relativistic speeds are forced by a magnetic field to follow curved trajectories they emit electromagnetic radiation in the direction of the motion, known as synchrotron radiation [112].The main properties (advantages) of the synchrotron radiation are the following:

- high intensity or high flux (allows rapid experiments),
- tuneable energy due to the broad and continuous spectrum (from μ-waves to hard X-rays),
- natural narrow angular collimation,
- high degree of polarization (both linear and circular),
- pulsed time structure (allows the resolution of process ~10 ps),
- high brilliance: highly collimated photon beam (spatial coherence),
- ultra-high vacuum environment results high stability (submicron source stability),
- all properties are quantitatively evaluable.

The core of the radiation is the storage ring where the charged particles (generally electrons or positrons) are running around, but the number of applied High Magnetic Field Devices (HMFD) (wigglers, undulators, bending magnets) determine the possible number of generated radiations. These radiations can be used for several purposes simultaneously, however the beamlines attached

to the HMFD must take care of additional X-ray optics and if required the monochromator to adjust and optimise the beam for the specific application. In case of X-ray diffraction, a monochromatic beam is essential. The high brilliance of synchrotron radiation is the greatest benefit in this study. The brilliance (***Br***) of an X-ray source is defined as: $Br = F/(A \cdot \Omega \cdot \Delta E/E)$, where ***F*** is the flux of the photon from the source, ***A*** is the beam size, ***Ω*** is the solid angle, into which the radiation is emitted, and ***ΔE/E*** is the relative energy-bandwidth of the beam. The brilliance of different X-ray sources is presented in Figure 9. It shows that laboratory X-ray sources have at best a brilliance that is eight orders of magnitude lower than that of a modern synchrotron radiation source [20]. This essential difference makes it possible to perform far faster experiments with better statistics compare to that with laboratory (*ex-situ*) equipment. Moreover, it provides the unique opportunity to design experiments during continuous processing (*in-situ*) [110,113].

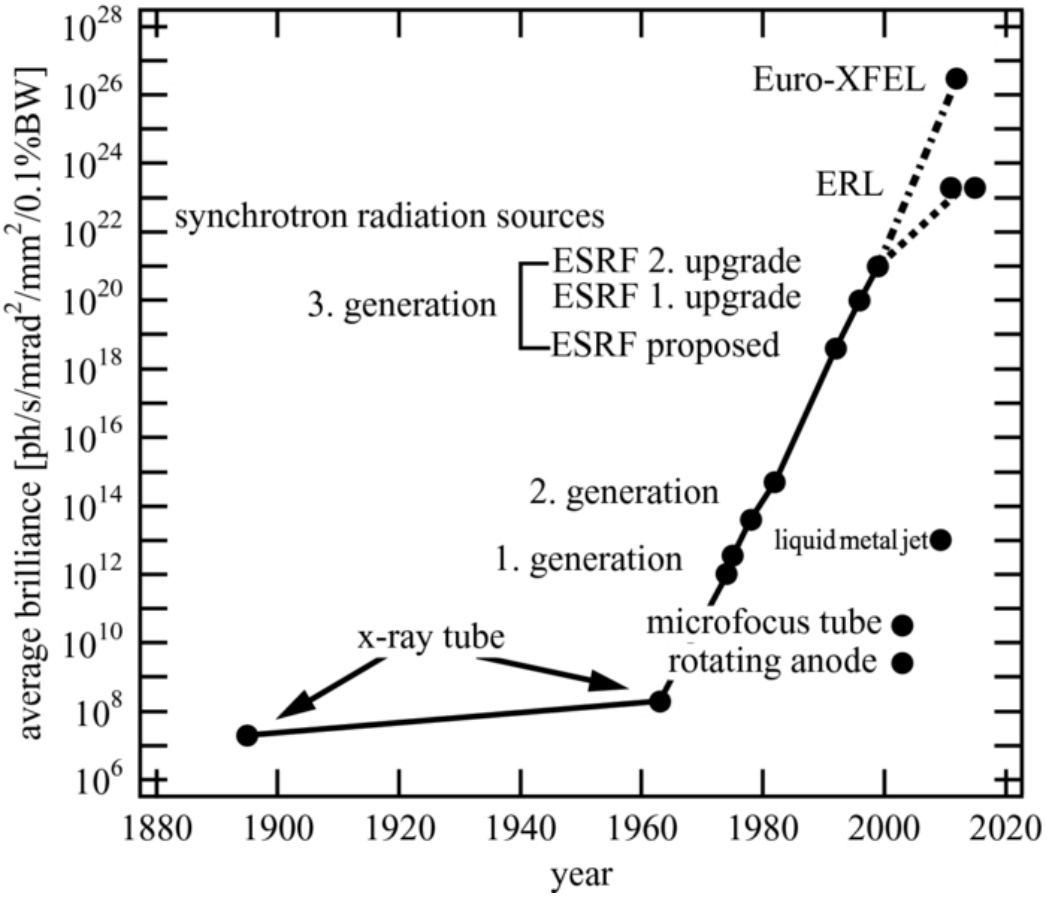

Figure 9. Brilliance of different X-ray sources [20].

2.3.3 Theoretical background of X-ray diffraction

X-ray diffraction is based on constructive interference of the elastic scattered X-rays on a crystalline sample (Figure 10). The interaction of the incident rays with the sample produces constructive interference when conditions satisfy the Bragg´s law [114]: $n\lambda=2d\cdot\sin\Theta$, where n is an integer, λ is the wavelength of the incident X-rays, d is the distance between the oriented atomic layers in the crystal and Θ is the angle of incidence. The directions of possible diffractions depend on the size and shape of the unit cell of the material.

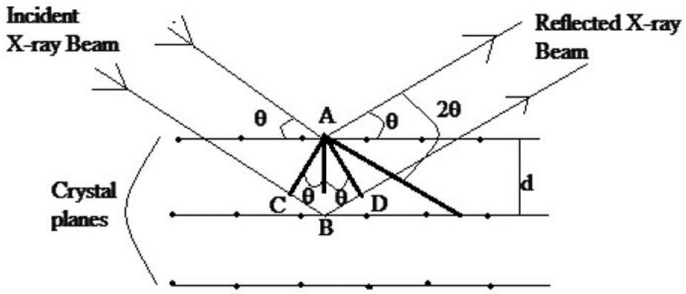

Figure 10. Schematic of the diffraction of monochromatic X-ray beams on a crystalline structure [115].

By scanning the targeted sample through a range of 2Θ angels, the possible diffraction directions (each corresponding to a certain d) of the lattice can be detected. The measured intensity data is generally presented in the function of 2Θ (*Intensity-2Θ*), however exchanging the 2Θ to reciprocal lattice parameter ($q=2\pi/d$ [nm^{-1}]) is beneficial if data sets measured with different wavelengths of X-rays are correlated [116, 117]. The interplanar distance (d) can be calculated from the parameters of the unit cells and Miller indices. The formulas for cubic (d_c) and for hexagonal (d_h) structures are the following:

$$d_c = \frac{a}{\sqrt{h^2 + k^2 + l^2}}$$

$$d_h = \frac{a}{\sqrt{\frac{4}{3}(h^2 + k^2 + h \cdot k) + \frac{l^2}{(\frac{c}{a})^2}}}$$

These equations explain the reason for using monochromatic X-rays for diffraction. In order to experience any constructive interference of the reflected electromagnetic waves, the wavelength (λ) has to be typically in the same order of magnitude (0.1-100 Å= 10^{-2}-10 nm) as the spacing (***d***) between planes.

2.3.4 Application of X-ray diffraction

There is a wide-ranging field of applications for X-ray diffraction. The resulted diffraction peaks of the patterns have to be analysed accordingly. The three major data points used in the analysis of the peaks are: position, width and intensity. The position of the peak gives the major structural information through the deep spacing (***d***). Any structural change or change in lattice parameter is directly correlated with the peak position. X-ray diffraction peaks broaden when the crystal lattice becomes imperfect. According to the theory of kinematical scattering, X-ray diffraction peaks broaden either when crystallites become smaller than about a micrometre or if lattice defects are present in large enough abundance [118]. These defects can be dislocations, twins, grain boundaries, chemical heterogeneities, precipitates or just residual mechanical stresses. These possibilities extend the range of XRD application to even in the field of structural material science. Without taking account all the possibilities, some example are given in the following list [110, 111]: characterization of crystalline structures, grainsize measurements, determination of unit cell dimensions, measurement of sample purity, determination of crystal structures using Rietveld refinement, determination of modal amounts of mixed phases (quantitative analysis), characterization of thin films (dislocation density, lattice mismatch, thickness/roughness), texture measurements.

2.3.5 *In situ* experiments with synchrotron radiation X-ray diffraction (SRXRD)

The microstructural evolution occurs during thermomechanical process steps. In complex process routes and examined materials the outcome cannot be explained only from information from pre- and post-process stages. Therefore, obtaining information during dynamic studies would often be more appropriate. The continuous development of the X-ray acquisition systems at synchrotron sources provides a unique tool to characterize the phase formation and evolution during the thermomechanical processing steps (welding, casting, rolling etc.) *in situ*.

In situ experiments have been conducted with synchrotron radiation both with CT [119, 120] and X-ray diffraction (SRXRD) methods. The following investigations have been already published:

- solid state transformations [113],
- mechanical tests [110, 113, 121, 122],
- welding [110, 113, 123, 124],
- solidification [125, 126, 127 128, 129, 130].

The use of the *in situ* solidification using SRXRD is the recording of diffraction patterns while the examined alloy is cooling in a controlled way. These results can supply experimental validation and/or clarification to existing thermodynamic databases. In complex, multicomponent alloy systems it can be used as a unique tool to reveal the phase evolutions in systems that has not been considered and developing the phase diagrams for such systems. It also allows for the possibility of studying non-equilibrium conditions and understanding the phase evaluation during industrial process conditions. Solidification of Mg-RE alloys have been already investigated using SRXRD [128, 129,], even alloys from the ternary Mg-Y-Gd system [132]. Szakacs et al. reports results from Mg4YxGd alloys (x= 0, 1, 4). The article indicates that higher RE concentration is required for any reasonable conclusions. Therefore this study is using 15 wt% RE additions to the investigated alloys.

3 Aims and methods

3.1 Aims

The sequence, extent, and nature of the different transformations during solidification have a significant bearing on the final microstructures of the as-cast metals. The solidification process and the phase evolution can be modelled based on the thermodynamic databases [131]. Although such databases provide information on the expected solidification path, the commercial castings normally deviate from the equilibrium descriptions. Therefore, an understanding of the sequence of the intermetallic phase evolution during solidification with different cooling rates (CR) is necessary.

Mg-Gd-Y alloys are of interest in a wide range of applications ranging from structural automotive components to degradable biomaterials. However, the microstructural evolution of this system has not been investigated to understand the types of intermetallic phases observed during solidification. Szakacs et al reported that in dilute ternary alloys $Mg_{24}(Y,Gd)_5$ phase was prevalent [132]. However, due to the low concentration of Y and Gd it was difficult to follow the microstructural evolution during solidification nor was it possible to conclusively show the formation of various intermetallic phases. Thus higher concentrated alloys are needed to understand the phase evolution during solidification, in order to evaluate the effect of Gd content in Mg-(15-x)Y-xGd (where x is between 0 and 15) alloys were investigated. The general aims of the work are:

1. Role of Gd on the intermetallic phase formation in Mg-Y-Gd alloys in the as-cast system,
2. Determine the role of cooling rate on the solidification behaviour of Mg-(15-x)YxGd alloys.

3.2 Key methods

An understanding the fundamental principles which dictate material properties and the optimization of casting/solidification is critical in research and industrial application. In these fields not only static but also dynamic information are of interest. However, the general method is to collect properties and microstructural information from cast or quenched stages of observed phase transformations. In complex alloys the outcome cannot be explained only from these stages. Therefore, obtaining information during dynamic studies would often be more appropriate. The continuous development of the X-ray acquisition systems at synchrotron sources provides a unique tool to characterize the phase formation and evolution during solidification *in situ*. The following methods are used to determine the aim of the study:

1. Phase evolution during solidification: using synchrotron radiation X-ray diffraction to determine the type forming phases and their formation temperatures. The transformation temperatures observed are compared with those measured with conventional thermal analysis.
2. Correlate the experimental findings on phase evolution and the transformation temperatures with those observed from the ternary Mg-Gd-Y phase diagrams using Scheil model for solidification.

4 Experimental Procedures

4.1 Alloy composition and preparation

This study investigates the ternary Mg-Gd-Y system with five nominal composition of: Mg15Y, Mg10Y5Gd, Mg7.5Y7.5Gd, Mg5Y10Gd and Mg15Gd. The alloys were cast at the Magnesium Innovation Centre (MagIC) in Helmholtz - Zentrum Geesthacht using permanent mould gravity casting (PMGC) or permanent mould indirect chill casting (PMDCC) [133]. The alloys were cast from pure metals magnesium (99.99%) yttrium (99.95%) gadolinium (99.95%) and Mg15Gd (14.8 wt. %) master alloy. Table 4-1 shows the investigated alloys' casting method and designations. The ASTM designation of magnesium alloys are W and V for the yttrium and for the gadolinium respectively. However, G has been used for gadolinium in several publications. This current work will use G to avoid any confusion.

Table 4-1. The investigated alloys.

Alloy nominal comp.	Casting method	Designation
Mg15Y	PMGC	W15
Mg10Y5Gd	PMGC	WG105
Mg7.5Y7.5Gd	PMGC	WG77
Mg5Y10Gd	PMGC	WG510
Mg15Gd	PMDCC	G15

4.1.1 Gravity casting

All alloys except G15 were produced by permanent mould gravity casting. Pure Mg and Mg15Gd master alloy pieces were melted in an electric furnace under protective atmosphere (2 wt.% SF_6 and 98% Ar). The melt was heated up to 710-720 °C and kept at the temperature 15 minutes following the addition of preheated yttrium pieces. Prior to pouring, the melt was stirred several times to ensure the uniform distribution of alloying elements. The melt was poured into a cylindrical steel mould coated with hexagonal boron nitride (BN) and preheated to 400°C. The as

cast ingots were approximately 100 g in weight and were 110-130 mm in length with a diameter of 13 mm (Figure 11).

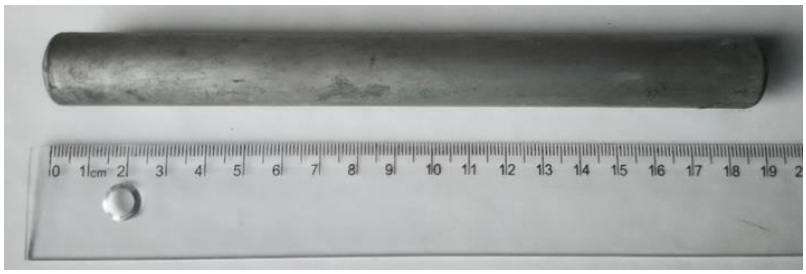

Figure 11. The permanent mould gravity casting (PMGC) ingots.

4.1.2 Permanent mold indirect chill casting

This material was used two ways during the study: as G15 alloy, since the composition meets the desired composition (~15 wt.% Gd binary alloy) and used as a master alloy to produce the ternary alloys. The permanent mould direct chill casting [133] was the most suitable from the available methods to produce larger amounts with low deviation in the concentration of the entire ingot. To produce the alloy pure Mg (99.95 %) and Gd (99.95 %) were used. After melting the pure Mg the preheated Gd pieces were added at 720 °C and the melt was kept at that temperature for 15 minutes with continuous stirring (200 rpm). The melt was then poured into a preheated (400 °C) steel mould. The mould was coated with hexagonal BN. The mould with the melt was placed into a holding tubular furnace at 680 °C for 15 minutes. After the holding time the mould was lowered at a speed of 2 mm/s into flowing water to solidify the ingot. During the process the same protective atmosphere: 2 wt% SF_6 in Ar was used. During the holding, light reaction products will float while heavy ones settle. This results in a higher cleanliness of melt.

4.1.3 Chemical analysis of the alloys

The chemical composition of the alloys were determined by a spark emission spectrometer (Spectrolab M, Spektro, Germany) and by an X-ray fluorescence spectrometer (Bruker AXS S4 Explorer, Bruker AXS GmbH, Germany).

4.2 Quenching experiment on G15 alloy

In order to follow high temperature phase transformations of intermetallic phases, a small specimen of G15 alloy was quenched from a temperature near the eutectic transformation temperature of the alloy. For this experiment the chamber of a Bähr 805 dilatometer (Figure 18) was used as a furnace, which uses an induction coil for melting. Small specimens were placed in medium pressure steel crucibles (ME-29990). A type S thermocouple was welded on the side of crucible to control the temperature. The crucible was placed in the middle of the induction coil which heated up the sample to 750 °C. Held for 5 minutes and cooled to the eutectic temperature at a rate of 100 K/min. From 2°C above the eutectic temperature the sample was quenched by rapidly flowing N_2 and switching off the heating system.

4.3 Sample preparation for microstructure analysis

Samples from as cast (laboratory cast alloys) and as-solidified (from the *in situ* solidification experiments at the synchrotron beam line) state were embedded in a multicomponent plastic resin (Demotec 30) with a mixture of methyl methacrylate powder and liquid volume ratio of 1:1. The embedded samples were ground with SiC-grinding papers with a granularity of 200, 500, 800, 1200 and 2500 by a Struers polishing machine. Automatic grinding was performed on 6 samples at once using 10 N of force per sample and a speed of 100 rpm and 80 rpm on the table and the sample holder respectively. Each grinding step was carried out for 1-3 minutes under running water. After the grinding process the samples were washed and dried. The samples were polished manually with an OP-Chem polishing cloth in combination with water free colloidal silica solution (OP-S) and 1 μm diamond paste. The polishing step took 1 to 3 hours dependent on the specimen. After finishing the polishing, samples were washed with ethanol and dried. As a final step, the samples were cleaned with ethanol on a clean OP-Chem cloth to remove any residual colloidal silica solution.

Optical microscopy (OM) analysis was carried out using a Leica DMI500 M microscope.

Scanning Electron Microscopy (SEM) was performed on the as-cast and as-solidified samples with a VEGA3 Tescan SEM operating at 15 kV in back-scattered electron (BSE) imaging mode at working distance of 15 mm. The volume fraction of the intermetallic particles was determined of the averages of 3 images using the software ImageJ [134].

The Tescan SEM is attached with an EDAX energy dispersive X-ray spectrometer (EDXS). The EDXS point analysis was performed on different parts of the microstructures. The EDX spectra were recorded for 30 s. Software Iridium Ultra was used to record and analyse the EDX spectra and both the atomic and weight concentrations of elements of interest in the samples were indicated.

Thin foils for transmission electron microscopy (TEM) were prepared from the as cast condition ingots. The slices of alloys with a thickness of 0.5 mm were cut with a slow speed saw with the speed of 2000 rpm with continuous running water for cooling. Discs with a diameter of 3 mm were punched from these slices. These discs were ground to approximately 0.15 mm. The final step of the foil preparation was done by electrolytic polishing in automatic double jet device TENUPOL 5. The polishing was performed at 50 V, with a current of 0.08-0.1 A, in 1.5 vol. % $HClO_4$ mixed in ethanol at -45°C. After thinning, foils were washed in high purity ethanol, soaked in ethanol for a minimum of 2 minutes and dried in air for 2 minutes.

The specimen from the quenched G15 sample was prepared from a region containing intermetallic particles, using focused ion beam (FIB) milling with a FEI Helios NanoLab 600 DualBeam FIB/SEM. The electron beam voltage was 10 kV and the current 0.54 mA. The ion beam was operating at 30 kV and the current was set between 0.3 and 0.5 nA during the milling process. The specimen surface was protected with a 500 nm Pt layer (Figure 12, left) prior to FIB processing with Ga^+ ions to protect the specimen from damage. The prepared specimen was mounted on Cu grids for TEM investigations (Figure 12, right) and then it was further milled as a cleaning process with the ion beam operated at 5 kV with 70 pA.

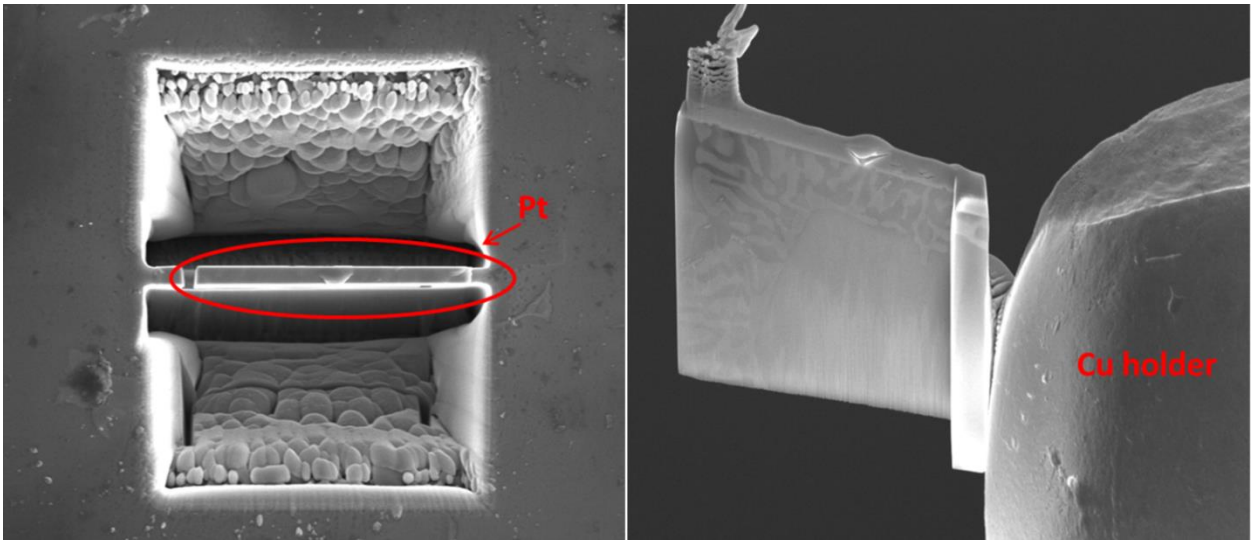

Figure 12. Steps of sample preparation by FIB are shown. Left side shows how the interested area was protected with Pt layer and cut out from the bulk material, and the right side shows the already cut and welded sample on the Cu sample holder.

Transmission electron microscopy (TEM) was performed on a FEI CM200 TEM equipped with an EDAX energy dispersive X ray (EDX) spectrometer operating at 200 kV. The investigations were made in bright field-imaging mode (BF) with two beam electron contrast condition in appropriate cases, while micro-beam electron diffraction (MBED) patterns were recorded with a nominal beam diameter of 30 nm, a camera length of 700 mm and a nominal condenser aperture diameter of 30 μm, from primary intermetallic phases.

The qualitative energy dispersive X-ray spectrometry (EDXS) was performed on the FEI CM200 TEM equipped with an Oxford X-Max Inca X stream windowless EDXS detector using a focused electron beam, a condenser aperture with a nominal diameter of 200 μm, and an average detector time of 30 s. The spectra were analysed using of Oxford Inca software using standard analysis assuming thin film conditions.

4.4 Thermal analysis

The samples were cut from the as cast materials weighed and then placed in medium pressure steel crucibles (ME-29990) then closed under an Ar atmospherein a glove box to ensure no contaminations with oxygen to prevent any elevated temperature oxidation of the molten Mg. The transformation temperatures during solidification were determined with Differential Scanning Calorimeter (DSC) using a Mettler Toledo [135]. The experiments were performed at 5 and 20 K/min heating and cooling rates under an Ar atmosphere.

4.5 Solidification studies with synchrotron radiation diffraction

Small samples were machined from the as-cast material in order to fit in the graphite crucibles designed for the synchrotron diffraction experiments (diameter = 4 mm, height = 5 mm) to study the solidification.

The measurements were carried out at the Petra III P07 High Energy Materials Science (HEMS) Beamline of Helmholtz-Zentrum Geesthacht (HZG) at the Deutsches Elektronen-Synchrotron (DESY). The measurements were performed in the chamber of a Bähr 805 dilatometer in Ar flow (Figure 14). The dilatometer has been modified for *in situ* synchrotron measurements. There are two windows on the sides covered by Kapton foil (Figure 14 left) , which is transparent for the X-ray beam, and the induction coil is opened in the middle so the beam passes through only the sample and the crucible (Figure 14, right) [128]. The time-temperature program used during experiments is shown in Figure 13.

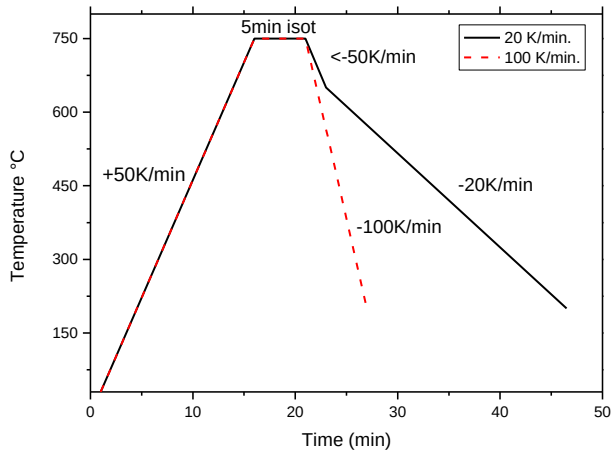

Figure 13. The time-temperature programs of the experiments.

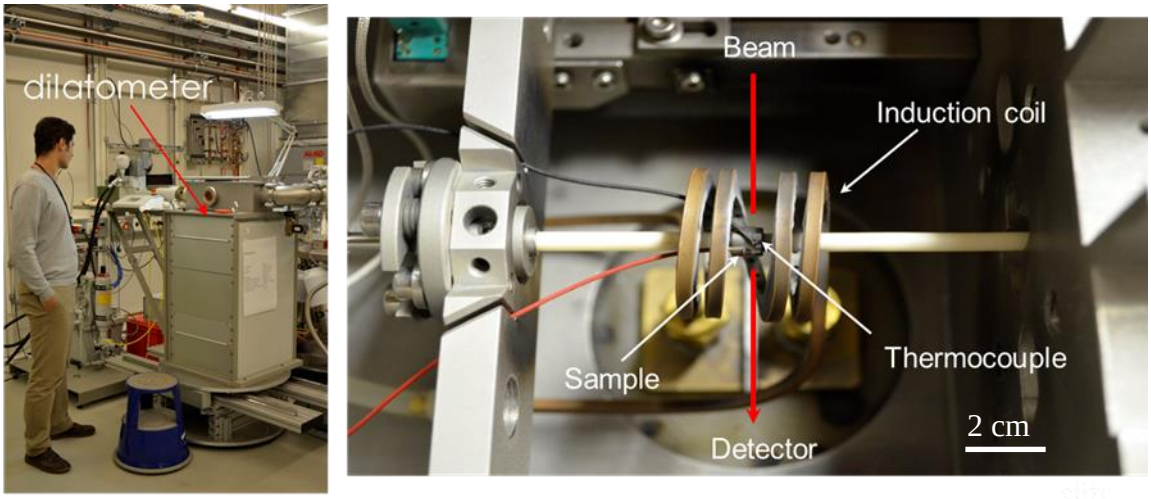

Figure 14. Experimental set up of the *in situ* solidification experiment. On the left is the dilatometer inside the experimental hutch, and right shows the chamber of the Bähr805A/D dilatometer, modified for in situ synchrotron measurements. The windows on the sides are covered with Kapton foil and the coil opened for the beam to pass only through the sample [128].

During the experiments the samples were contained in graphite crucibles closed with steel caps. These caps isolate the molten metal from the surrounding atmosphere and make it possible to weld type S thermocouples to control the measurement. The samples were heated up to 750 °C held for 5 min, to ensure melt homogeneity and then cooled to 200 °C with a controlled cooling rate of 20 or 100 K/min. The *in situ* diffraction experiments were conducted in transmission geometry using a beam with a cross section of 1×1 mm^2. At the main beamline the beam was set to the photon

energy of 100 keV, corresponding to a wavelength of $\lambda = 0.0124$ nm. During the experiments the 2D diffraction patterns (Figure 15) were recorded with an acquisition time of 3 s (in the case of 20 K/min CR) and 0.1 s (100 K/min) by a Perkin Elmer XRD 1621 Flat Panel detector [136] with a pixel size of $(200\ \mu m)^2$. Using the selected acquisition times, 1 K temperature-resolution is possible in both cases. With the 3 s acquisition time the detector was used in slow mode and in this case, it is automatically synchronised with the dilatometer. The dilatometer data sets are recorded at the same time as the 2D patterns are recorded by the detector because both are synchronized with the X-ray slit. When the slit is open, both sets of data are recorded. In fast mode, which is required with 0.1s acquisition time, the slit is open. The actual recorded temperature of the 2D patterns can be checked through the time of the recordings manually. The sample to detector distances was determined using a LaB_6 standard powder sample as a reference.

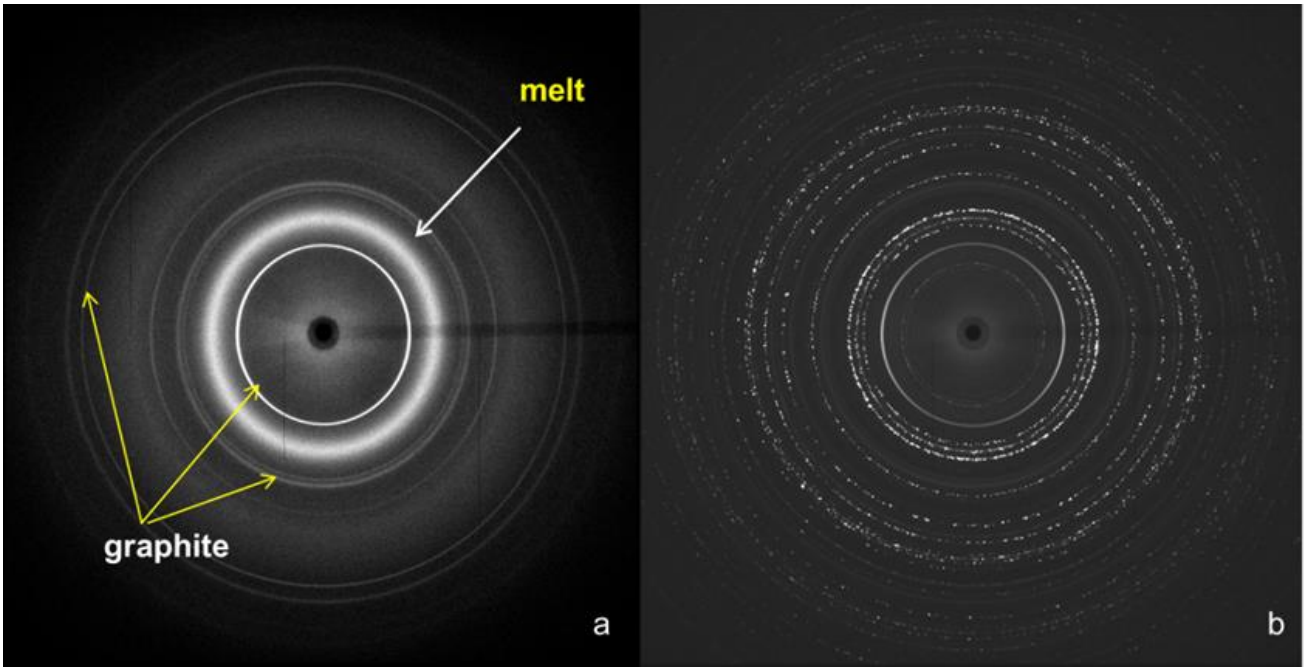

Figure 15. 2D diffraction patterns, taken during the solidification experiment of G15, are shown. When the sample is molten and only the rings of the crucible and the molten background is visible (a) and when the sample is fully solidified (b).

4.6 Data analysis and calculation

The 2048 × 2048 pixel diffraction patterns were integrated to azimuthal line profiles by using the fit2d software [137]. The information on the intermetallic phases were obtained from the Pearson's Crystal Structure Database [138], the d-spacing and 2θ angles for the phases were calculated using CaRIne Crystallography 3.1™ software. To make the results from the different beamlines directly comparable, using different wavelengths, several measurements of reciprocal lattice parameters (q) were determined and used for presenting the results plotted in software Origin. The experimentally recorded temperatures for various phases were compared with the solidification simulations performed with Pandat™ with PanMagnesium 2017 thermodynamic software [10].

5 Results

5.1 Chemical analysis of the as-cast ingots

The as-cast ingots were chemically analysed with X-ray fluorescence and spark emission spectrometry. The X-ray fluorescence gives more reliable results for gadolinium, while the spark emission spectrometry is more accurate for Y. Both the bottom and top parts of the ingots were analysed (Table 5-1) and the average results are presented in the Table 5-2. The Fe, Cu and Ni concentrations were also determined and in each sample the concentrations of Fe, Cu and Ni are < 0.016 wt.%, < 0.025 wt.% and < 0.01 wt.% respectively.

Table 5-1. Chemical compositions from the top and button section of the ingots of the investigated alloys.

Alloy		**Y [wt. %]**	**Gd [wt.%]**	**Mg [wt.%]**
W15	Top	*14.9*	-	*Bal.*
	Bottom	*13.3*	-	*Bal.*
WG105	Top	*10.5*	*5.5*	*Bal.*
	Bottom	*10.2*	*5.4*	*Bal.*
WG77	Top	*7.2*	*7.1*	*Bal.*
	Bottom	*6.7*	*7.3*	*Bal.*
WG510	Top	*5.8*	*10.7*	*Bal.*
	Bottom	*5.7*	*11.0*	*Bal.*
G15	Top	-	*15.1*	*Bal.*
	Bottom	-	*14.5*	*Bal.*

The cast materials have some contamination of Cu, Ni and Fe elements however, all these elements are below the 250 ppm range and comparable concentration in each alloy investigated. This level of contamination should not have any effect on the solidification behaviour or at least the effect

should be similar. The current work is not focused on corrosion properties; thus the level of contamination is acceptable and not considered any further for the solidification studies.

Table 5-2. The average chemical compositions of the as cast ingots.

Alloy	**Y [wt.%]**	**Gd [wt. %]**	**Mg [wt.%]**
W15	*14.1±0.5*	-	*Bal.*
WG105	*10.3±0.2*	*5.4±0.05*	*Bal.*
WG77	*6.9±0.2*	*7.2±0.1*	*Bal.*
WG510	*5.7±0.1*	*10.8±0.3*	*Bal.*
G15	-	*14.8±0.3*	*Bal.*

5.2 As-cast microstructure of the binary alloys

The microstructure characterization of the as-cast alloys was performed using SEM and OM. For all investigations the middle part of the ingots was used. The as-cast microstructures are shown in Figure 16 (a-d). On the left side are the optical micrographs and on the right side are the SEM-BSE micrographs. The characteristic feature in the two alloys structure is the existence of intermetallic phase(s) regions in the alloys containing yttrium (W15) or gadolinium (G15) visible as bright areas in Figure 16 b and d. The intermetallic phases are rich in either Gd or Y as it has been reported in former studies [81]. They have a typical eutectic structure with regular alternation of α-Mg and secondary phase. Many darker grey areas visible in the SEM-BSE images are secondary phase regions in a certain depth under the specimen surface. But one cannot exclude that the concentration of solutes is higher in the matrix near to the eutectics which may likely account for this feature in the BSE micrographs. Beside the eutectic structure, a smaller distribution of bright spots were also observed (pointed by the arrows). These particles are rich in Y or Gd (Rare Earth rich particles: RERP), sporadic nests of Gd-containing particles were found. These particles can be rare earth hydrides (RH_2) [69]. The volume fraction of the intermetallic particles in the as cast structure are presented in Table 5-3. The results from the SEM-EDX analysis from the as-cast materials are presented in Table 5-4.

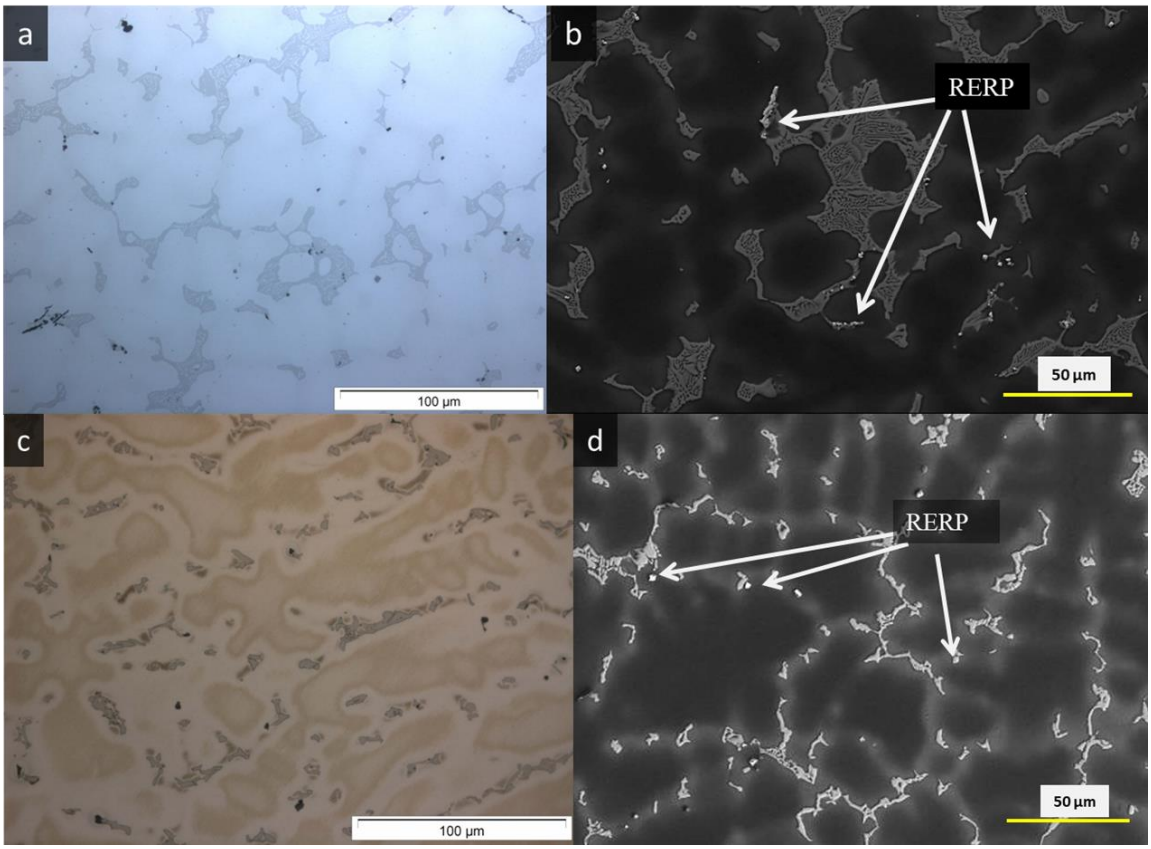

Figure 16 As-cast microstructure of the W15 (a and b) and G15 (c and d) OM (left), SEM-BSE (right). The brighter regions are the eutectic structure and in the border of the eutectic structure rare earth rich particles (RERP) are observed.

Table 5-3. The area fraction of the intermetallic phases in the as-cast structure.

Alloy	**Area fraction of intermetallic phases [%]**
W15	*9.52±0.42*
G15*	*10.31±0.28*

* The cooling rate was higher during the casting of G15 alloy.

Table 5-4. The concentration of the Gd and Y in the alloy determined by SEM-EDX.

Composition	**Concentration (alloy) [wt.%]**		**Concentration (intermetallic) [wt.%]**		**Concentration (matrix) [wt.%]**	
	Y	**Gd**	**Y**	**Gd**	**Y**	**Gd**
W15	*14.2*	-	*28.05*			*8.52*
G15	-	*13.28*	-	*81.4*	-	*11.1*

5.3 The in situ solidification investigations of the binary alloys

The solidification behaviour of the alloys was experimentally determined by DSC and by SRXRD. SRXRD experiments were carried out in Bähr 805 dilatometer meanwhile synchrotron radiation was used to record the 2D diffraction patterns from the phase evaluation during the solidification of the alloys with two different cooling rates (20 and 100 K/min). The as-solidified samples from the synchrotron measurements were further investigated by OM and SEM and are also presented in this chapter.

5.3.1 Results of the in situ SRXRD solidification of the W15 alloy

The azimuthally integrated line profiles of the 2D diffraction patterns acquired during the solidification experiments of W15 alloy are shown in Figure 17. The horizontal axis of the graph is the reciprocal lattice parameter (q [nm^{-1}]) and the vertical axis is the normalised intensity (without unit). In the upper portion of the graph, the molten stage of the two different cooling rates (CRs) measured 720°C is shown. Although the line profiles are normalized, there are differences between them due to the acquisition times. In the case of the CR of 20 K/min the signal-noise ratio is ten times larger than that of CR of 100 K/min. Therefore, the CR of 20 K/min line profiles are smoother. The other difference is caused by the inhomogeneous nature of the specimens. There are small differences between the two specimens in terms of concentration of Y and contamination (due to oxides and fluorides).

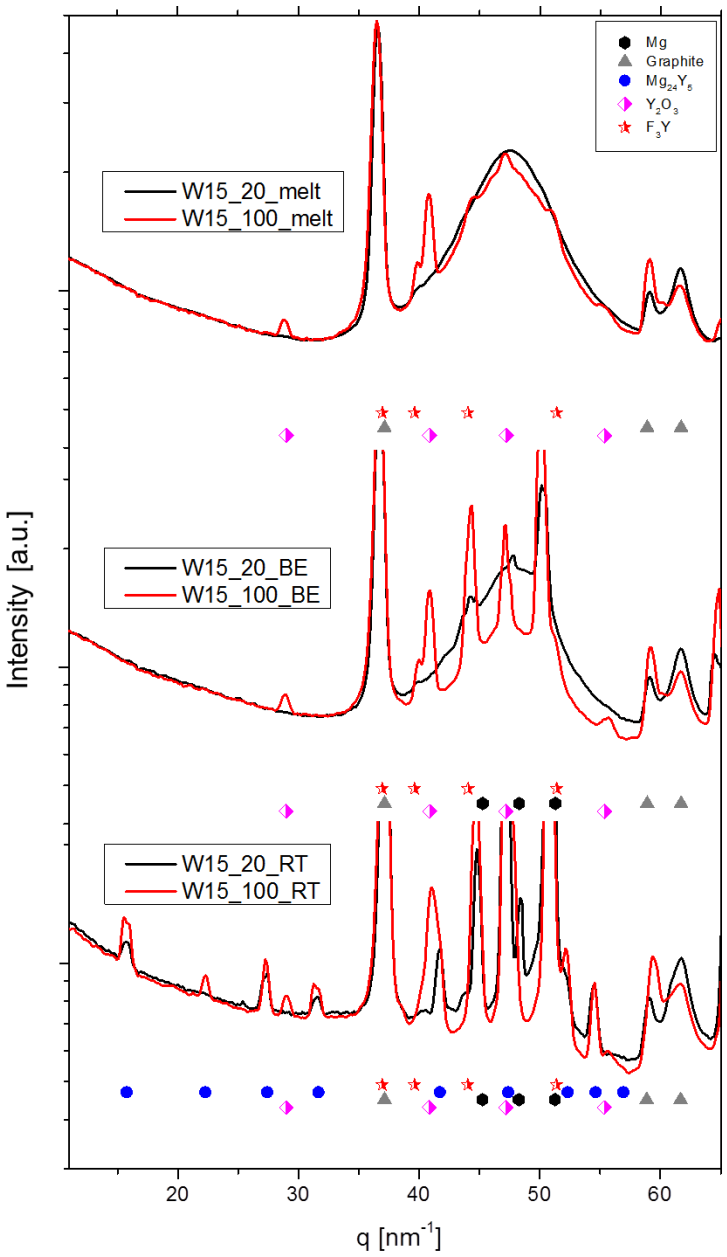

Figure 17. The results of the *in situ* solidification experiments of W15. Red lines correspond to the experiment conducted with 100 K/min CR and the black lines belong to the 20 K/min CR. In top of the figure is the molten state of the two experiments. In the middle part of the figure the partly solidified (liquid and α-Mg) state before the eutectic temperature. And the bottom of the figure represents the fully solidified state. Symbols are used to index the major visible peaks of the observed phases.

When the samples are molten, a diffuse background originating from the melt and diffraction peaks of the graphite crucible can be observed in both experiments. However, the sample used for the CR of 100 K/min experiment exposes stronger additional peaks. These peaks are a continuous part of the background and can be indexed according to the peaks of Y_2O_3 and/or F_3Y phases. These phases are from the residual contamination from the casting. Yttrium is more reactive than Mg, and the formation of oxides or fluorides are expected where oxygen and fluorine (from the cover gas) are present.

During cooling from the melt near the liquidus temperature α-Mg starts to form from the liquid. With the decrease in temperature, the Mg peaks become more pronounced and Mg is the only phase that forms from the melt before the eutectic temperature is reached. After the eutectic temperature is reached, the formation of only one intermetallic phase is observed. At this temperature the system is fully solidified and there is no further phase transformation observed in the alloy (this is illustrated by the curve recorded at room temperature). The phases are indexed with symbols in Figure 17.

Although the changes to the CR did not result in different solidification paths for the alloy, the resultant microstructures are different in terms of the volume fraction of the intermetallic particles. The micrographs are shown in Figure 18 and the volume fractions of the intermetallic particle are presented in Table 5.5.

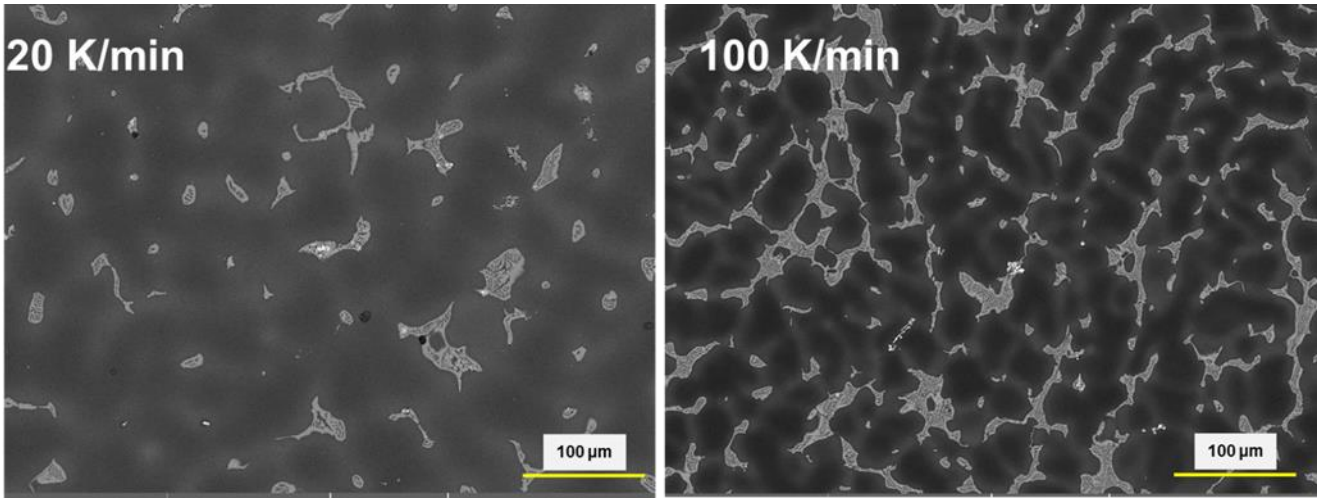

Figure 18. The resulted BSE micrographs of W15 alloy with both CRs. The left shows a CR of 20K/min. while the right with a CR of 100 K/min. The evaluated area fractions of the intermetallic phases are presented in table 5-5. The darker areas (pores) were extracted from the total area.

Table 5-5. The results of the area fractions of the intermetallic phases (IMP) and the area fraction of RERPs in the W15 alloy for the two cooling rates (20 and 100 K/min).

Alloy	Cooling rate	Area fraction of IMP [%]	Area fraction of RERP [%]
W15	**20**	*4.7±0.06*	*0.2±0.01*
	100	*10.8±0.12*	*0.4±0.02*

EDX point analysis was performed on different areas of the as-solidified samples. Only typical information is presented in the following sections. These presence of some of the features in the microstructure were more pronounced in the sample examined with a CR of 100K/min. Therefore, a micrograph and a more detailed analysis is presented from that specimen in Figure 19. The chemical composition of the matrix slightly differs from each other. The analysis targeted three different type of areas in the microstructure: matrix, eutectic structure and rare earth rich particles (RERP). The centre of the X points represent the centre of the applied beam.

EDX analysis at point three was taken from the core of the matrix. Only the matrix chemical composition differs between the two cooling rates. The average concentration of the Y in the matrix is around a 20-25% higher at 20 K/min than at 100 K/min CR {~2.5 at.% (~8.7 wt.%) and

~2 at.% (~7 wt.%)}. In addition to Mg and Y, a small amount of oxygen was detected on the region marked X_3 (~2.1 at.%).

To estimate the composition of the intermetallic phase; the point four was taken from the eutectic structure. This point is reflect the concentration of the IMP together with the secondary α-Mg without any other phases (RERP) in the region. The average Y concentration of the area is ~9 at.% (~27 wt.%), which results an atomic ratio of ~8:1 (Mg:Y). A small amount of oxygen was also detectable on the area (~2 at.%).

For the RERPs, the point one was taken from the corner of a larger eutectic region with an addition of segregated particles (RERPs). This typical feature of the analysed microstructure has a higher Y concentration ~31 at.% (~66 wt.%) and magnesium ~23 at.% (~13 wt.%) with a notable amount of oxygen and fluorine (similar atomic concentrations as magnesium) ~22 and ~18 at.%. Small but distinguishable amount of Si is also present on the EDX spectra (~4 at.%). Point two and five are from a larger area where collection of small RERPs are visible. Alongside this are the EDX results obtained spread between 49 and almost 75 at.% Mg, while the concentration of the Y vary from 27 to 16 at.% (~59-43 wt.%). Beside the presence of the two component of the alloy, there is a recognizable amount of oxygen (~6-20 at.%) and silicon (~2.8-4 at.%) can be detected from this area. The EDX point analyses of the different features are shown in Table 5-6.

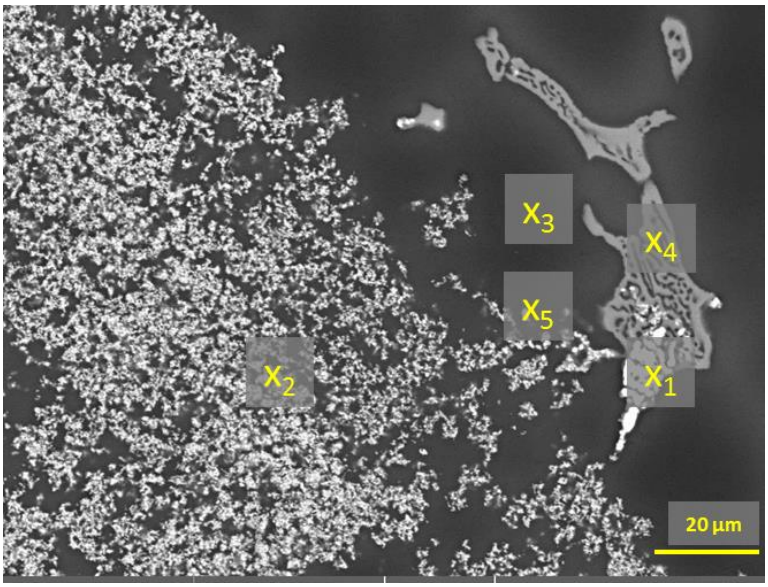

Figure 19. A higher magnification micrograph of the W15 alloy cooled with 100 K/min. The EDX point analyses of the different features are shown in Table 5-6. The middle of the X signs point the centre of the analysing e-beam.

Table 5-6 The EDX point analysis of the typical observed microstructural features in W15 alloy.

	Concentration at. %				
	Mg	**Y**	**O**	**F**	**Si**
X_1	*23.3*	*31.7*	*22.8*	*18.4*	*3.7*
X_2	*74.5*	*16.6*	*6.8*	-	*1.9*
X_3	*95.6*	*2*	*2.1*	-	-
X_4	*87.3*	*9.3*	*2*	-	-
X_5	*49.6*	*27.2*	*19.5*	*0.7*	*2.9*
	Concentration wt. %				
	Mg	**Y**	**O**	**F**	**Si**
X_1	*13.4*	*66.8*	*8.6*	*8.3*	*3.7*
X_2	*52.3*	*42.6*	*3.2*	-	*1.9*
X_3	*91.1*	*7.1*	*1.3*	-	-
X_4	*70.1*	*27.2*	*1.1*	-	-
X_5	*29.8*	*59.8*	*7.7*	*0.3*	*2.9*

For a better overview, the 2D azimuthal integrated SRXRD results during the solidification can be aligned next to each other as a time-2Θ diagram, Figure 20. As the sample is heated up, the peaks/lines originate from the W15 alloy (α-Mg: indexed with light blue colour on the right side, and the intermetallic phase (IM) with purple) disappears. The molten metal appears as bright wider

belt in the range where the three major lines (peaks) of α-Mg exist in the solid phase. The remaining lines mainly belong to the graphite crucible (red) and some Y_2O_3 (yellow). The bottom part of the figure is representing the time-temperature diagram of the experiment and it is attached to the diffraction patterns. The observed formation temperatures are projected with yellow dashed lines to the t-T diagram. The temperature difference between the recorded T_L and T_E during the solidification give the solidification range (ΔT) of the examined alloy. The visible grey level changes after T_E on the graph which indicates that there is no more liquid left and therefore the diffused background reflection is dropped. The intermetallic phase Y_5Mg_{24} has been identified from the diffraction pattern as IM in the time-2θ diagram in Figure 20.

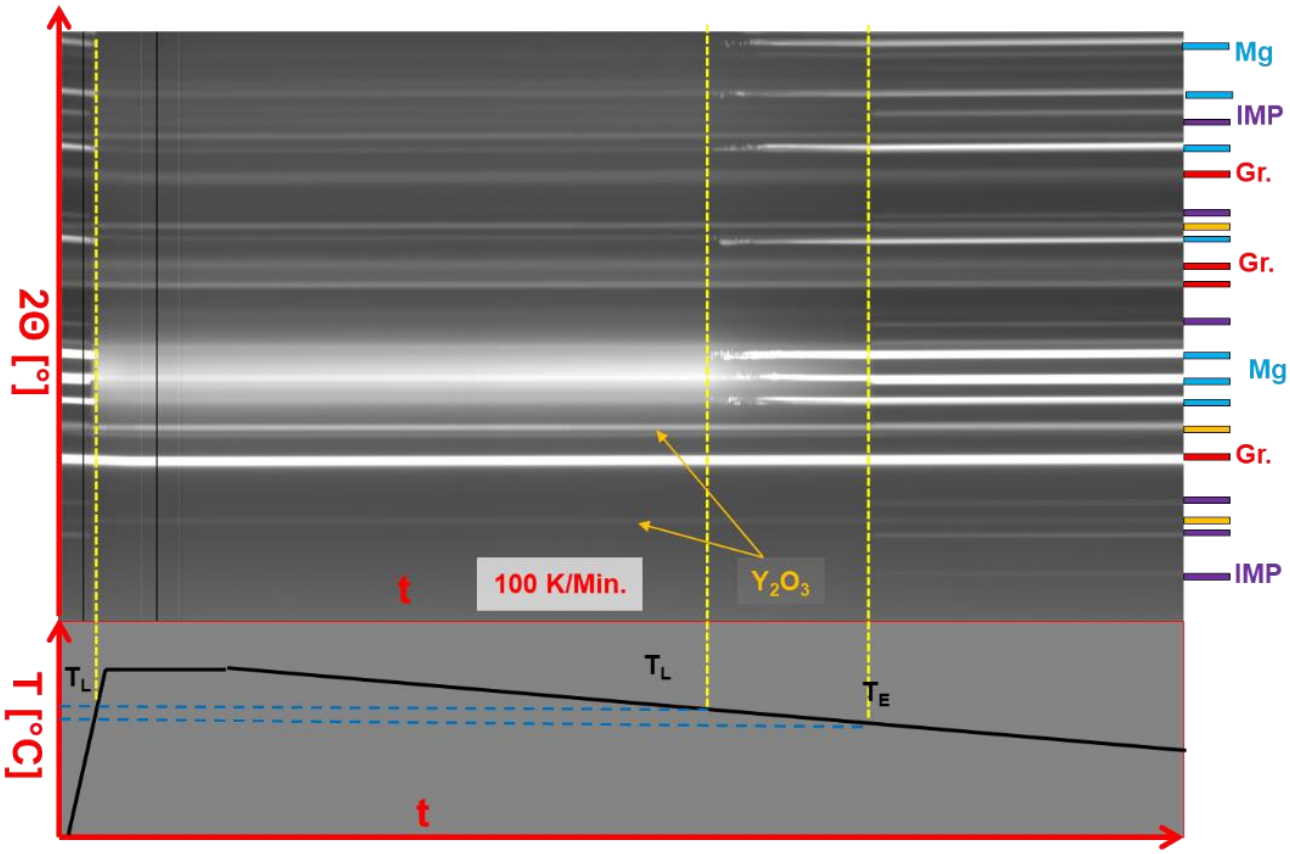

Figure 20. The overview of the SRXRD solidification experiment of the W15 with the cooling rate of 100K/min, and the time-Temperature program of the experiment. During the heat up (left part of the picture) the peaks/lines of the sample (α-Mg: light blue, secondary phase: purple) disappear after overcoming the T_L, and start appearing just after cooling back to T_L (this temperature only α-Mg). In between peaks from the crucible (red: Gr.) and probably Y_2O_3 peaks (yellow arrows) are visible. The peaks of the secondary phase are observed after reaching the T_E and the background radiation also drops at this temperature, indicates that the sample fully solidified.

5.3.2 Results of the *in situ* SRXRD solidification of the G15 alloy

Four different regions were observed during the solidification of the G15 as detected by *in situ* SRXRD. The four specific stages as follows:

1. melt,
2. first solid phase formation (α-Mg); between T_L and T_E,
3. secondary phase formation (γ- Mg_3Gd), liquid phase disappear, solidification ends: T_E,
4. γ transforms to another solid phase (β-Mg_5Gd) already in the solid stage, close to T_E

The 4th stage of the solidification was not possible to be detected with any other method. Any signal from the transformation can overlap with the signals of the eutectic structure formation. Therefore, three different ways are chosen to explain the four sequences of solidification in G15 alloy.

In Figure 21 the azimuthally integrated line profiles of the 2D diffraction patterns acquired during the solidification experiments with a cooling rate of 20 K/min are shown. The horizontal axis of the graph is the measured 2Θ angles in degrees and the vertical axis is the normalised intensity. The changes observed on integrated line profiles are presented together in order to make the changes or peak shifts more pronounced, as it was published in [139]. The CR 20 K/min used as they provide ten times better signal-noise ratio compared with that of line profiles of the CR 100 K/min experiment. On the other hand, the faster CR develops a higher volume fraction of intermetallic phases. Therefore, the 2D diffraction patterns recorded with 100 K/min CR are better to present an overview (time-2Θ diagram) of the full solidification. The major changes in the intermetallic phase formations are more pronounced (Figure 22) and the raw 2D patterns are used to compare the different stages during last of the solidification phase transformations (Figure 24).

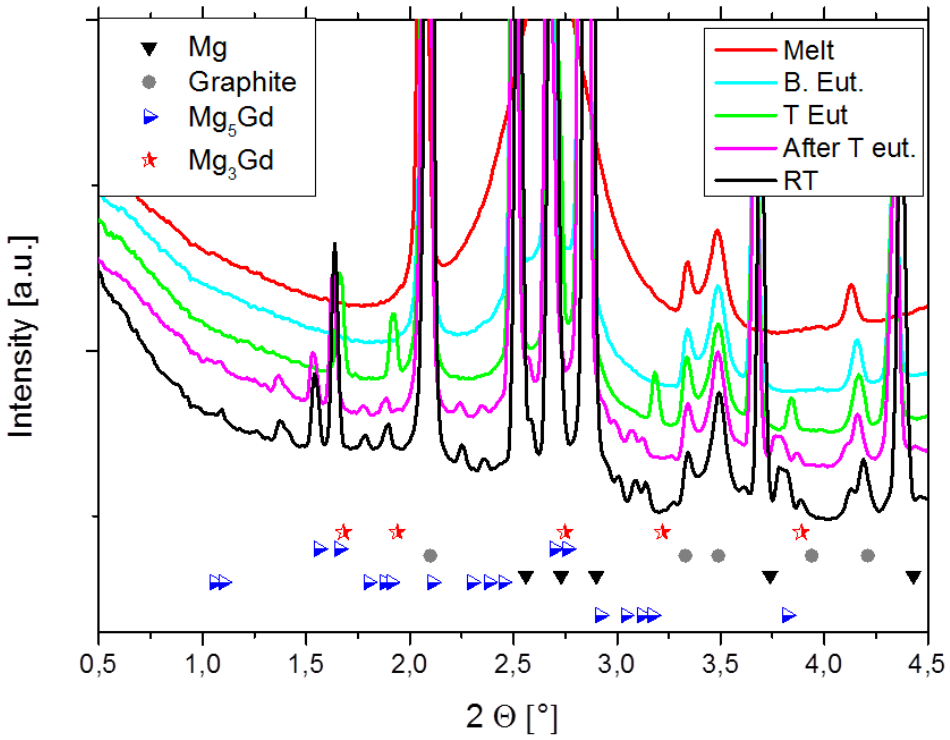

Figure 21. The solidification sequences of G15 alloy with a cooling rate of 20 K/min [139139]. The red line shows the melt, the light blue is the first sequence of the solidification (α-Mg), the green line was recorded at the eutectic temperature (formation of $GdMg_3$), the purple is taken ~5°C lower (the $GdMg_3$ transformation to $GdMg_5$) and the black line corresponds to the room temperature state.

In Figure 21 the red line (identified on the graph as: *Melt*) was recorded at a holding temperature of 720°C. The solidification sequence starts with the formation of α-Mg dendrites at T_L and only these peaks became more pronounced before T_E (light blue). As soon as the temperature hits T_E (green line) the rest of the liquid phase forms an eutectic structure with α-Mg and the secondary γ-phase (identified as $GdMg_3$). As no more liquid phase can be detected below T_E, the solidification finishes at this point, but the microstructure evolution advances further. Around five Kelvin below the T_E, peak shifts are visible on the major peaks of γ. This peak shift is presented with a purple line (*After T eut.*). Comparing the peaks of the new phase that forms to the most likely phases, the results suggest that the γ phase, which forms from the liquid is $GdMg_3$. However, this phase does not stay in the microstructure thus this is a metastable phase, which then transforms to $GdMg_5$ (β). $GdMg_5$ is the thermodynamically stable secondary phase of the Mg-Gd system as

presented in the binary phase diagram. These peaks did not change from T_E until the room temperature microstructure (*RT*) (black line) (Figure 25, Figure 26).

In Figure 22 the entire experiment is presented with the CR 100K/min on a time-2Θ diagram. As the sample is heated, the peaks/lines originated from the G15 alloy (α-Mg: indexed with light blue on the right side, and the intermetallic phase (IM) purple) disappears. The molten metal appears as a bright diffuse belt in the range where the three major lines (peaks) of α-Mg exist in solid state. The remaining lines mainly belong to the graphite crucible (red). The bottom part of the figure contains the t-T diagram and attached to the diffraction patterns. The formation temperatures observed are illustrated as yellow dashed lines to the t-T diagram. The yellow arrows show the major lines the intermetallic phase γ. As γ appears, the diffuse background from the liquid phase vanishes. The solidification ends. The lines of the secondary phase stay just a short temperature range after the solidification and then they disappear. At the same time the $GdMg_5$ phase appears and remains in the microstructure. The results of the overview indicate that the γ phase transforms into $GdMg_5$, which is the stable intermetallic phase of the binary Mg-Gd system on the magnesium rich side. The same can be observed in the 20 K/min CR solidification studies. This part of the graph with both CRs, where the transformation is observed, are enlarged in Figure 23. The temperature difference between the recorded T_L and T_E during the solidification give the solidification range (ΔT) of the G15 alloy. The visible grey level change after T_E on the graphs make it clear that there is no more liquid left, thus the diffused background reflection is no longer present.

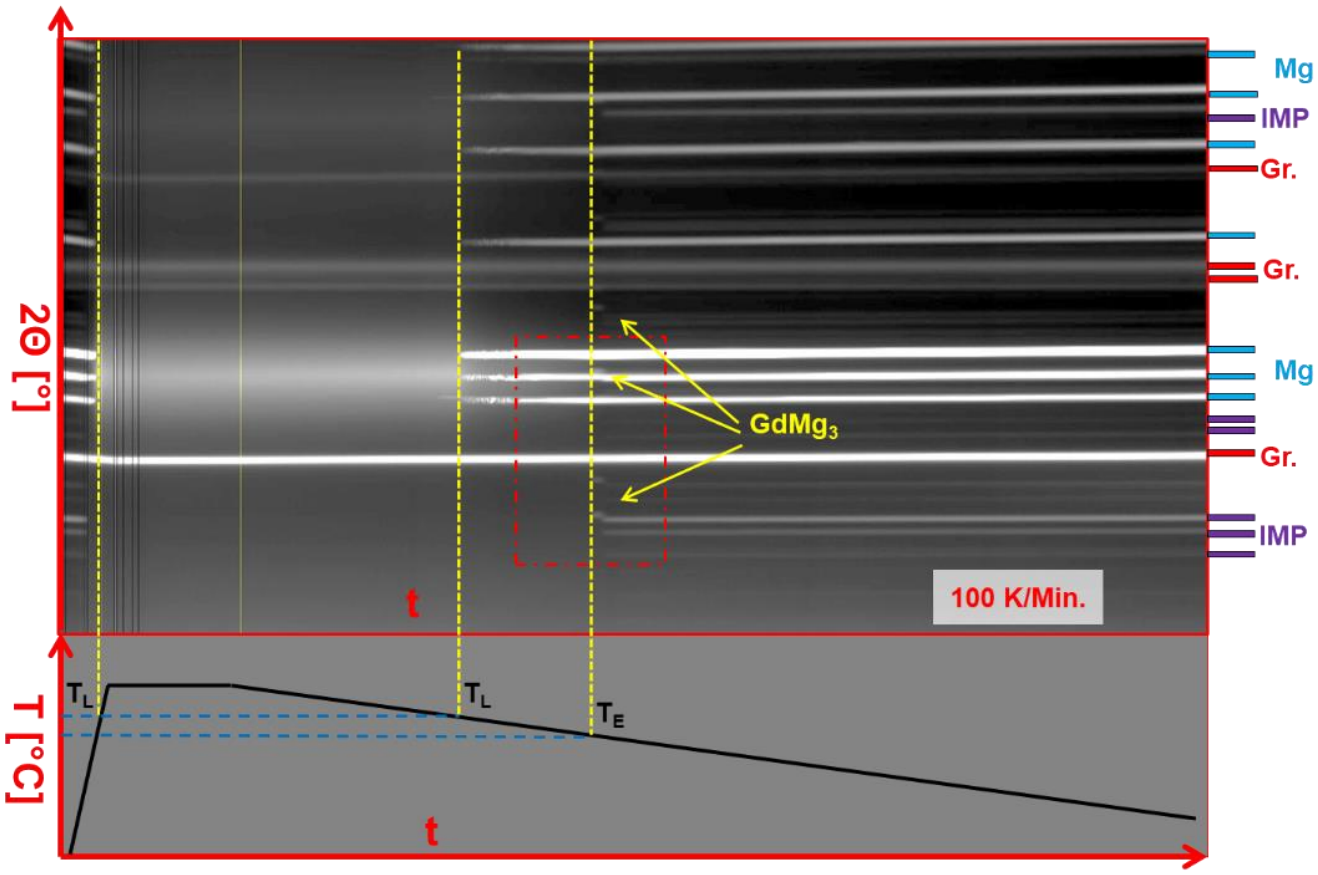

Figure 22. The overview of the SRXRD solidification experiment of the G15 with the cooling rate of 100K/min, and the time-Temperature program of the experiment. The yellow arrows show a solid phase transformation. The small red box is enlarged in Figure 23. During the heat up (left part of the picture) the peaks/lines of the sample (α-Mg: light blue, intermetallic phase: purple) disappear after overcoming the T_L, and start appearing just after cooling back to T_L (this temperature only α-Mg). In between peaks only from the crucible (red: Gr.) are visible. The peaks of the secondary phase are observed after reaching the T_E (yellow arrows) and the background radiation also drops at this temperature, indicates that the sample fully solidified. Further cooling results a solid phase transformation. The peaks of the secondary phase ($GdMg_3$) disappear and another intermetallic phase peaks appear ($GdMg_5$=IMP: purple).

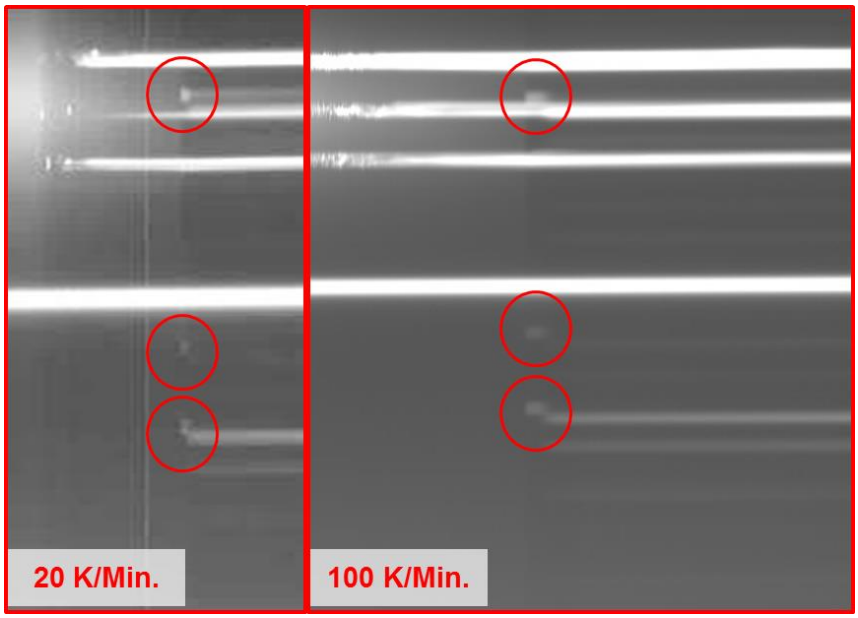

Figure 23. The enlarged (red box) section from the Figure 22 (right), and the same section of the experiment with 20 K/min CR is shown on the left. Both cooling rate shows the same secondary phase selection ($GdMg_3$) at T_E and solid phase transformation ($GdMg_3 \rightarrow GdMg_5$) afterwards.

The observed solid phase transformation is also visible on the raw 2D diffraction patterns Figure 24. The figure shows half of the recorded 2D patterns at two different temperatures, left side recorded at T_E and the white arrows point to rings which appear at T_E. These rings are the most intense diffraction rings of the $GdMg_3$ phase. The right side is recorded 4s later ~6°C below the eutectic temperature. The yellow arrows mark the rings of the $GdMg_5$ phase. The diffraction rings of the $GdMg_5$ are also phase present at room temperature.

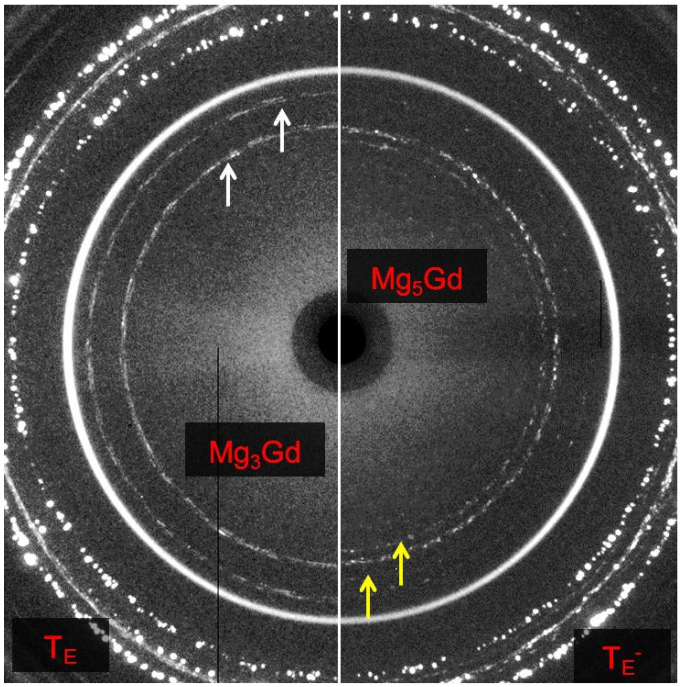

Figure 24. 2D SRXRD patters. Left side recorded at eutectic temperature (T_E). White arrows point those rings which appear at T_E ($GdMg_3$). The right side is recorded at ~6°C below the eutectic temperature (T_E^-). The yellow arrows mark the rings of the $GdMg_5$ phase.

The different CRs do not illustrate different solidification paths, but rather the microstructures are different in terms of the volume fraction of the intermetallic phases observed, as shown in Figure 25 and Figure 26, while the evaluated values of the volume fractions of the intermetallic phase is presented in Table 5-7. The two cooling rates produce the same features namely: the matrix, the eutectic structure and small bright Gd rich particles. These small brighter particles are present near the eutectic regions, but the volume fraction of these particles is lower than 0.1%. The chemical composition of the are similar at both cooling rates: ~10 at.% (~43 wt.%) and ~11 at.%

(~46 wt.%) Gd in sample with 20 and 100 K/min CR respectively. This indicates an atomic ratio of ~8:1 (Mg:Gd) in the eutectic region.

SEM-EDX analysis indicates that the chemical composition of the matrix is different between the two CRs. The average concentration of the Gd in the matrix is ~2 at.% (~13 wt.%) and ~1.5 at.% (~9 wt.%) with 20 and 100 K/min cooling rate respectively.

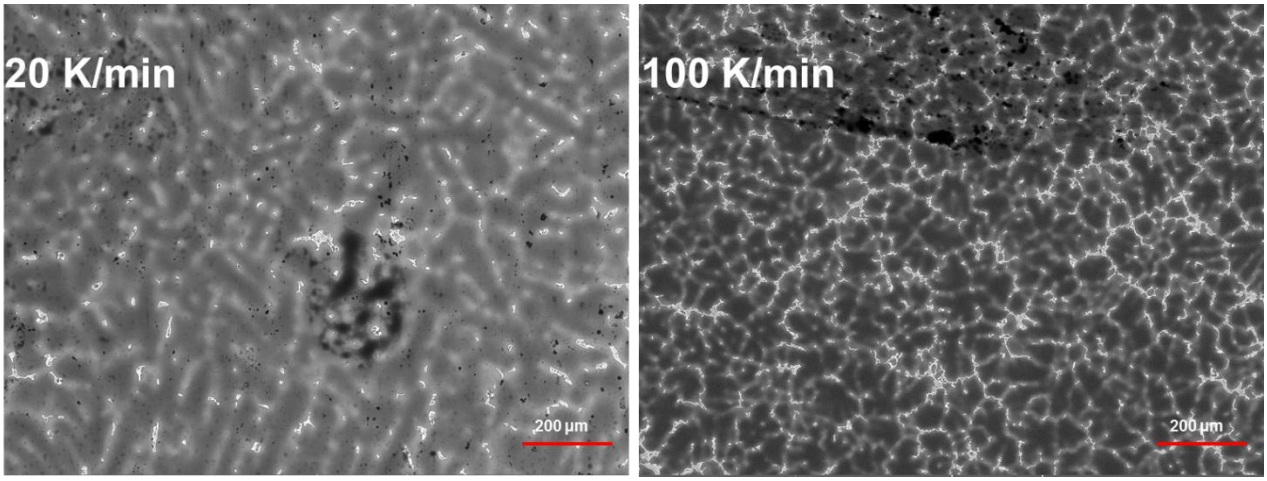

Figure 25. The resulted micrographs of the G15 alloy with both CRs. The left side is with 20K/min. while the right side is with 100 K/min cooling rate. The evaluated area fractions of IMP are presented in table 5-7. The darker areas (pores) were extracted from the total area.

Table 5-7. The results of the area fraction of the intermetallic phase (IMP) in the G15 alloy with the two examined cooling rates (20 and 100 K/min).

Alloy	**Cooling rate [K/min]**	**Area fraction of IMP [%]**	**Area fraction of contamination [%]**
G15	**20**	*4.9±0.04*	*0.1±0.02*
	100	*10.2±0.14*	*0.1±0.01*

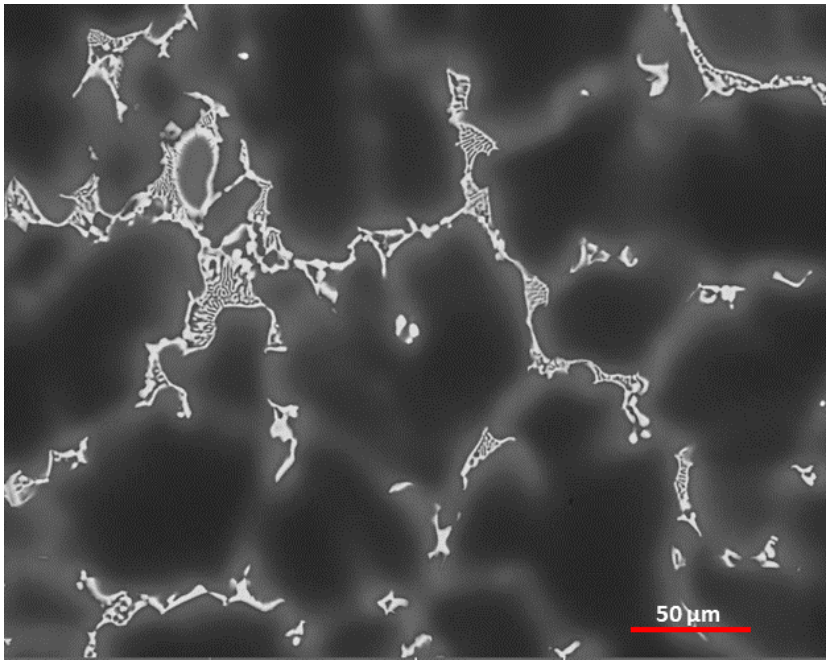

Figure 26. A higher resolution micrograph of the G15 alloy cooled at 100 K/min.

5.3.3 DSC results of the binary alloys

To determine the phase formation and transformation of the alloys, DSC measurements were performed. To compare the DSC results with the results from the SRXRD studies the 20 K/min cooling rate was used in the DSC work. The results of the measurements are presented in Figure 27. Thermal profiles for both alloys show two peaks during the solidification. The first peak, in both cases, is the formation of the α-Mg and the second peak is at the eutectic temperatures of the alloys where the intermetallic phase is expected to form along with eutectic Mg. The temperature difference between the first solidification of Mg and the eutectic solidification peaks determine the solidification range of the alloys (ΔT). The recorded temperatures and the calculated ΔTs are presented in Table 5-8.

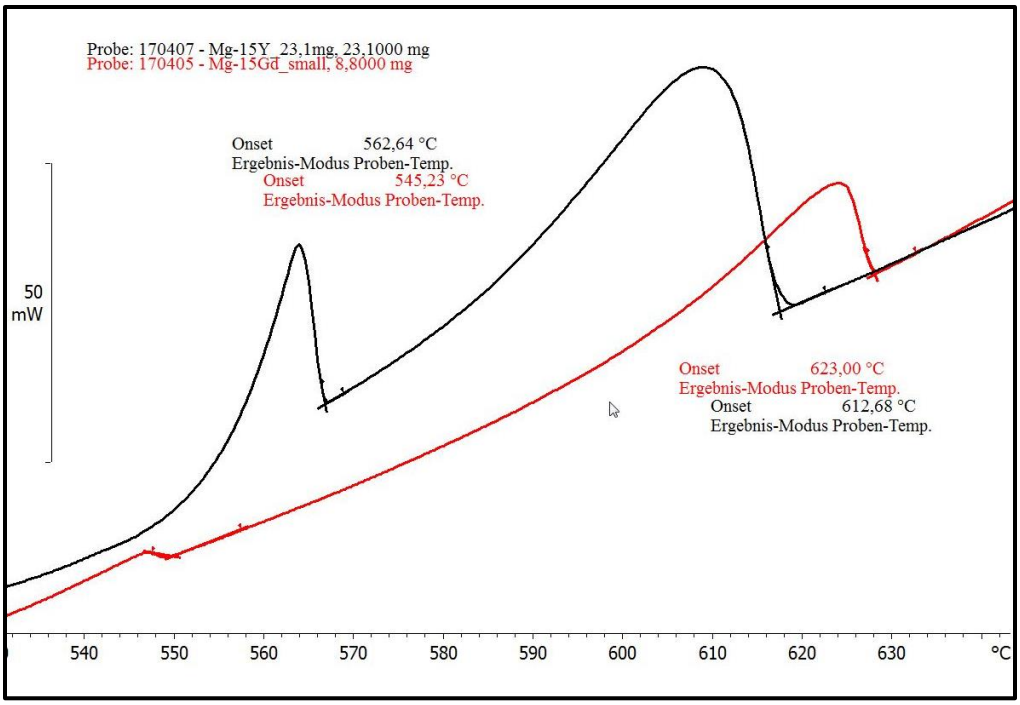

Figure 27. The DSC curves (temperature-heat flow) of the W15 (black) and G15 (red) alloys during solidification with applied 20 K/min cooling rate. Two exothermic reaction were recorded during the cooling of both samples. The first reaction is the crystallisation of α-Mg from the melt at T_L: 623°C in G15 and 612.7 °C in W15. The second reaction is the formation of the secondary phase together with the continuous formation of α-Mg at T_E: 543.2 °C in G15 and 562.6°C in W15.

5.3.4 Summary of the thermal analysis of the binary alloys

Two different types of solidification experiments were carried out on the binary alloys: SRXRD experiments with two CRs (20- and 100 K/min.) and a DSC experiment with one CR (20 K/min.). During the solidification experiment the phase formation/transformation temperatures were experimentally determined and solidification ranges (ΔT) were calculated. The results from both experiments are summarised in Table5-8.

Table 5-8. Experimentally determined temperatures of the phase formations in the examined binary alloys.

Alloy	**DSC [°C]**			**SRXRD [°C]**					
				20 K/min			**100 K/min**		
	T_L	**T_E**	**ΔT**	**T_L**	**T_E**	**ΔT**	**T_L**	**T_E**	**ΔT**
W15	*612.7*	*562.6*	*50.1*	*605.2*	*553.8*	*51.4*	*617.3*	*564.2*	*53.1*
G15	*623.2*	*544.5**	*78.7*	*640.2*	*561.1**	*79.1*	*593.7*	*513.4**	*80.3*

*Solid phase transformation is observed by SRXRD.

5.3.5 Solidification calculations using thermodynamic software for the binary alloys

The Pandat Thermodynamic software was used to calculate the expected liquidus, and eutectic temperature based on both the Lever rule and the Scheil models for both binary alloys. Both equilibrium (Lever rule) and non-equilibrium (Scheil-model) solidification paths were simulated and presented in Figure 32 and 33 for Mg-Y and Mg-Gd alloys. Since the models were meant to represent different conditions (diffusion stages) the results are expected to be different but comparable with the experimental results. Therefore, both of the calculations are used to evaluate the results.

The primary α-Mg appearance is predicted at 613 °C and the formation of the intermetallic phase (R_5Mg_{24} phase) is expected at 574 °C (as a calculated eutectic temperature of the Mg-Y binary system) in the case of the examined W15 alloy, with a calculated ~39°C solidification range (ΔT). The Scheil predicts a mole fraction of 13.64 % while the equilibrium calculation predicts 0.69% intermetallic phase for the W15 alloy (Figure 28). The mole fractions are more comparable than the mass fractions with the experimentally determined area fractions due to the great mass differences between the elements.

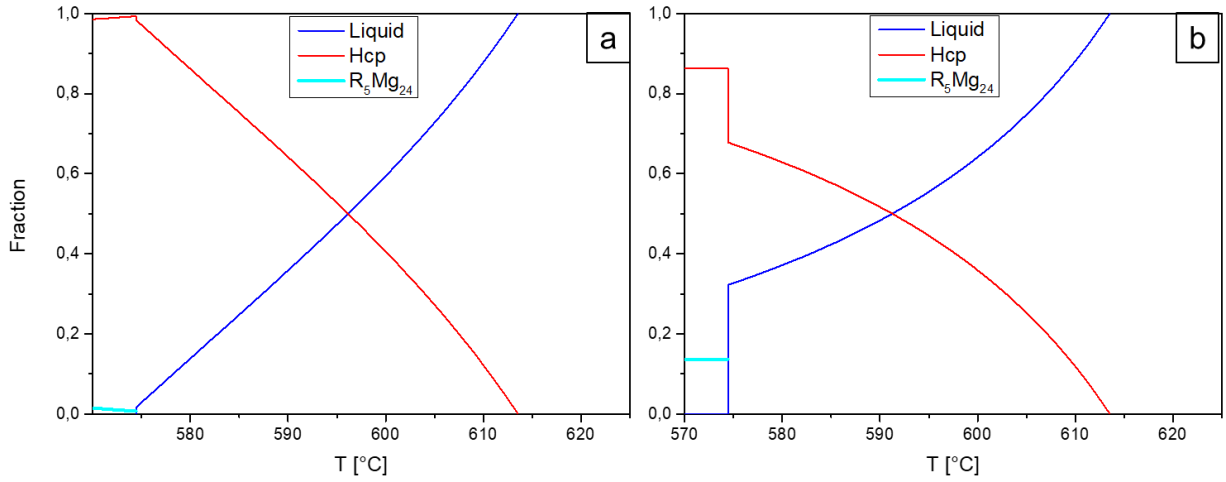

Figure 28. Change of the mole fractions during the solidification of W15 according to the calculations. The (a) represents the equilibrium solidification (Lever-rule) while the (b) shows the result of the Scheil calculation. Results are presented in Table 5-9 and Table 5-10.

In the case of the G15 alloy only Scheil calculation predicts any intermetallic phase formation with a mole fraction of 5.1 % at 547 °C. The secondary phase formed is the RMg_5 type phase ($GdMg_5$). The primary α-Mg formation is predicted at 623 °C, which provide a solidification range of ~76°C. The changes of the mole fractions during the solidification of G15 is presented in Figure 29. The calculated results are presented in Table 5-9 and Table 5-10.

Table 5-9. The calculated mole fractions of solid phases at the end of the solidification in the binary alloys.

Alloy	**Model**	**α-Mg [%]**	**IMP [%]**
W15	*Scheil*	*86.36*	*13.64*
	Lever	*99.31*	*0.69*
G15	*Scheil*	*94.9*	*5.1*
	Lever	*100*	*0*

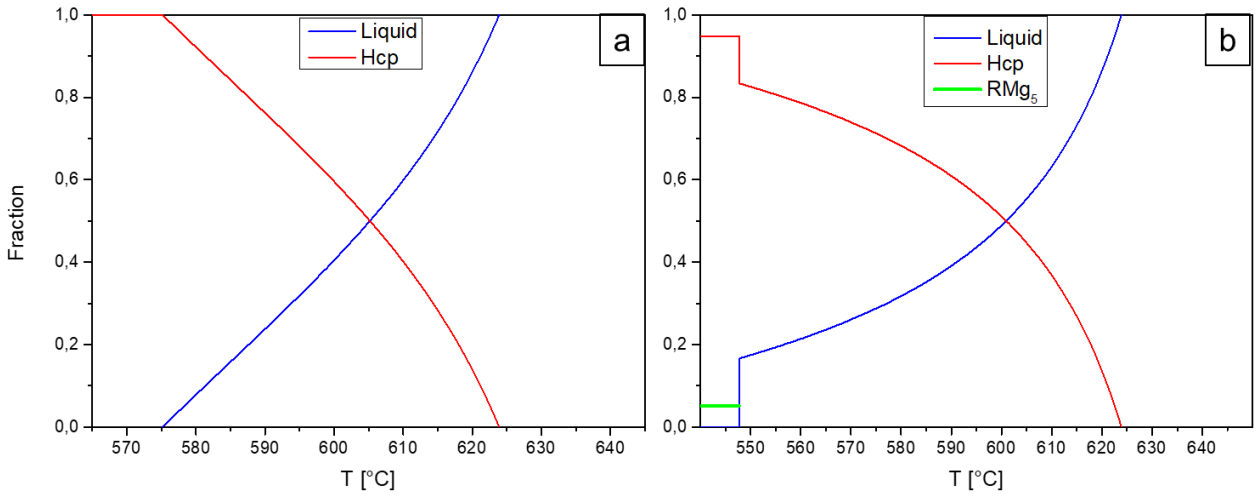

Figure 29. Change of the mole fractions during the solidification of G15 according to the calculations. The (a) represents the equilibrium solidification (Lever-rule) while the (b) shows the result of the Scheil calculation. Results are presented in Table 5-9 and Table 5-10.

Table 5-10. The calculated formation temperatures of the solid phases during the solidification of the binary alloys and their solidification ranges (ΔT).

Alloy and model		**phase evolution**		**Temperature of appearance [°C]**		**ΔT [°C]**
		Primary	Secondary	T_L	T_E	
W15	Scheil	α-Mg	R_5Mg_{24}	*613.2*	*574.4*	*38.8*
	Lever	α-Mg	R_5Mg_{24}	*613.2*	*574.4*	*38.8*
G15	Scheil	α-Mg	RMg_5	*623.8*	*547.8*	*76*
	Lever	α-Mg	-	*623.8*	-	*48*

5.4 As-cast microstructures of the ternary alloys

The microstructure characterization of the ternary as-cast alloys was performed with OM, SEM and TEM. For all investigations the middle part of the ingots was used. The as-cast micrographs are shown in Figure 30 (a-f).

The characteristic feature in the alloy structures is the presence of intermetallic phase(s) in the alloys containing yttrium and gadolinium as shown in Figure 30 b, d and f. The intermetallic phase is rich in RE and have typical eutectic structure. The darker grey areas, visible on the SEM micrographs, are segregated elements which solidify at lower temperature where there is a high level of solute may be contained in the Mg matrix. In addition to the eutectic structure, smaller bright particles are observed (pointed by the arrows). These particles are considered to be RERP. The average volume fractions of intermetallic phases were obtained from SEM-BSE micrographs and are summarised in Table 5-11.

Table 5-11. The area fraction of the intermetallic phases in the as-cast microstructures is presented.

Alloy	Area fraction of intermetallic particles [%]
WG105	*10.0±0.32*
WG77	*9.5±0.24*
WG510	*9.3±0.18*

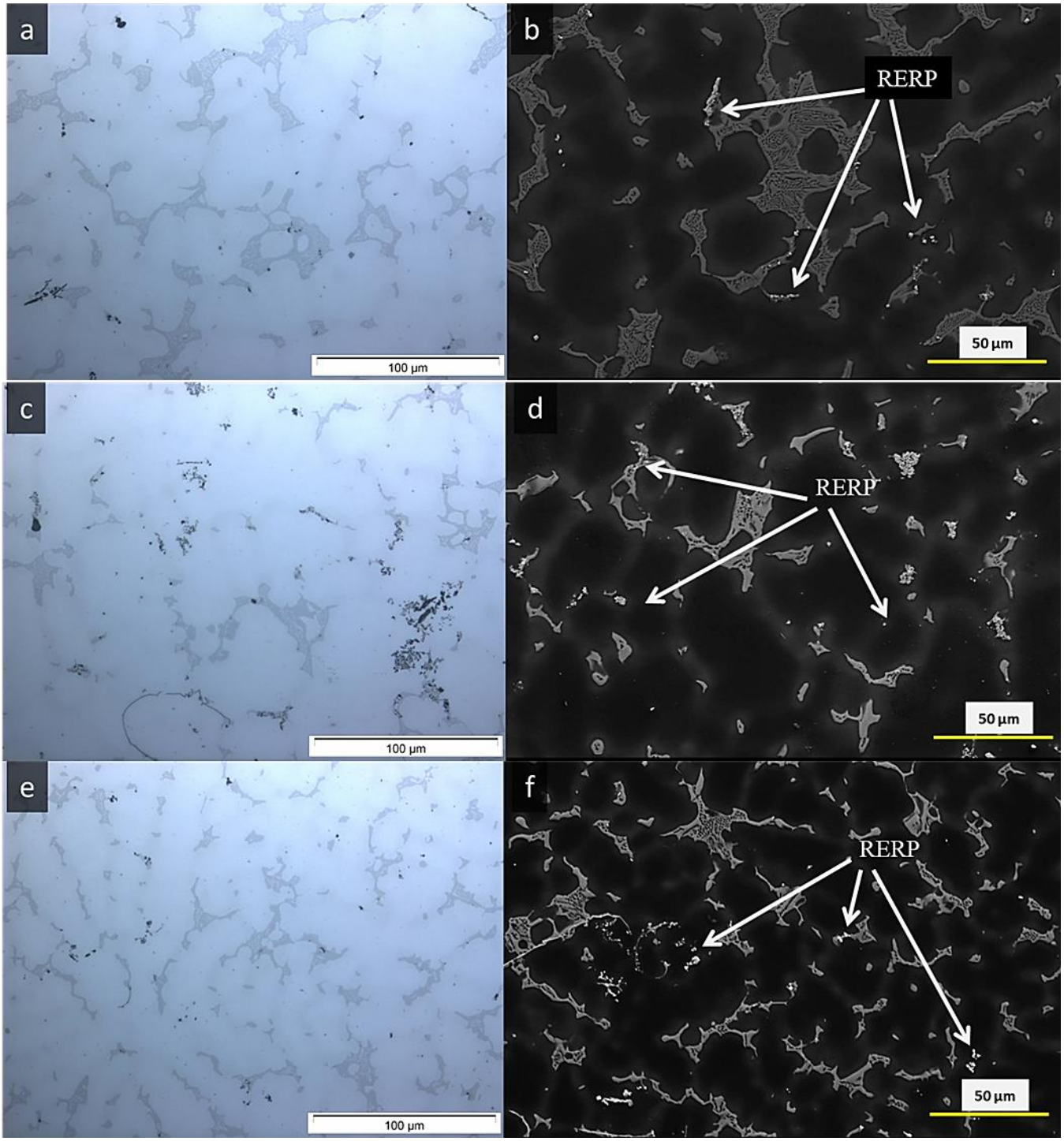

Figure 30. As cast microstructures of the WG105 (a-b), WG77 (c-d) and WG510 (e-f) alloys OM images are shown on the left and SEM BSE images are on the right. The brighter particles on the BSE images (RERPs) are dark black features on the OM micrographs.

SEM-EDX analysis was performed on each of the alloys investigated from an area of at least 100 μm x 100 μm to qualitatively compare the concentration of elements in the alloy. Point analysis of intermetallic phases and the core of the matrix (far from the eutectic structures or particles) was done. Although, a small amount of oxygen was detected in each spectrum, it is not included in the analysis. The obtained concentration values in weight percent are collected in Table 5-12.

Table 5-12. The SEM-EDX analysis results from the microstructures of the as cast samples both weight and atomic percent.

Composition	**Concentration (alloy) [wt.%]**		**Concentration (intermetallic) [wt.%]**		**Concentration (matrix) [wt.%]**	
	Y	**Gd**	**Y**	**Gd**	**Y**	**Gd**
WG105	*12.8*	*3.9*	*24.1*	*9.9*	*7.3*	*2.0*
WG77	*8.4*	*5.4*	*19.0*	*20.3*	*5.3*	*2.2*
WG510	*8.9*	*10.7*	*14.9*	*23.1*	*5.9*	*4.7*
Composition	**Concentration (alloy) [at.%]**		**Concentration (intermetallic) [at.%]**		**Concentration (matrix) [at.%]**	
	Y	**Gd**	**Y**	**Gd**	**Y**	**Gd**
WG105	*3.9*	*0.7*	*8.8*	*2.0*	*2.1*	*0.3*
WG77	*2.5*	*0.9*	*7.4*	*4.5*	*1.5*	*0.4*
WG510	*2.9*	*1.9*	*5.8*	*5.1*	*1.7*	*0.8*

5.4.1 TEM investigation of the intermetallic particles in the ternary alloys

The aim of the TEM investigation was to determine the intermetallic phase structure/type and to broadly estimate chemical composition in the ternary alloys. The major interest was how the addition of the Gd influences the evolution of intermetallic phases in as-cast microstructures and to see whether there is an associated lattice parameter change.

The TEM investigation of the WG105 is presented in Figure 31. The top part of the figure is a bright field (BF) micrograph of a typical intermetallic particle. From this particle EDX spectra

were obtained. A characteristic EDX spectrum from this intermetallic phase is presented in the middle of the Figure 31. The average results of the EDX analysis is presented in the Table 5-13. Micro beam electron diffraction (MBED) patterns were recorded from such intermetallic particles and analysed (bottom of the picture). The recorded MBED patterns can be characterised as the intermetallic phase type $(Y,Gd)_5Mg_{24}$ (Chapter 2.2) of the zone axis: <111> (left), <311> (middle) and <110> (right).

The TEM investigation of the WG77 alloy is presented in Figure 32. A BF micrograph was taken from a typical intermetallic particle of the microstructure (on the top). Under the BF image the EDX spectrum, recorded from the presented particle is shown. The average results of the EDX analysis is presented in the Table 5-13. From this selected particle micro beam electron diffraction (MBED) patterns were recorded and analysed (bottom of the picture). The recorded MBED patterns reveal that the investigated particle has a crystal structure of R_5Mg_{24} type phase. The diffraction patterns correspond to the zone axis: <110> (left), <111> (middle) and <311> (right).

The TEM analysis of the WG510 is presented in Figure 33. The top part of the picture is a BF micrograph of an investigated intermetallic particle from the microstructure. The recorded EDX spectrum from the particle is in the middle of the figure. The values of the EDX analysis is shown in the Table 5-13. The analysed micro beam electron diffraction (MBED) patterns are presented on the bottom of the figure. The recorded SAED patterns correspond to the intermetallic phase type of R_5Mg_{24} of the zone axis: <110> (left), <111> (middle) and <120> (right).

Similar microstructures were found in the three ternary alloys. The phases, constituting the eutectic structure, have been identified by SAED is the R_5Mg_{24} type phase. Although the increases of the Gd/Y ratio in the as-cast alloys does not influence the structure of the intermetallic phase, which is remains R_5Mg_{24}, but the Gd:Y ratio of the intermetallic phase change from ~1:3 to 2:1. Neither the SEM nor the TEM investigations indicated the presence of any other intermetallic phases addition to $(Y,Gd)_5Mg_{24}$.

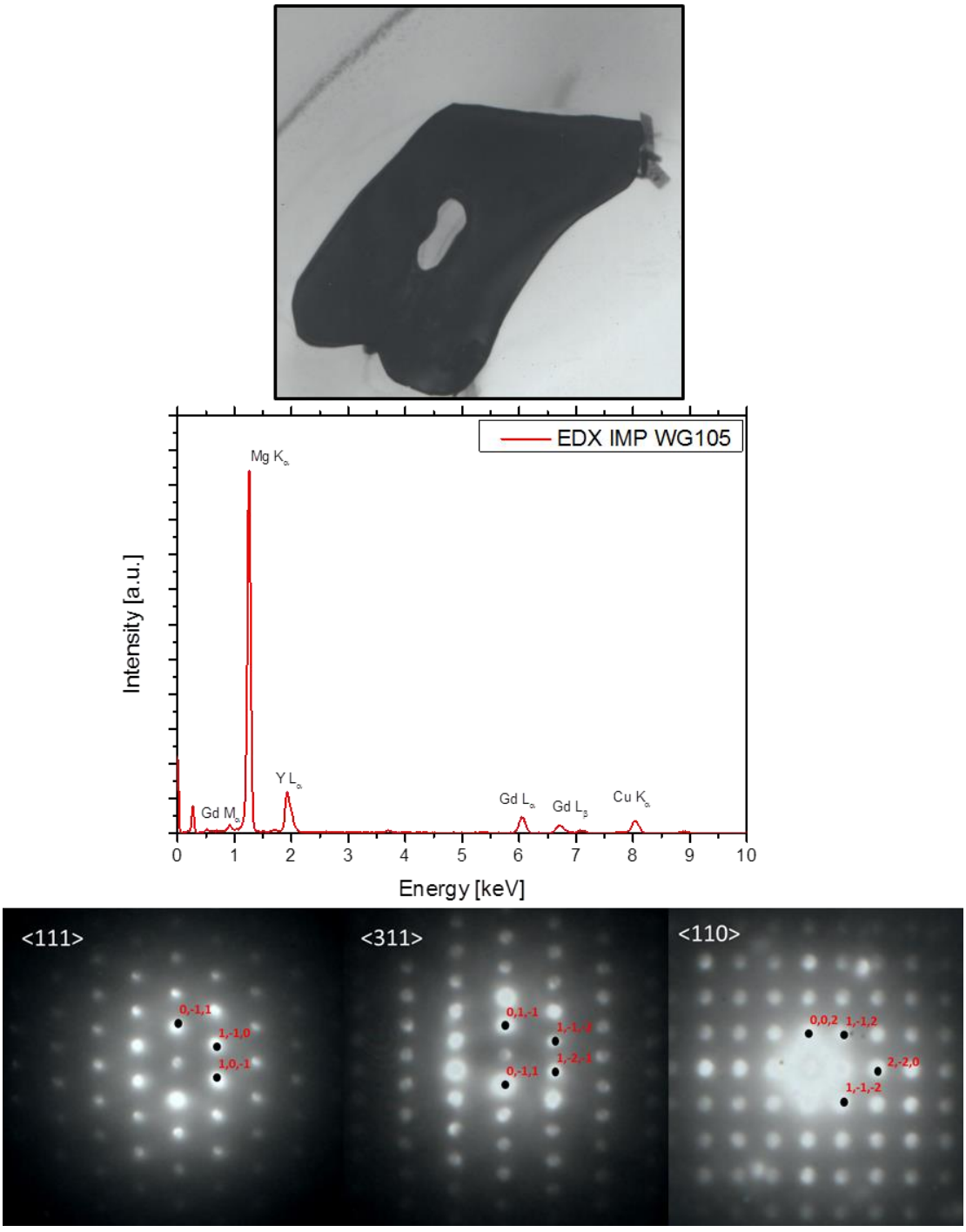

Figure 31. Bright field (BF) micrograph (top) of an intermetallic particle taken from WG105 alloy. The TEM-EDX spectrum of the intermetallic is seen in the middle. The SAED patterns of the intermetallic particles with three different zone axes which correspond to type R_5Mg_{24} phase.

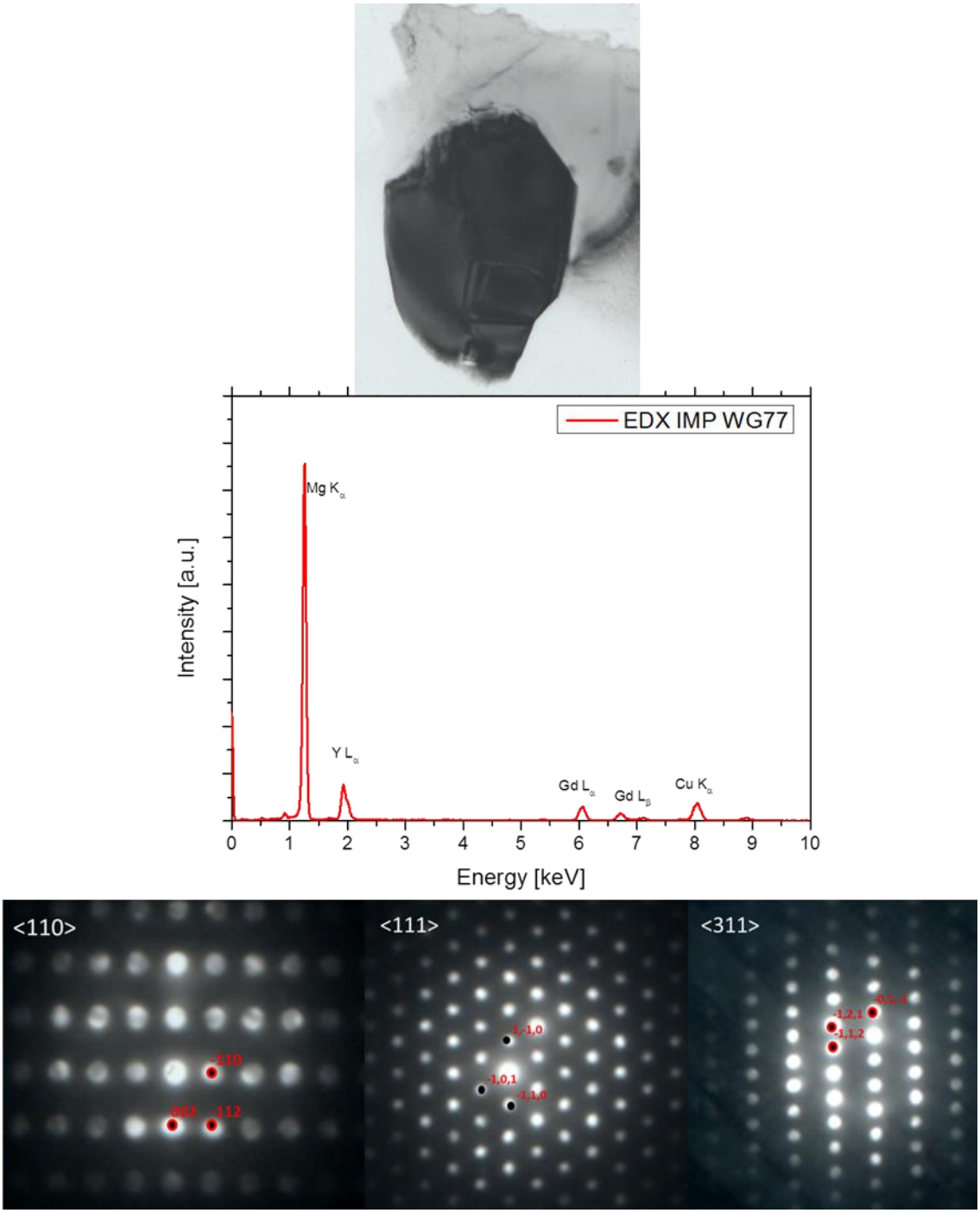

Figure 32. BF micrograph (top) of an intermetallic particle taken from WG77 alloy. The EDX spectrum of the intermetallic is seen in the middle. The SAED patterns of the intermetallic particles with 3 different zone axes which correspond to type R_5Mg_{24} phase.

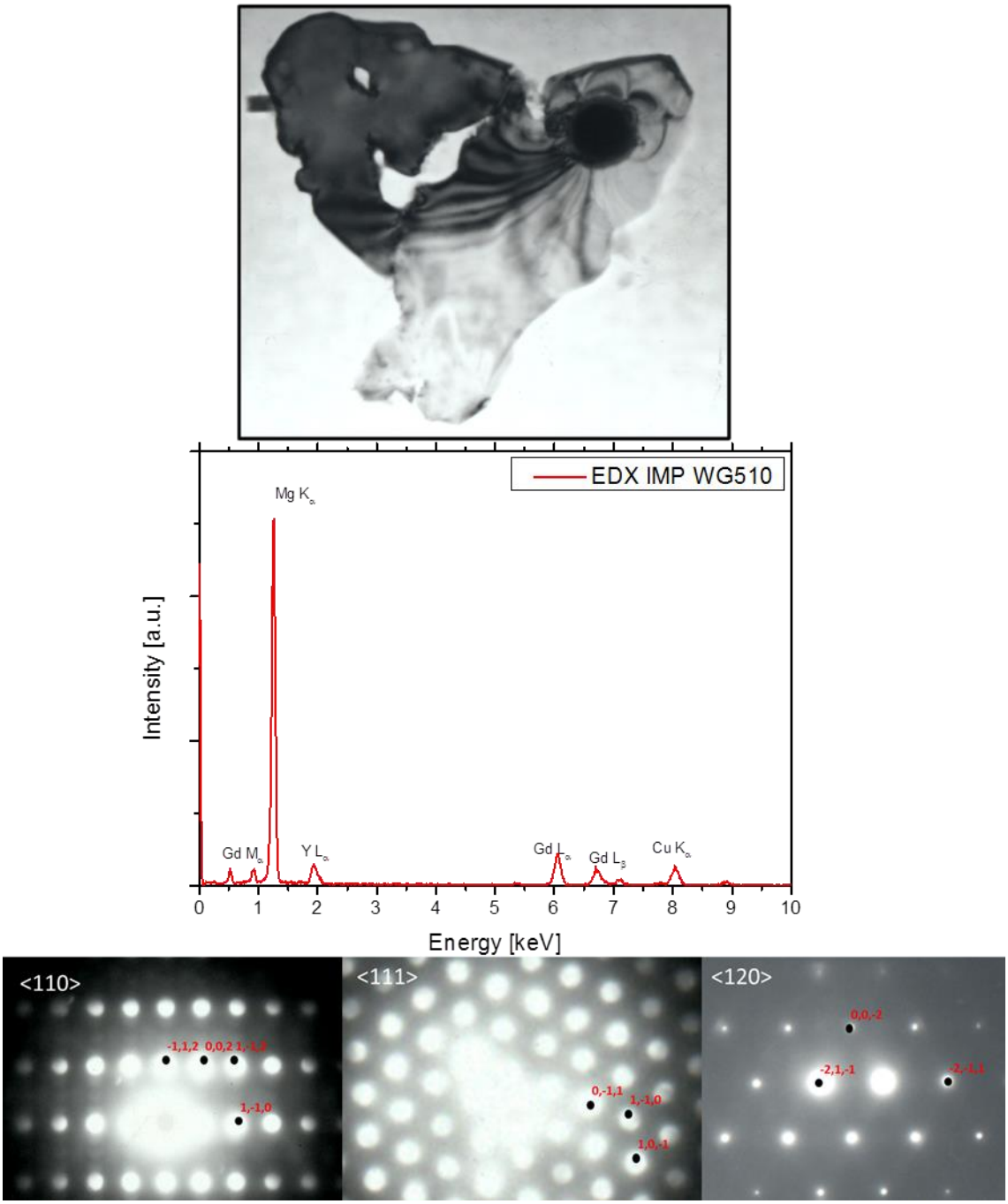

Figure 33. BF micrograph (top) of an intermetallic particle taken from WG510 alloy. The EDX spectrum of the intermetallic is seen in the middle. The SAED patterns of the intermetallic particles with 3 different zone axes which correspond to type R_5Mg_{24} phase.

Table 5-13 TEM-EDAX analysis results of the intermetallic phase structure type of R_5Mg_{24} from the microstructures of the as-cast ternary alloys.

Composition	**Concentration (intermetallic) [at.%]**		
	Y	**Gd**	**Mg**
WG105	*8.41±0.25*	*3.81±0.04*	*87.78±0.26*
WG77	*10.03±0.62*	*4.39±0.14*	*85.58±0.48*
WG510	*4.21±0.15*	*8.06±0.15*	*87.74±0.30*
Composition	**Concentration (intermetallic) [wt.%]**		
	Y	**Gd**	**Mg**
WG105	*21.65±0.69*	*17.32±0.19*	*61.02±0.18*
WG77	*24.53±1.39*	*18.96±0.63*	*56.51±0.32*
WG510	*9.99±0.37*	*33.79±0.58*	*56.22±0.21*

5.5 Solidification of the ternary alloys

5.5.1 *In situ* SRXRD investigations

WG105

The azimuthally integrated line profiles, of the 2D diffraction patterns acquired during the solidification experiments of WG105 alloy are shown in Figure 34. The line profiles presents the solidification experiments of the WG105 alloy in the same way as the solidification of the W15 alloy is presented (Chapter 5.3). During the experiments, three stages of solidification can be observed: molten stage, start of the solidification of α-Mg, and the end of the solidification with the formation of an eutectic phase transformation where α-Mg forms alongside intermetallic phase(s).

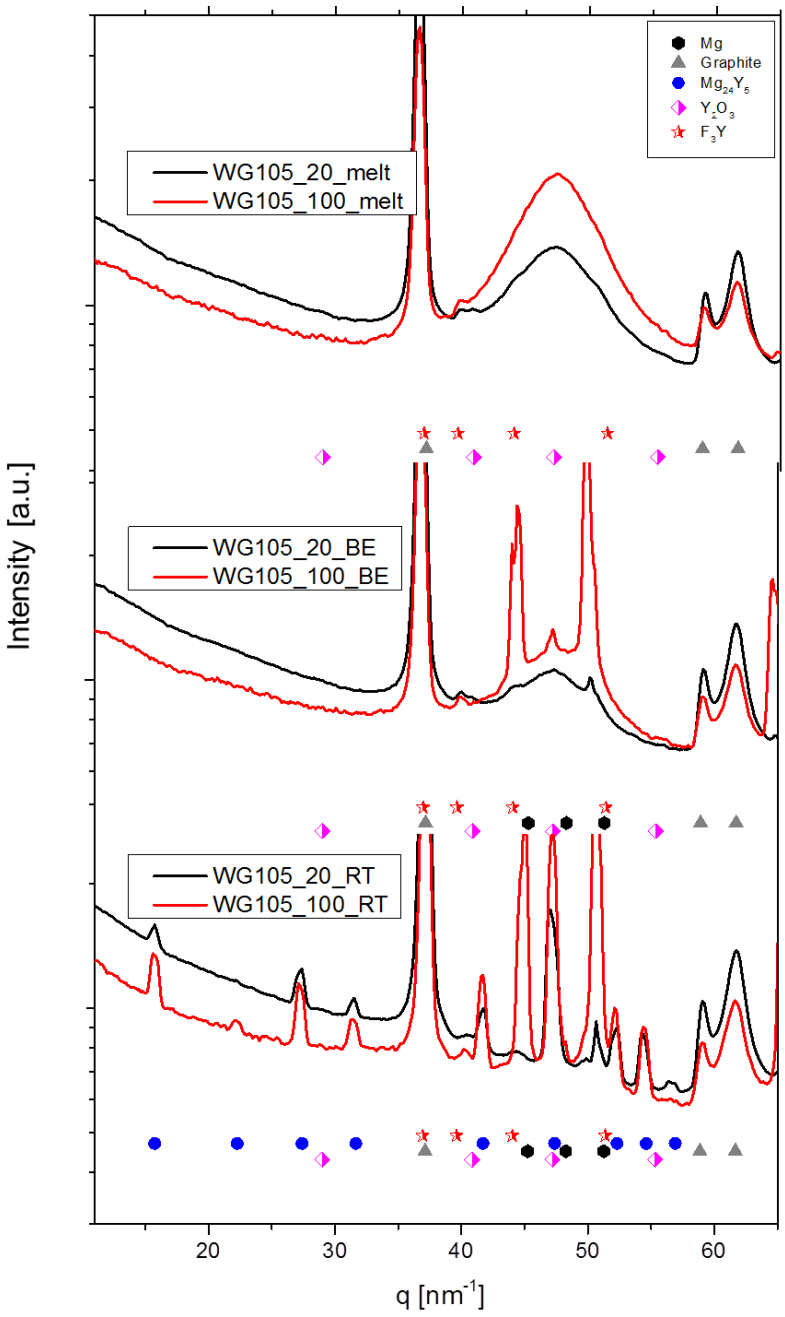

Figure 34. *In situ* solidification of WG105. Red lines correspond to the experiment conducted with a CR of 100 K/min and the black lines belong to the 20 K/min CR. Upside of the figure the molten state of the two experiments. In the middle part of the figure the partly solidified (liquid and α-Mg) state before the eutectic temperature and the bottom of the figure represent the fully solidified state. Symbols are used to index the major visible peaks of the observed phases.

The molten stage of the two different CRs measured from 720°C is shown in top of Figure 34. The diffuse background from the melt and peaks originate from the graphite crucible are the most apparent. However, some small additional peaks are also observed in the line profile and likely to corresponds to aforementioned Y_2O_3 and/or F_3Y phases (Chapter 5.3).

Second stage of the solidification is when the temperature reaches the liquidus temperature (T_L). At T_L the α-Mg starts to form from the liquid. With the decrease in temperature, the Mg peaks become more pronounced and Mg is the only phase that forms from the melt before the temperature reaches the temperature of the secondary phase formation (T_2).

At T_2, the third stage of the solidification, the formation of one intermetallic phase is observed. The peaks appearing can be indexed according to the R_5Mg_{24} type phase. At this temperature the system is fully solidified and there is no further phase transformation observed in the alloys (*RT*). The possible phases are indexed with symbols in Figure 34.

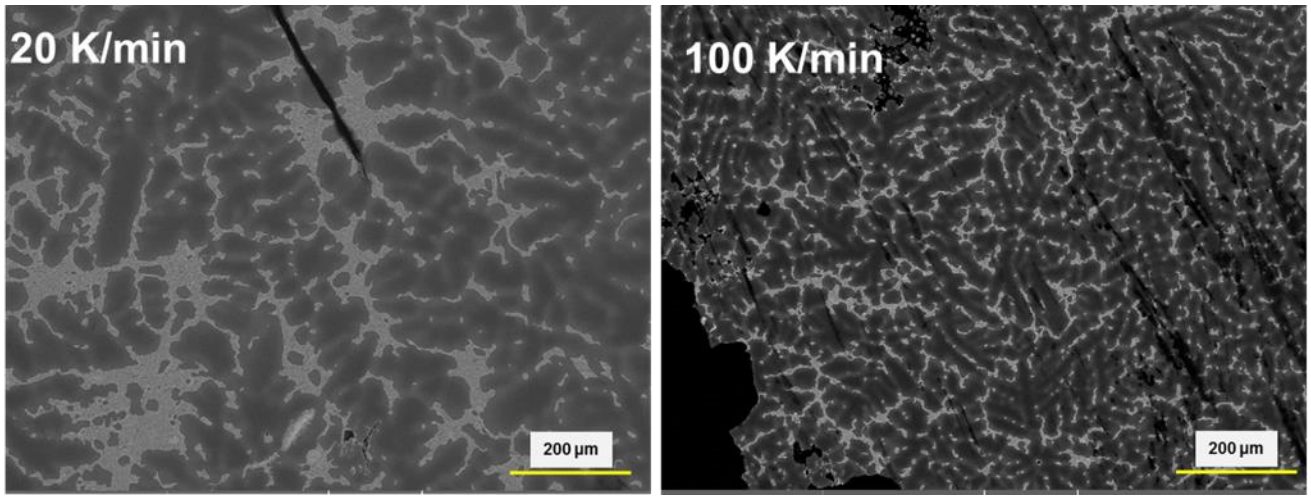

Figure 35. SEM BSE micrographs of WG105 alloy at both investigated CRs. The left side is with 20K/min while the right side is with 100 K/min cooling rate. The darker areas (pores) were extracted from the total area.

Although the different CRs do not result in different solidification paths in the alloy, the microstructures are different in terms of the area fraction of the intermetallic phase and concentration of particles (Table 5-14).

Table 5-14. Area fractions of the intermetallic phase (IMP) in the WG105 alloy at CR of 20 and 100 K/min and the area fraction of brighter RE rich particles (RERPs).

Alloy	Cooling rate [K/min]	Area fraction of IMP [%]	Area fraction of RERP [%]
WG105	**20**	*7.54±0.06*	*0.36±0.06*
	100	*11.42±0.16*	*0.76±0.01*

Specific areas of the as-solidified microstructure were investigated by SEM-EDX point analysis. The examination targeted three different characteristics of the microstructure: matrix, eutectic structure and rare earth rich particles. The two cooling rates produced similar features in the microstructure, however a slight difference in the chemical composition of the matrix is detected between the two cooling rates. Typical features are shown in an as-solidified sample cooled with a 100 K/min CR (Figure 36).

The average concentration of the magnesium in the core of matrix is ~2-3 wt. % higher in sample CR 20 than in sample CR 100. The point four in Figure 36 was taken from the matrix with a concentration of ~96 at. % (~91 wt. %) Mg and around ~7 wt. % of RE (rest is oxygen). This is lower compare to that of the binary alloys. The matrix has a (Y:Gd) atomic ratio of ~11:9 and ~9:8 in samples with CR 20 and 100 K/min respectively, which results a weight ratio of ~2:3 and ~5:8.

In this alloy the small RERP are finely distributed along the Eutectic region, which makes difficult to estimate the concentration of the eutectic structure. The point three was taken from eutectic with lower amount of brighter particles, with the exception of small amount of oxygen at ~3 at.% (~1.5 wt.%), this point consist of magnesium and the mixture of both alloying RE elements in a ratio of ~6:1 (Mg:RE). The Y:Gd atomic (weight) ratio in the eutectic region is ~1 (~1:2) and ~7:3 (4:3) in the specimens with CR of 20 and 100 K/min respectively.

Point one was taken from a segregated are in the corner of a larger eutectic region. This point has a high yttrium and gadolinium concentration (RERP) with a moderate presence of magnesium. The oxygen and fluorine concentrations are also high in this point. Point two was selected in the middle of a larger eutectic area with small RERPs. This area also has high concentrations of RE but no fluorine. The concentration of Y is generally several times higher than the concentration of Gd if fluorine is present.

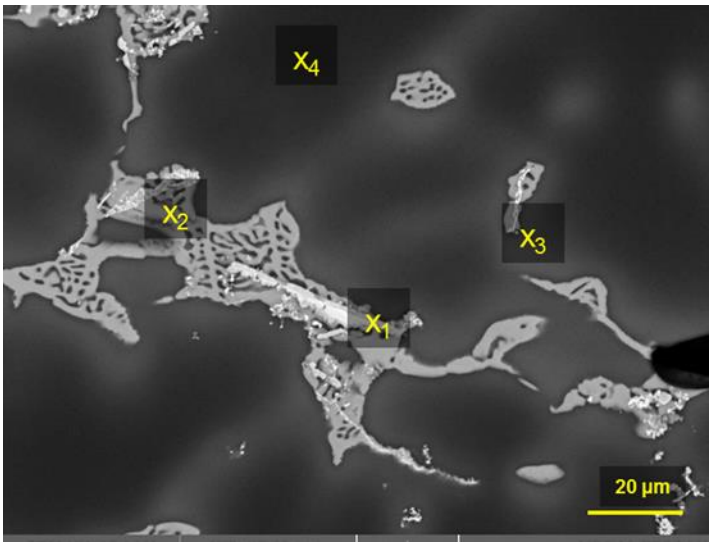

Figure 36. A higher magnification micrograph of the WG105 alloy cooled with 100 K/min where X_1-X_4 correlate with EDX point measurement regions (Table 5-15). The middle of the X shows the centre of the applied e-beam.

Table 5-15. The SEM-EDX point analysis of the typical observed microstructural features in WG105 alloy (Figure 42). The results are presented both atomic and weight percent.

	Concentration at. %				
	Mg	**Y**	**Gd**	**F**	**O**
X_1	*3.9*	*37.1*	*9.2*	*19.8*	*30*
X_2	*75.8*	*14.5*	*6.9*	-	*2.8*
X_3	*82.5*	*10*	*4.1*	-	*3.4*
X_4	*95.8*	*0.8*	*0.7*	-	*2.7*
	Concentration wt. %				
	Mg	**Y**	**Gd**	**F**	**O**
X_1	*1.7*	*58.1*	*25.3*	*6.6*	*8.4*
X_2	*43.3*	*30.3*	*25.4*	-	*1.1*
X_3	*55.8*	*24.7*	*17.9*	-	*1.5*
X_4	*91.3*	*2.9*	*4.1*	-	*1.7*

The experiment conducted at CR of100 K/min is presented as time-2Ɵ diagram with the time-Temperature program in Figure 37. The lines represent the peaks of the phases. Left side of the picture is the start of the experiment (as-cast condition), while the right side is the as-solidified microstructure. The peaks are indexed on the right side of the graph with coloured lines (α-Mg: light blue, R_5Mg_{24} (IM): purple, crucible (Gr): red, and Y_2O_3: yellow).The peaks/lines of the α-Mg and IM disappears during heating (from left to right) and the molten metal appear as dispersed belt in the range where the three major lines (peaks) of α-Mg are exist in solid phase. The remaining lines belong to the graphite crucible and small amount of Y_2O_3. Diffraction lines due to Mg start appearing again when the temperature reaches the T_L. The lines get more pronounced and the diffused region of diffraction due the liquid reduced as the Mg lines became more prominent. As the temperature reached T_2 the lines of the same secondary phase observed in the as-cast condition appears again. The visible grey level change after T_2 is indicative of the consumption of all liquid with the formation of the eutectic structure. The bottom part of the figure show the time-temperature diagram and follows the time line for the 2θ-time diagram presented. The observed

formation temperatures are projected on to the t-T diagram with yellow dashed lines. The difference in temperature T_L and T_2 provides the solidification range (ΔT) of alloy.

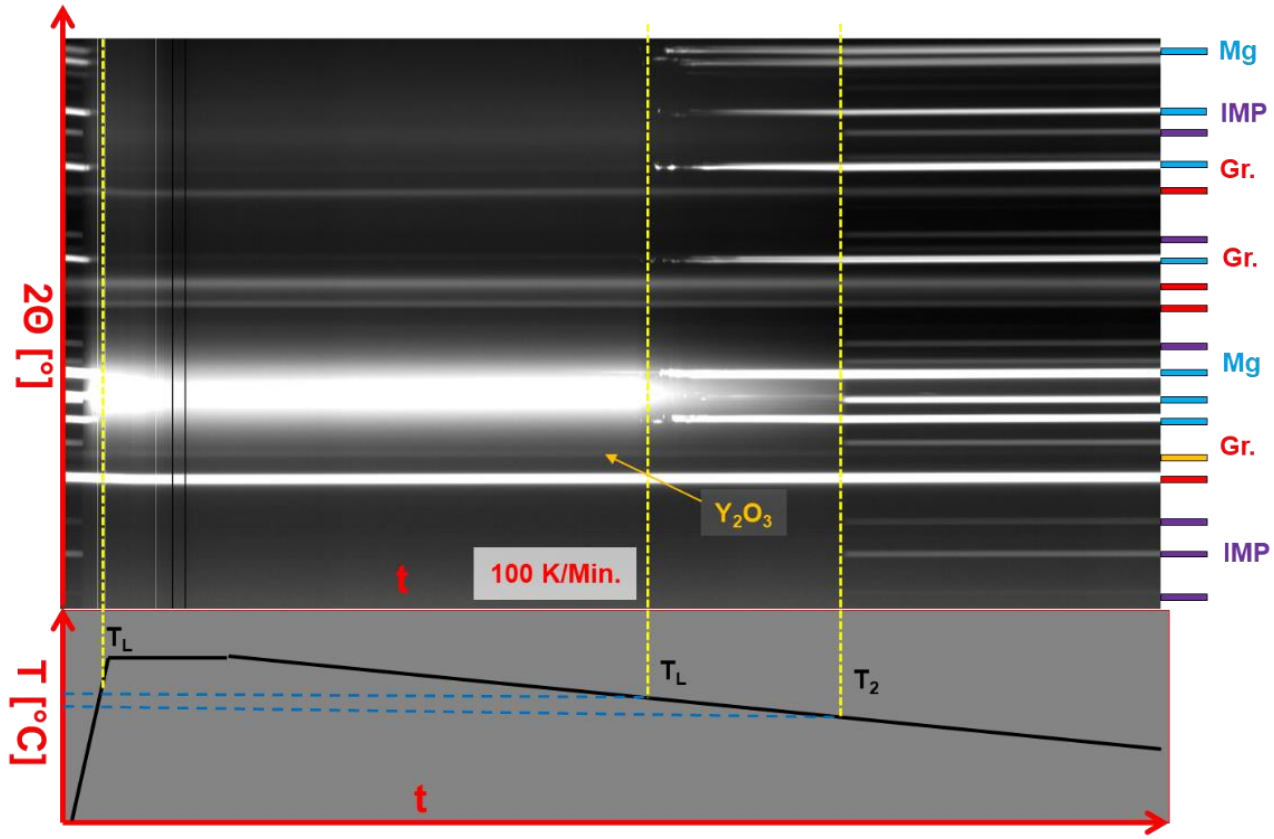

Figure 37. The overview of the SRXRD solidification experiment of the WG105 with the cooling rate of 100K/min, and the time-Temperature program of the experiment. During the heat up (left part of the picture) the peaks/lines of the sample (α-Mg: light blue, secondary phase: purple) disappear after overcoming the T_L, and start appearing just after cooling back to T_L (this temperature only α-Mg). In between peaks from the crucible (red: Gr.) and probably Y_2O_3 peaks (yellow arrows) are visible. The peaks of the secondary phase are observed after reaching the T_2 and the background radiation also drops at this temperature, indicates that the sample fully solidified.

WG77

The solidification of the WG77 alloy has three different distinct regions:

1. melt: this part from the holding temperature (T_H) till the liquidus temperature (T_L),

2. sequence 1: first region of solidification, from T_L to T_2 (secondary phase formation)
3. sequence 2: formation of secondary phase in an eutectic structure and completion of solidification, at T_2.

The azimuthally integrated line profiles of the 2D diffraction patterns acquired from the solidification experiments of WG77 alloy are shown in Figure 38. The results are presented in the same manner as with previous alloys.

The completely molten state of alloys at both CRs a shown in the top of Figure 38. As the alloys are molten, a diffuse background originating from the melt and diffraction peaks of the graphite crucible are observed. Although, some small differences between line profiles may be observed due to inhomogeneities in the specimen s, but the differences are more pronounced in this experiment. The diffraction patterns of the specimen used for the 100 K/min experiment shows some unexpected peaks, which fit to the peaks of Y_2O_3 and/or F_3Y phases. The intensities of these peaks increase during the first step of the solidification. The intensity of these peaks more intense in the liquid state than that observed in the as-cast alloy used in the beginning of the experiment and they are significantly intense than the same peaks observed in the sample examined at 20 K/min CR.

At the liquidus temperature α-Mg starts to form from the liquid. With the decrease in temperature, the Mg peaks become more pronounced and Mg is the only phase that forms from the melt before the solidus/eutectic temperature (T_2). This is illustrated in the graph at the middle of Figure 38.

The second and last sequence of the solidification (bottom part of Figure 38) is the formation of an intermetallic phase and some of the remaining liquid transforms into α-Mg. These peaks are indexed according to R_5Mg_{24} phase. At T_2, the system is fully solidified and there is no further phase transformation observed in the alloys below T_2 (*RT*).

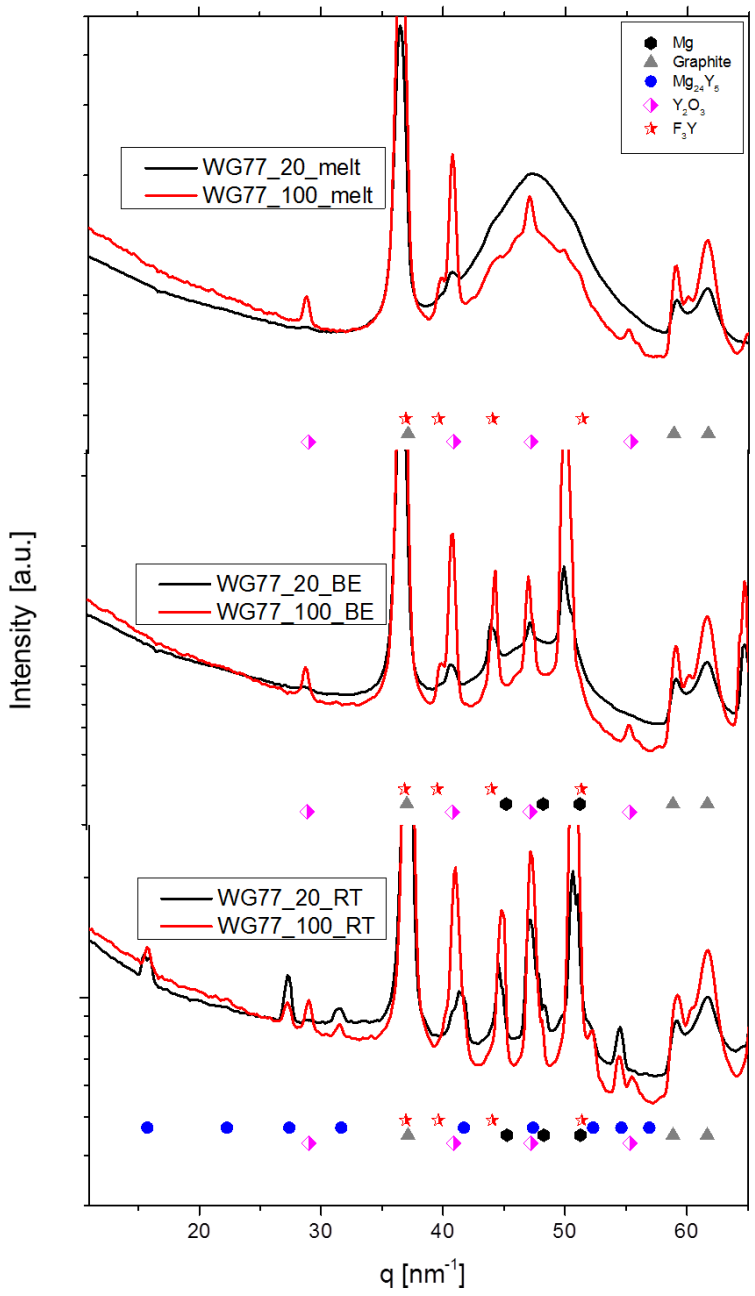

Figure 38. The results of the in situ solidification experiments of WG77. Red lines correspond to the experiment conducted with 100 K/min CR and the black lines belong to the 20 K/min CR. Upside of the figure the molten state of the two experiments. In the middle part of the figure the partly solidified (liquid and α-Mg) state before the eutectic temperature. And the bottom of the figure represents the fully solidified state. Symbols are used to index the major visible peaks of the observed phases.

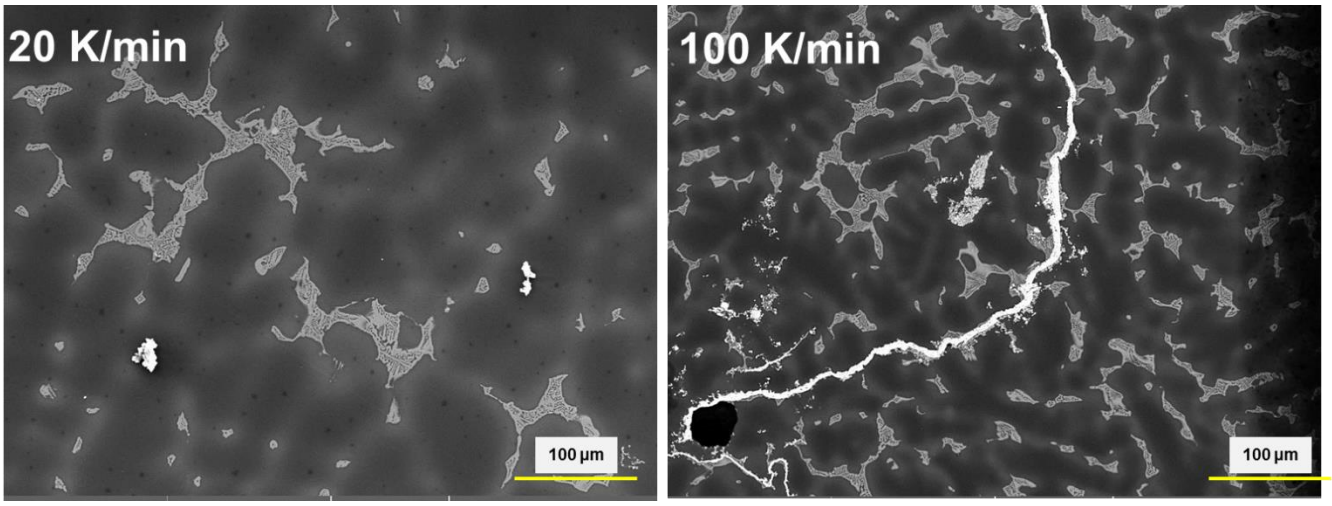

Figure 39. The resulted micrographs of the WG77 alloy with both CRs. The left side is with 20K/min. while the right side is with 100 K/min. cooling rate. The brighter features on the micrographs are RERPs. The dark black areas are pores, those areas were extracted from the total area. The evaluated area fractions of IMPs are presented in table 5-16.

The solidification sequences are the same for both CRs (and similar to that of W15 and WG105) and the same type of phases is identified. However, the volume fraction of the intermetallic phases observed show significant differences between the two cooling rates. The most obvious difference is the presence of RE rich particles (RH_2) or the presence of oxide and fouride films. The volume fraction of the RERP was calculated to be approximately four times higher in the sample examined at 100 K/min CR compared with the sample at 20 K/min CR. The SEM micrographs presents the differences in Figure 39 and the measured volume fractions of the intermetallic particles are presented in Table 5-16.

Table 5-16. The results of the volume fractions of the intermetallic phase (IMP) in the WG77 alloy with the two examined cooling rates (20 and 100 K/min.), and the area fraction of RERPs.

Alloy	**Cooling rate**	**Area fraction of IMP [%]**	**Area fraction of RERPs [%]**
WG77	**20**	*4.32±0.16*	*0.42±0.01*
	100	*9.51±0.13*	*1.78±0.02*

The two resultant microstructures exhibit the same typical features despite the presence of the different volume fractions of intermetallic particles and the presence of RE rich particles or oxide/fluoride particles. The sample cooled at 100 K/min has higher volume fraction of

intermetallic particles and RE rich particles, therefore that microstructure is used to represent the characteristic of the as-solidified microstructures and to show typical results from SEM-EDX analysis, Figure 40. The quantified EDX results from typical points investigated are shown in Table 5-17.

The matrix has an average Mg concentration of ~97 at.% (~90 wt.%) for both cooling rates. It means that the average concentration of RE are ~10 wt.%. The Y:Gd atomic (weight) ratio in the matrix is: ~7:5 (~7:9) and ~5:1 (~3:1) with CR of 20 and 100 K/min respectively. The amount of Gd is much lower in the matrix of the sample at CR of 100K/min. Point four in Figure 35 was taken from the matrix in that sample with a detected Gd concentration of 0.4 at.% (~2.5 wt%).

The eutectic structure in the WG77 alloys has an Mg:RE atomic ratio of ~8:1 with a Mg concentration of ~89 at.% (~64-70 wt.%) in the as-solidified samples. These values are comparable with results from W15 and WG105. Additionally, the eutectic structure consists of α-Mg and the intermetallic phase R_5Mg_{24}. The Y:Gd ratios in the eutectic structure are different between the two different cooling rates. The atomic (and weight) ratio of Y:Gd in the eutectic structure is: 5:4 (5:7) and ~51:1 (~26:1) in the samples with CR 20 and 100 K/min respectively.

The EDX analysis point 1 was taken from an area that contain an agglomeration of small particles. This area has a high concentration of Y with a moderate level of Gd. The EDX point 3 was recorded from a segregated are alongside of a larger eutectic region. This segregation looks like a agglomeration of film of fine scaled particles in the microstructure which was left in the liquid until the last liquid solidified (Figure 39 right and Figure 40). This feature consisted mainly of yttrium, fluorine and oxygen. The EDX analysis point five was selected from the middle of a larger eutectic region in next to such agglomeration of particles. This area also contained a high concentration of yttrium, fluorine and oxygen but a very low concentration of gadolinium. The same features are observed in the sample cooled with 20 K/min CR, but the volume fraction of such features are lower.

The level of gadolinium detected in the sample with 100 K/min CR is significantly lower than in the 20 K/min. The average Gd concentrations are ~1.5 wt.% (~0.3 at.%) and ~6.5 wt.% (~2 at.%) at CR of 100 and 20 K/min respectively.

Table 5-17. The SEM-EDX point analysis of the typical observed microstructural features in WG77 alloy (Figure 40). The results are presented both atomic and weight percent.

Point	**Concentration at. %**				
	Mg	**Y**	**Gd**	**F**	**O**
X_1	*62.8*	*22.4*	*0.3*	-	*14,7*
X_2	*89.5*	*10.4*	*0.2*	-	-
X_3	*4.1*	*44.8*	*0.3*	*17*	*34*
X_4	*97.4*	*2.1*	*0.4*	-	-
X_5	*23*	*29.9*	*0.2*	*21,4*	*25,1*
Point	**Concentration wt. %**				
	Mg	**Y**	**Gd**	**F**	**O**
X_1	*40.5*	*52.9*	*1.2*	-	*6.2*
X_2	*69.9*	*29.7*	*1.1*	-	-
X_3	*2.1*	*80.3*	*0.8*	*6.5*	*11*
X_4	*92.4*	*7.3*	*2.5*	-	-
X_5	*14.2*	*65.6*	*0.7*	*10*	*9.9*

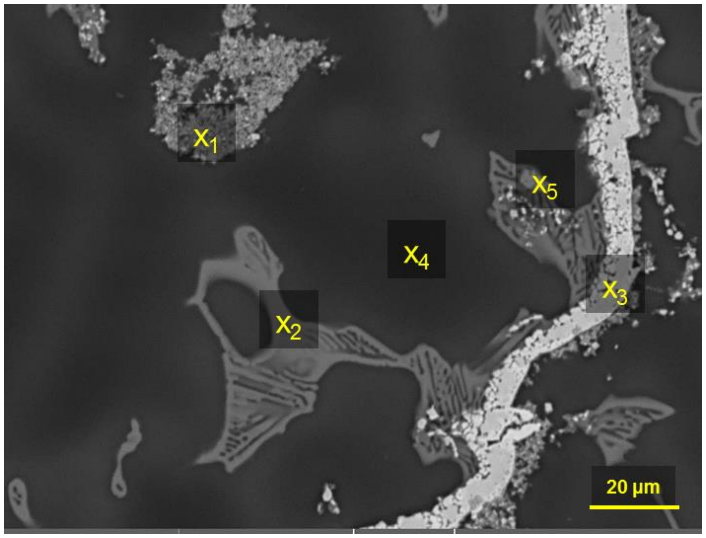

Figure 40. A higher magnification micrograph of the WG77 alloy cooled with 100 K/min. The EDX point analyses of the particles are shown in Table 5-17. The middle of the X shows the centre of the applied e-beam.

The time-2Θ diagram with the time-Temperature program is summarised for the 100 K/min CR in Figure 41. On this image the entire experiment is presented. RE-oxides or hydrates (yellow) are more visible during this experiment than in any other alloy investigated. However, the experiment confirming that microstructure consist of the same phases after and before the experiment.

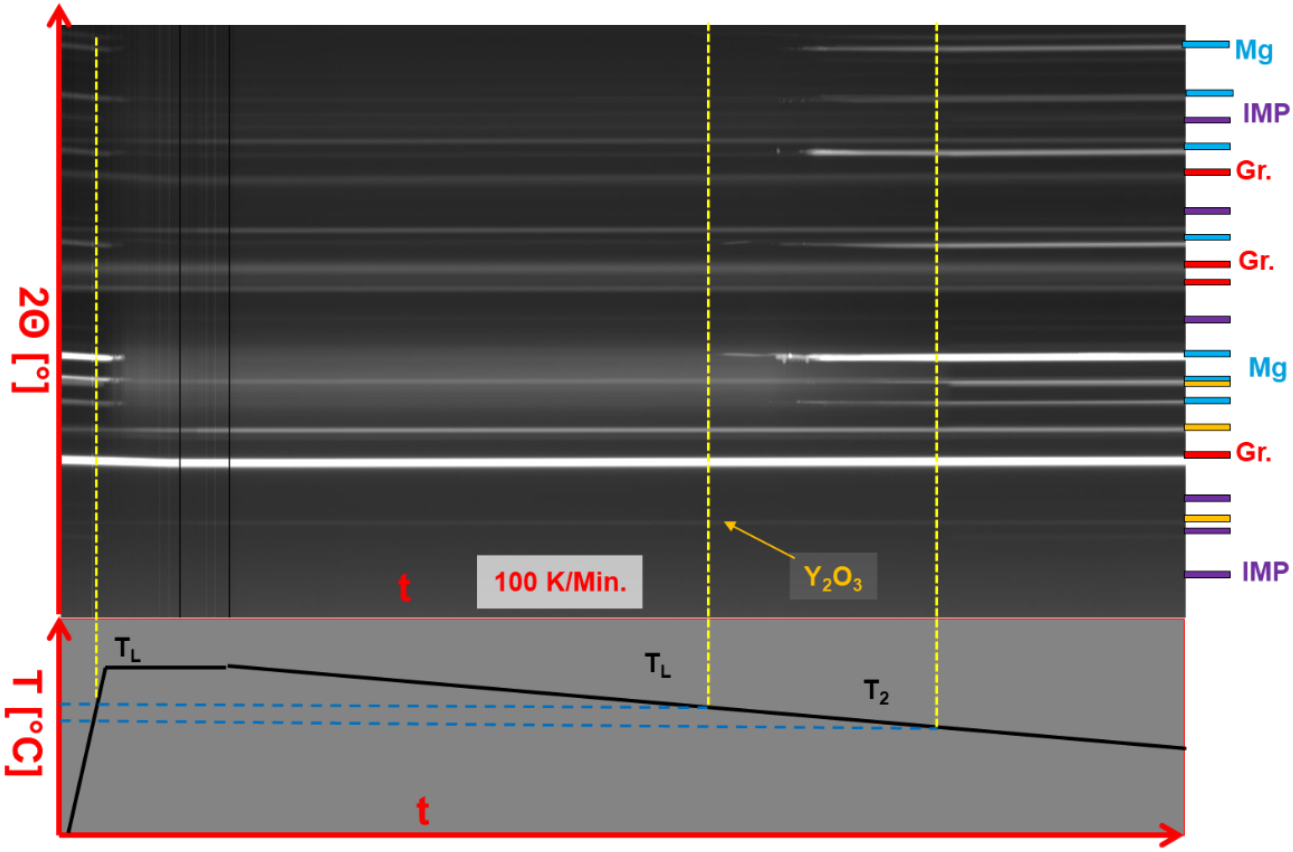

Figure 41. The overview of the SRXRD solidification experiment of the WG77 with the cooling rate of 100K/min, and the time-Temperature program of the experiment. During the heat up (left part of the picture) the peaks/lines of the sample (α-Mg: light blue, secondary phase: purple) disappear after overcoming the T_L, and start appearing just after cooling back to T_L (this temperature only α-Mg). In between peaks from the crucible (red: Gr.) and probably Y_2O_3 peaks (yellow arrows) are visible. The peaks of the secondary phase are observed after reaching the T_2 and the background radiation also drops at this temperature, indicates that the sample fully solidified.

WG510

Figure 42 summarizes the results from the *in-situ* solidification experiments of the WG510 alloy using SRXRD. The figure presents the azimuthally integrated line profiles, of the 2D diffraction patterns acquired during the experiments at 20- (black lines) and 100 K/min (red) CRs. The x scale of the graph is the reciprocal lattice parameter (q [nm^{-1}]) and the y scale is the normalised intensity. The solidification experiments consist of three steps with both cooling rates, however they proceed differently. The three stages of the solidification:

1. melt,
2. first appearance of a solid phase
3. end of the solidification with an formation of additional solid phase(s) at T_2.

In the molten phase (Figure 42 graph at the top of the figure) shows no significant difference between the two cooling rates. With the exception of peaks of the graphite crucible the molten background is the very pronounced with small peaks of possible contaminants (Y_2O_3 and/or F_3Y phases).

As soon as the temperature rich the liquidus temperature (T_L) the solidification of the samples began. At T_L, the two experiments show noticeable differences in the line profiles (Figure 42 middle). Both line profiles shows the formation of α-Mg from the liquid but the sample solidified at a cooling rate of CR of 20 K/min has a a small peak at 26 nm^{-1}. Peaks of an unexpected phase (YX) appear together with the peaks of the α-Mg. However, this peak overlap with one of the strong peaks of R_5Mg_{24} phase, but the other peaks of that phase were not observed close to this temperature. With the reduction in temperature, only the Mg peaks become more pronounced with both CR, but the peak of the YX phase remained unchanged.

The last part of the solidification is the formation of one more intermetallic phase at T_2. The new peaks can be indexed according the structure of R_5Mg_{24}. At this temperature the system is fully solidified and there is no further phase transformation observed in the alloys. Some of the peaks R_5Mg_{24} phase is same as the unknown phase that appeared at the start of in the sample cooled at 20 K/min.

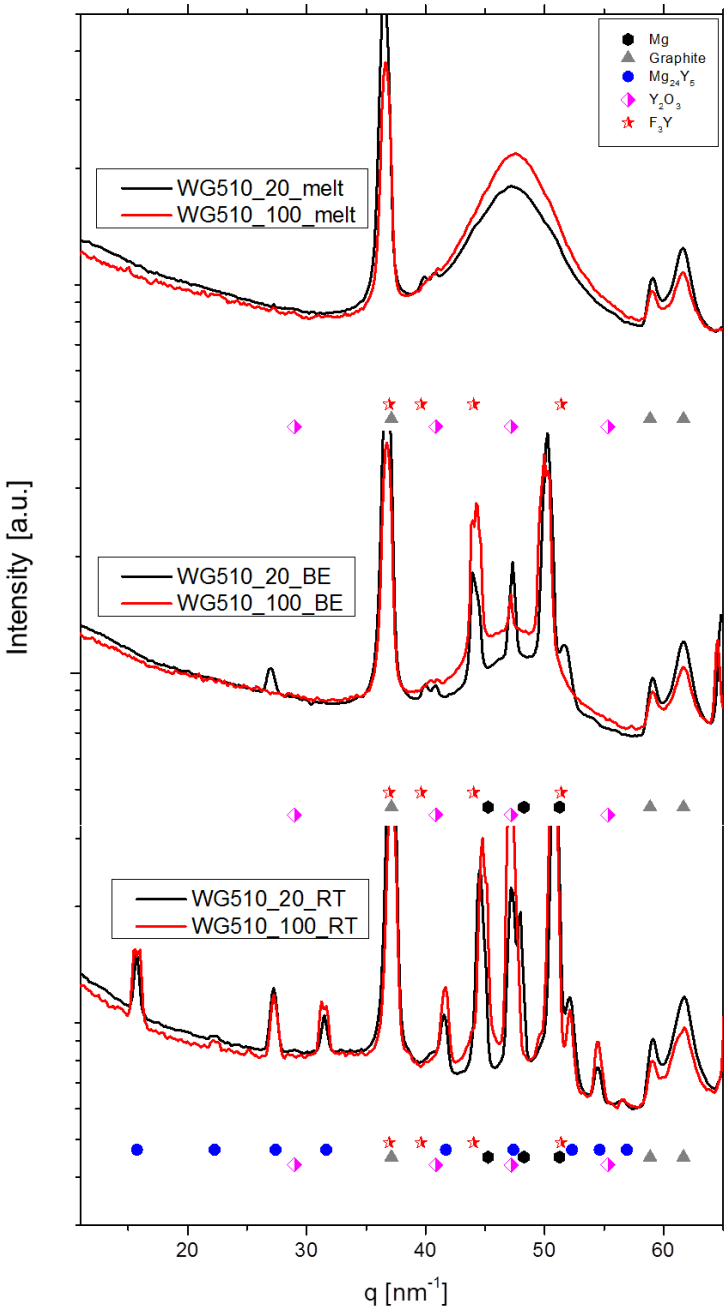

Figure 42. The results of the in situ solidification experiments of WG510. Red lines correspond to the experiment conducted with 100 K/min CR and the black lines belong to the 20 K/min CR. Upside of the figure the molten state of the two experiments. In the middle part of the figure the partly solidified (liquid and α-Mg) state before the eutectic temperature. And the bottom of the figure represents the fully solidified state. Symbols are used to index the major visible peaks of the observed phases.

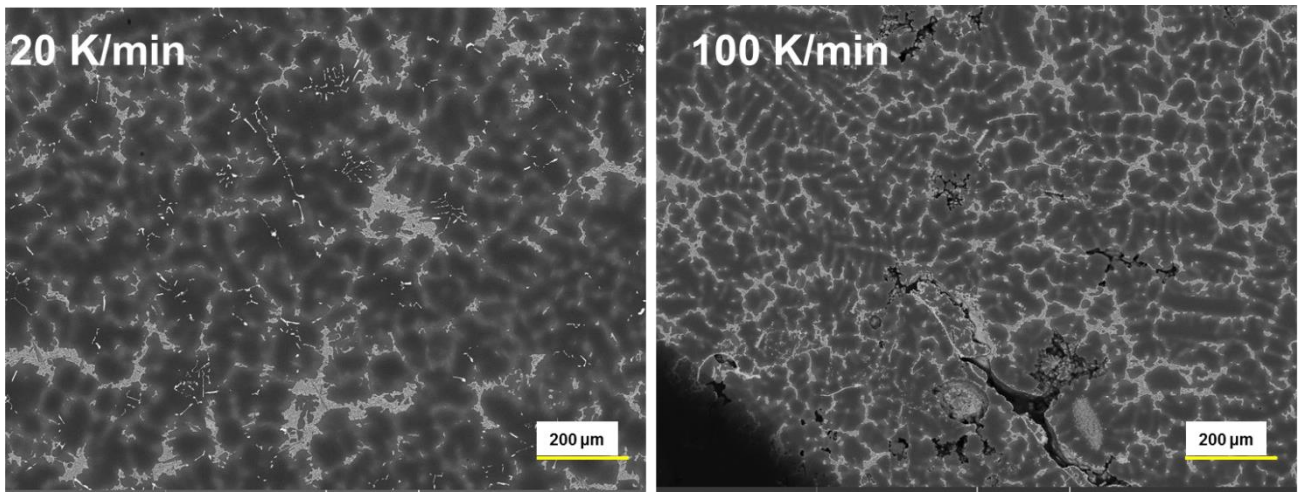

Figure 43. The resulted micrographs of the WG510 alloy with both CRs. The left side is with 20K/min. while the right side is with 100 K/min. cooling rate. The evaluated area fractions of IMPs are presented in Table 5-18. The darker areas (pores) were extracted from the total area.

The microstructures of the as-solidified samples show significant differences due to the presence the unknown phase. The SEM micrographs are shown in Figure 43 and the area fractions of the intermetallic particle are presented in Table 5-15. The EDX analysis revealed that some of the RERPs are containing aluminium in the sample examined 20 K/min. Therefore the area fraction of the RERPs are significantly higher in this sample.

Table 5-18. The results of the area fractions of the intermetallic particles (IMP) and RERPs in the WG510 alloy with the two examined cooling rates (20 and 100 K/min). The intermetallic phase which formation was observed together with α-Mg in the sample with 20 K/min is considered as an RERP in the evaluation of area fraction.

Alloy	Cooling rate	Area fraction of IMP [%]	Area fraction of RERPs [%]
WG510	**20**	*4.94±0.23*	*0.94±0.01*
	100	*10.78±0.09*	*0.24±0.01*

In the case of the WG510 alloy the two experiments with different cooling rates show differences in the solidification path. This difference is observed in the resultant microstructure, therefore EDX investigations for both cooling rates are presented to show these inherent differences, in Figure 44 and Figure 45 at CR 100- and 20 K/min respectively.

SEM-EDX point analyses was carried out on selected areas of the microstructure two microstructures and the quantified results are presented in Table 5-19 (100 K/min) and Table 5-20 (20 K/min).

The microstructure of the 100K/min cooled sample has 3 distinct regions the matrix, eutectic structures and the RE rich particles. The EDX analysis point 1 is from a region far from both eutectic structures and the RE rich particles and represents the matrix composition. . The matrix consist of magnesium and the mixture of both Y and Gd in an atomic (weight) ratio of ~1:1 (~4:7) (Y:Gd). The matrix itself has a composition of 87.6 wt.% (95.2 at.%) Mg, which is close to the average value of ~88 wt. % (~96 at.%).

with the EDX point 2 represent a profile that is typical of one recorded from the eutectic structure where no RE rich particles are observed. These particles consist of Mg and the mixture of both Y and Gd at a ratio of ~8:1 (Mg:RE). This is comparable to the concentration values observed in the other alloys. However, the eutectic structure with the R_5Mg_{24} contains a higher concentration of Gd than Y where the Y:Gd ratio in the eutectic structure is ~6:(at.%) ~1:2 (wt.%).

The last two EDX-spectra were recorded from RE rich particles near the edge of the eutectic regions. These points have high RE concentration and in point 4 the concentration of RE is higher than Mg. The oxygen and fluorine concentrations is also detected at these points, but much lower than in the case of other alloys. The point five is from a larger area, where a collection of small RE rich particles are present and here a higher concentration of oxygen is measured.

Table 5-19. The SEM-EDX point analysis of the typical observed microstructural features in WG510 alloy with 100 K/min CR (Figure 44). The results are presented both at.-and wt. %.

Point	**Concentration at. %**				
	Mg	**Y**	**Gd**	**F**	**O**
X_1	*95.2*	*1.2*	*1.2*	-	*2.4*
X_2	*89.8*	*4.6*	*5.4*	-	*0.2*
X_3	*85.1*	*8.6*	*5.2*	*0.5*	*0.6*
X_4	*24.9*	*20.7*	*13.3*	*0.5*	*0.3*
X_5	*65.4*	*16*	*8.7*	-	*9.8*
Point	**Concentration wt. %**				
	Mg	**Y**	**Gd**	**F**	**O**
X_1	*87.6*	*4.1*	*7.1*	-	*1.5*
X_2	*63.4*	*11.8*	*24.5*	-	*0.1*
X_3	*56.3*	*20.8*	*22.4*	*0.2*	*0.3*
X_4	*10.6*	*32.3*	*36.9*	*0.2*	*0.1*
X_5	*35.1*	*31.3*	*30.2*	-	*3.5*

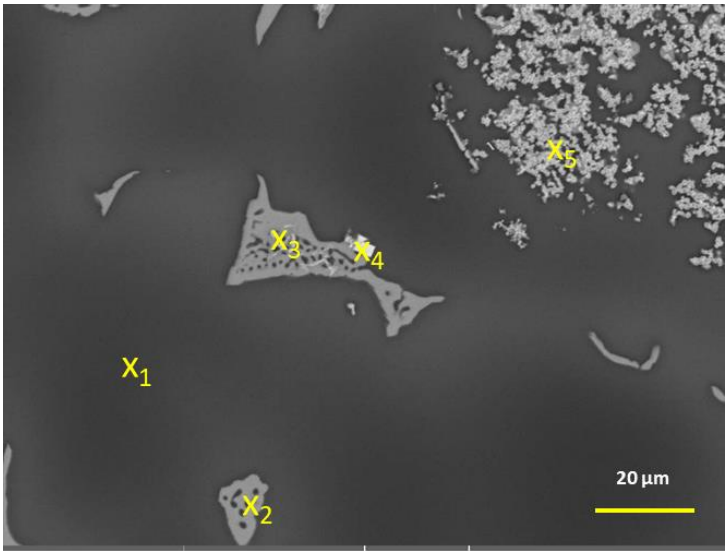

Figure 44. A higher magnification micrograph of the WG510 alloy cooled with 100 K/min. The EDX point analyses of the particles are shown in Table 5-19. The middle of the X shows the centre of the applied e-beam.

The final microstructure of the WG510 alloy with 20 K/min CR is shown in Figure 45. There were 3 major areas which were analysed being, matrix, eutectic region and the unknown phase. The EDX analysis point one is a new feature of the microstructure that was not observed in the other alloys nor in the other samples of the same alloy. This phase contains a high concentration of aluminium and RE elements with a moderate concentration of Mg. The atomic ratio is Al:RE ~2:1. These particles from away from the eutectic structures and is surrounded by α-Mg. The atomic (weight) ratio of Y:Gd in this particles is ~1:1 (~1:2).The 3rd point where EDX analysis was conducted, is on the matrix far from eutectic structures or other phases. . This point consist of Mg and the mixture of both alloying RE elements in atomic (weight) ratio of 10:9 (~5:8) (Y:Gd). The matrix contained ~89 wt. % (96 at. %) f Mg and around ~10 wt. % of RE.

On the EDX analysis from the eutectic structure consist of Mg and a mixture of RE, with a ratio of ~8:1 (Mg:RE). The atomic (weight) ratio of Y:Gd in the eutectic structure is: ~2:3 (~3:8).

Table 5-20 The SEM-EDX point analysis of the typical observed microstructural features in WG510 alloy (Figure 45). The results are presented both atomic and weight percent.

Point	**Concentration at. %**				
	Mg	**Y**	**Gd**	**Al**	**O**
X_1	*18.5*	*14.9*	*15.1*	*50.9*	*0.6*
X_2	*89.9*	*3.9*	*5.8*	*0.1*	*0.3*
X_3	*95.6*	*1*	*0.9*	*0.1*	*2.4*
Point	**Concentration wt. %**				
	Mg	**Y**	**Gd**	**Al**	**O**
X_1	*8.1*	*24.8*	*42.9*	*24.8*	*0.2*
X_2	*63.3*	*10.1*	*26.4*	*0.1*	*0.1*
X_3	*89.5*	*3.3*	*5.7*	*0.1*	*1.5*

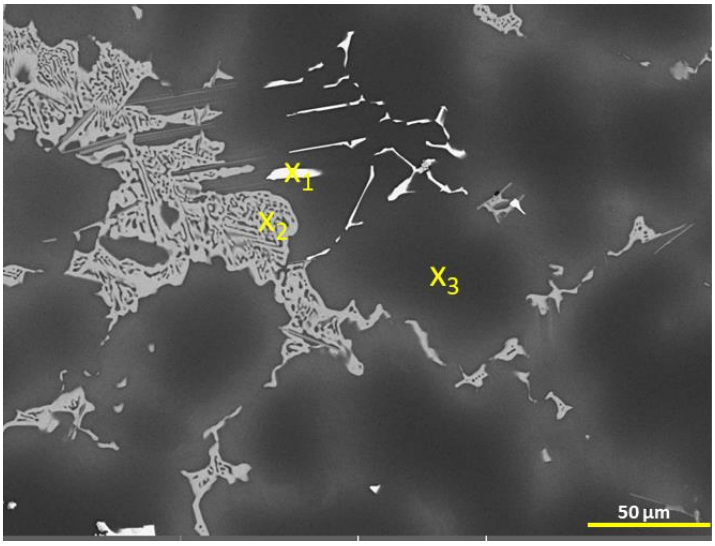

Figure 45. A higher magnification micrograph of the WG510 alloy cooled with 20 K/min. The EDX point analyses of the particles are shown in Table 5-20. The middle of the X shows the centre of the applied e-beam.

The process of solidification is different in WG510 due to possible Al contamination of the sample used for the 20 K/min CR and no repeated experimentation possible to check the accuracy of the data.

The time-2Θ diagram with the time-Temperature program is presented with the 100 K/min CR in Figure 46. Although, the alloy composition is different from the WG105 alloy 100 K/min CR show the same changes observed in W105 alloy. The initial (as-cast) and the as-solidified (final) microstructures both contained the same phases albeit, the composition of these phases are different in terms of ratio between Gd and Y.

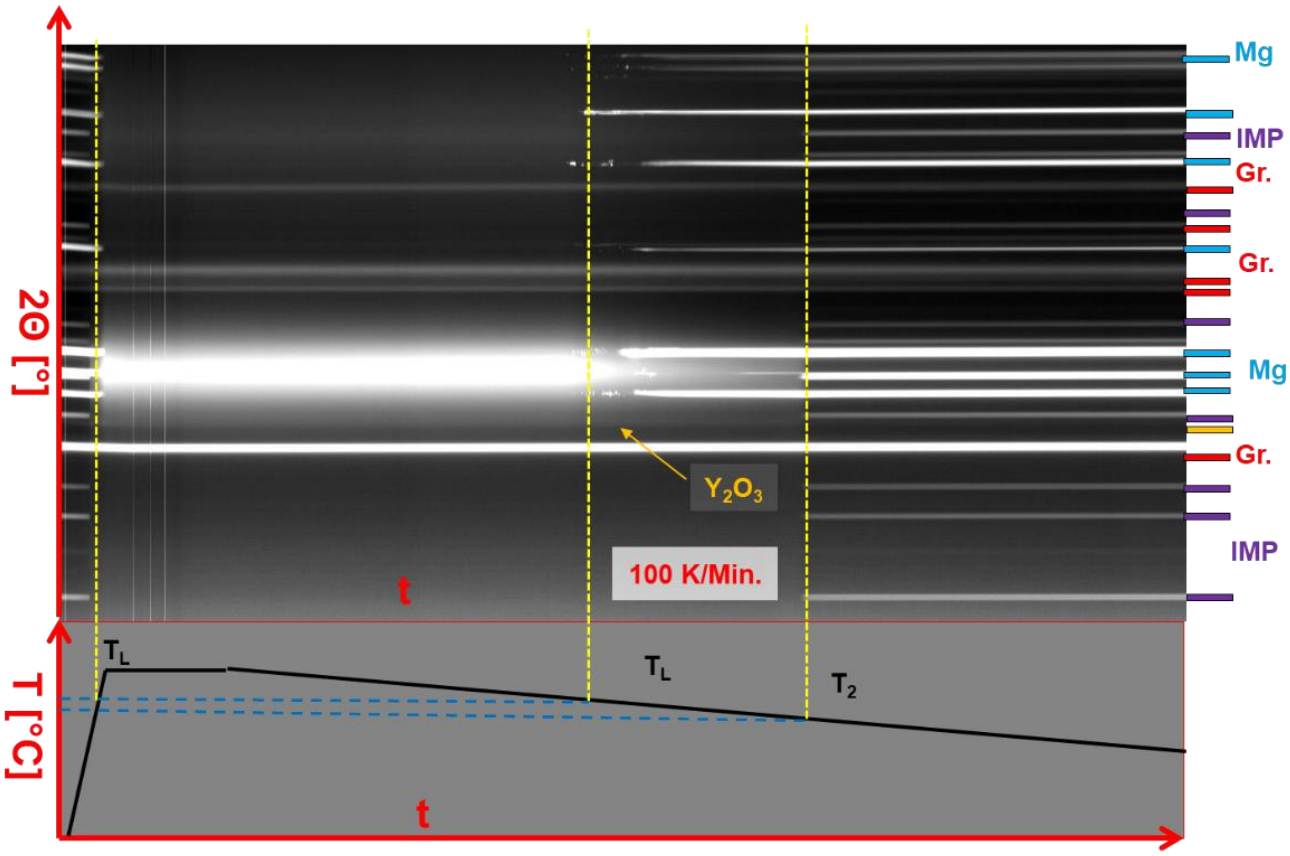

Figure 46. The overview of the SRXRD solidification experiment of the WG510 with the cooling rate of 100K/min, and the time-Temperature program of the experiment. During the heat up (left part of the picture) the peaks/lines of the sample (α-Mg: light blue, secondary phase: purple) disappear after overcoming the T_L, and start appearing just after cooling back to T_L (this temperature only α-Mg). In between peaks from the crucible (red: Gr.) and probably Y_2O_3 peaks (yellow arrows) are visible. The peaks of the secondary phase are observed after reaching the T_2 and the background radiation also drops at this temperature, indicates that the sample fully solidified.

5.5.2 The analysis of the peaks of the R_5Mg_{24}

All of the ternary alloys followed a similar solidification path to that of binary W15 alloy. The solidifications started with the formation of α-Mg and at the eutectic temperature of the alloys an intermetallic phases with structure R_5Mg_{24} was observed. No other intermetallic phases was detected (except in the case of WG510 with 20 K/min. due to the Al contamination). Although the experimental set up is not adjusted for a possible peak fitting analysis, SEM-EDX results demonstrate significant differences in chemical composition in the same intermetallic phase showing large solubility of Gd in place of Y in the R_5Mg_{24} phase.

As it is described in section 2.3 peak profile analysis will show any crystallographic change in the same phase due to variations in chemical composition. Therefore, the two most intense peaks of the R_5Mg_{24} phase (<220> and <211>) are compared among the ternary alloys and W15 at CR of 100 K/min. With the higher cooling rate of 100 K/min CR, the peaks cannot be fitted for an accurate analysis to provide quantitative data thus 20 K/min samples were not used for this approach. The peaks were fit with a simple Gaussian fitting to estimate the peak position (to observe a possible peak shift) and the full width half maximum values (FWHM). The peaks with the fittings are presented in Figure 47 and Figure 48 with the results from these fits are shown in the Table 5-21. Both peaks show no detectable change in peak position compared with Y_5Mg_{24} peaks in the W15. The FWHM values show some peak broadening mainly in peak <211>. In this case, the fitted peak the FWHM values are at least 20% higher than the FWHM value for W15. This indicates a detectable peak broadening of the intermetallic phase, but no quantitative information can be drawn from these results.

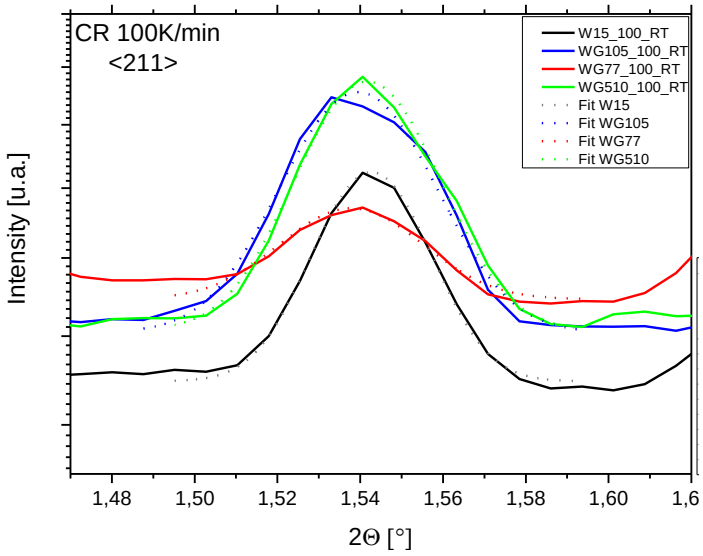

Figure 47. SRXRD diffraction <211> peaks of the R_5Mg_{24} intermetallic phase with the Gaussian fitting in the examined alloys W15 (black), WG105 (blue), WG77 (red) and WG510 (green) with a CR of 100 K/min.

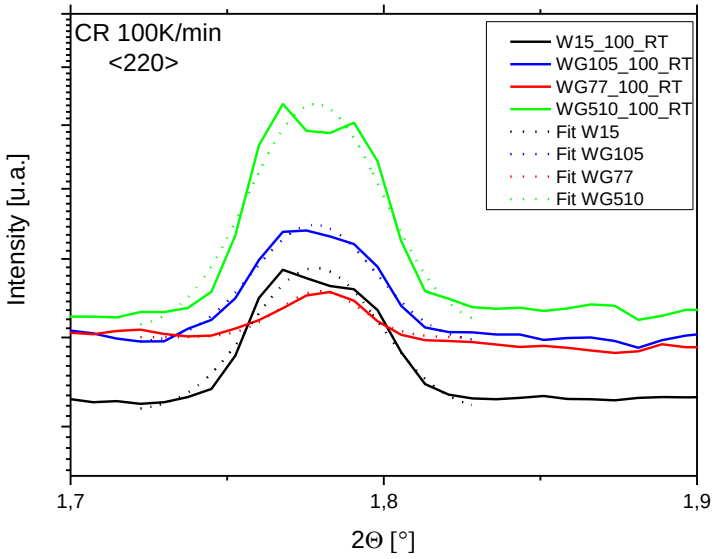

Figure 48. SRXRD diffraction <220> peaks of the R_5Mg_{24} intermetallic phase with the Gaussian fitting in the examined alloys W15 (black), WG105 (blue), WG77 (red) and WG510 (green) with a CR of 100 K/min.

Table 5-21. The table presents the values of the fitted peaks. The exact peak position and the value of the full width at half maximum of the peaks.

Peak	**211**		**220**	
Alloy	**Peak position [°]**	**FWHM**	**Peak position [°]**	**FWHM**
W15	*1.5426*	*0.03205*	*1.7781*	*0.0466*
WG105	*1.5395*	*0.04139*	*1.7774*	*0.0441*
WG77	*1.5378*	*0.03955*	*1.7796*	*0.0303*
WG510	*1.5417*	*0.03848*	*1.7782*	*0.0469*

Table 5-22. The SEM-EDX point analysis of the area of the eutectic structure in all the yttrium containing alloys with 100 K/min CR. The results are presented both at.-and wt. %.

Alloy	**Concentration [at. %]**			
	Mg	**Y**	**Gd**	**O**
W15	*87.3*	*9.3*	-	*2*
WG105	*82.5*	*10*	*4.1*	*3.4*
WG77	*89.5*	*10.4*	*0.2*	-
WG510	*89.8*	*4.6*	*5.4*	*0.2*
Alloy	**Concentration wt. [%]**			
	Mg	**Y**	**Gd**	**O**
W15	*70.1*	*27.2*	-	*1.1*
WG105	*55.8*	*24.7*	*17.9*	*1.5*
WG77	*69.9*	*29.7*	*1.1*	-
WG510	*63.4*	*11.8*	*24.5*	*0.1*

5.5.3 Phase transformation temperatures measured with DSC

Differential scanning calorimetry (DSC) measurements were performed on all alloys to determine the phase formation and transformation temperatures during the solidification. The DSC results are compared with the results from the SRXRD studies the 20 K/min as the maximum cooling rate of the DSC is not able to achieve 100K/min CR. The results of the measurements are presented in Figure 49. All solidification thermal profiles show two peaks during the solidification. The first peak is the formation of the α-Mg and the second peak is the eutectic temperature of the alloys.

The peaks determined the solidification range of the alloys (ΔT) and the transformation temperatures and the calculated ΔTs are presented in Table 5-23.

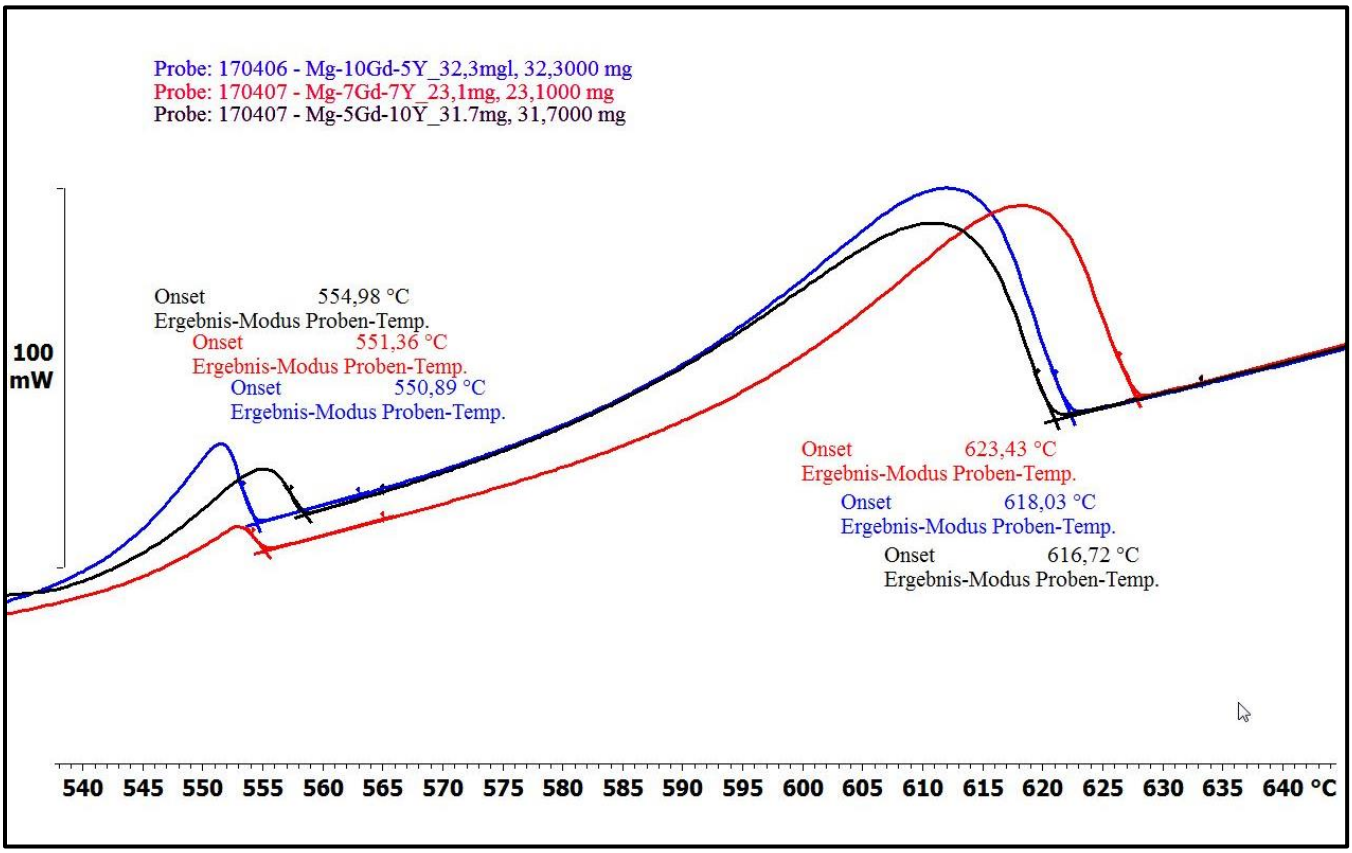

Figure 49. The DSC curves (temperature-heat flow) of the WG105 (black), WG77 (red) and WG510 (blue) alloys during solidification with 20 K/min cooling rate. Two exothermic reaction were recorded during the cooling of all samples. The first reaction is the crystallisation of α-Mg from the melt at T_L: 618.1°C in WG510, 623.4°C in WG77 and 616.7 °C in WG105. The second reaction is the formation of the secondary phase together with the continuous formation of α-Mg at T_2: 550.9 °C in WG510, 551.4°C in WG77 and 555°C in W15.

5.5.4 Summary of the thermal analysis of the ternary alloys

Two different type of solidification experiments were carried with SRXRD experiments at two CRs (20 and 100 K/min) and DSC experiments at one CR (20 K/min). During the solidification experiment the phase formation/transformation temperatures were experimentally determined and solidification ranges (ΔT) were calculated. The results from both types of experiments are summarised in Table 5-23. Since the results of the SRXRD and microstructure analysis indicate

that all the ternary alloys have a similar solidification path, which is comparable to the solidification path of the binary W15 alloy, the table also includes results from the binary W15 alloy.

Table 5-23. The table presents experimentally determined temperatures of phase formations in the examined ternary alloys and the binary W15 alloy.

Alloy	**DSC (20 K/min) [°C]**			**SRXRD [°C]**					
				20 K/min			**100 K/min**		
	T_L	**T_2**	**ΔT**	**T_L**	**T_2**	**ΔT**	**T_L**	**T_2**	**ΔT**
W15	612.5	561.7	50.8	605.2	553.8	51.4	617.3	564.2	53.1
WG105	616.72	554.98	61.74	622.7	561.3	61.4	611.4	550.1	61.3
WG77	623.43	551.36	72.07	618.7	549.3	69.4	614.1	547.9	66.2
WG510	618.03	550.89	67.14	605.2*	543.7	61.5	611.3	546.2	65.1

*In this certain experiment $REAl_2$ phase formation is detectable together with α-Mg.

Table 5-24 The Area fraction of the intermetallic particles in the as-solidified samples including the binary W15 and G15.

Alloy	**Cooling rate**	**Area fraction of IMP [%]**	**Area fraction of RERPs [%]**
W15	**20**	*4.66±0.06*	*0.18±0.01*
	100	*10.75±0.12*	*0.29±0.02*
WG105	**20**	*7.54±0.06*	*0.36±0.06*
	100	*11.42±0.16*	*0.76±0.01*
WG77	**20**	*4.32±0.16*	*0.42±0.01*
	100	*9.51±0.13*	*1.78±0.02*
WG510	**20**	*4.94±0.23*	*0.94±0.01*
	100	*10.78±0.09*	*0.24±0.01*
G15	**20**	*4,89±0,04*	*0,11±0,01*
	100	*10,18±0,14*	*0,08±0,01*

5.5.5 Results of calculations of the ternary alloys

The solidification path of each alloy was simulated with Pandat thermodynamic software using PanMg 2017 database using both equilibrium (Lever rule) and non-equilibrium (Scheil) calculations. The Mg rich side of the ternary phase diagram was calculated and the solidification paths of the ternary alloys according to the Scheil model (Figure 50a) and Lever rule (Figure 50b) were overlaid to show the solidification path.

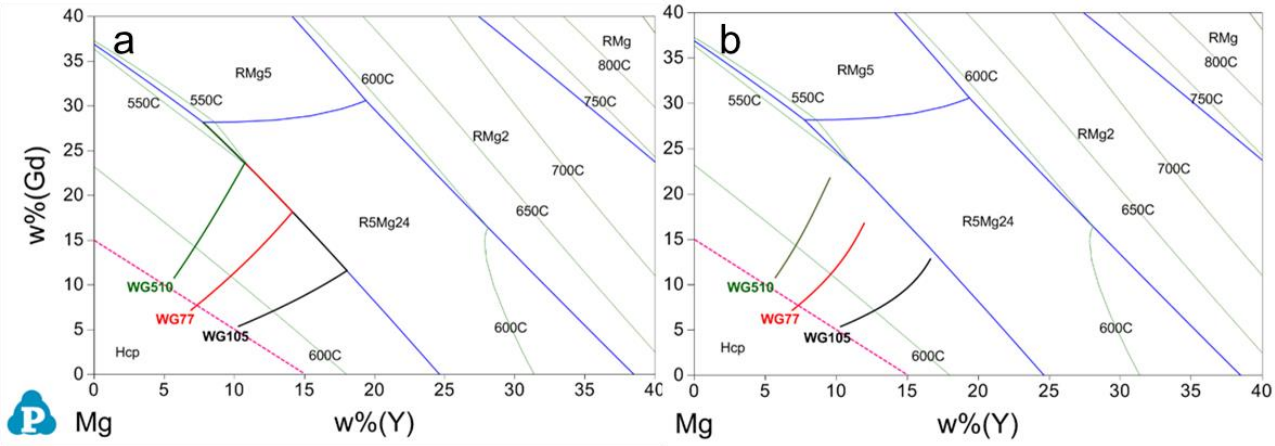

Figure 50. Magnesium rich part of the calculated liquidus projection of the Mg-Y-Gd phase diagram. Superimposed are the calculated solidification paths of the three ternary alloys WG510 (green), WG77 (red) and WG105 (black) under two different conditions: (a) Scheil model, and (b) Lever rule. The starting point of the paths correspond to the actual alloy compositions whereas the cross-section line of the nominal compositions is indicated by the magenta dash line along (wt% Y + wt% Gd = 15).

According to the Lever rule the only difference between the solidifications of these alloys are the Liquidus (T_L) and the finishing temperatures (T_2). Due to the high diffusion rate, none of the alloys should contain any intermetallic phase that form during solidification. The three alloys forms along the cross-section of the phase diagram (magenta dash line), which is presented in Figure 50. The determined T_L and solidus temperatures (T_2) with liquidus-solidus (T_L-T_2=ΔT_1) ranges and solidification ranges (T_L-T_E=ΔT_2) calculated using the Lever and Scheil approaches are presented in Table 5-26. The solidification paths with both approaches for each alloys are plotted on Figure

52-53. These curves clearly show the formation of 3 different phases following the Scheil calculations but only the formation of Mg from liquid is observed in the case of Lever rule.

The solidification paths of the alloys following the Scheil are WG510 (green-), WG77 (red-) and WG105 (black). The calculations predicts a similar solidification path for all three ternary alloys. The solidifications start with the formation of primary α-Mg phase at T_L are: 615, 620 and 613°C in the WG510, WG77 and WG105 respectively. With the progression of the solidification the liquid phases enrich in RE elements till the concentration of the liquid meet with the quasi-eutectic line (ie a line where an intermetallic phase forms but not the eutectic point on the ternary phase diagram). At this point (T_2) intermetallic phases (R_5Mg_{24}) forms (alongside with Mg) from the liquid phase at calculated temperatures of 549, 555 and 562°C in WG510, WG77 and WG105 respectively. This calculated temperature with the liquidus temperatures determine the ΔT_1 range in the alloys. In all three cases the solidification progress further till the rest of the liquid phase reach the ternary eutectic concentration and temperature. At this temperature (545°C) the rest of the liquid transforms into three different phases: primary α-Mg, the R_5Mg_{24} and the RMg_5 phases. The difference between the T_E and T_L determine the solidification range (ΔT_2) of the alloys. The final volume fractions each of the 3 phases expected from the thermodynamic calculations for all three alloys are presented in Table 5-25 and summarised in Figure 55. Both these show the formation of RMg_5 phase with all three alloys and that the phase transformation is completed at the eutectic point of the ternary alloy rather than with the formation of Mg and R_5Mg_{24} phase.

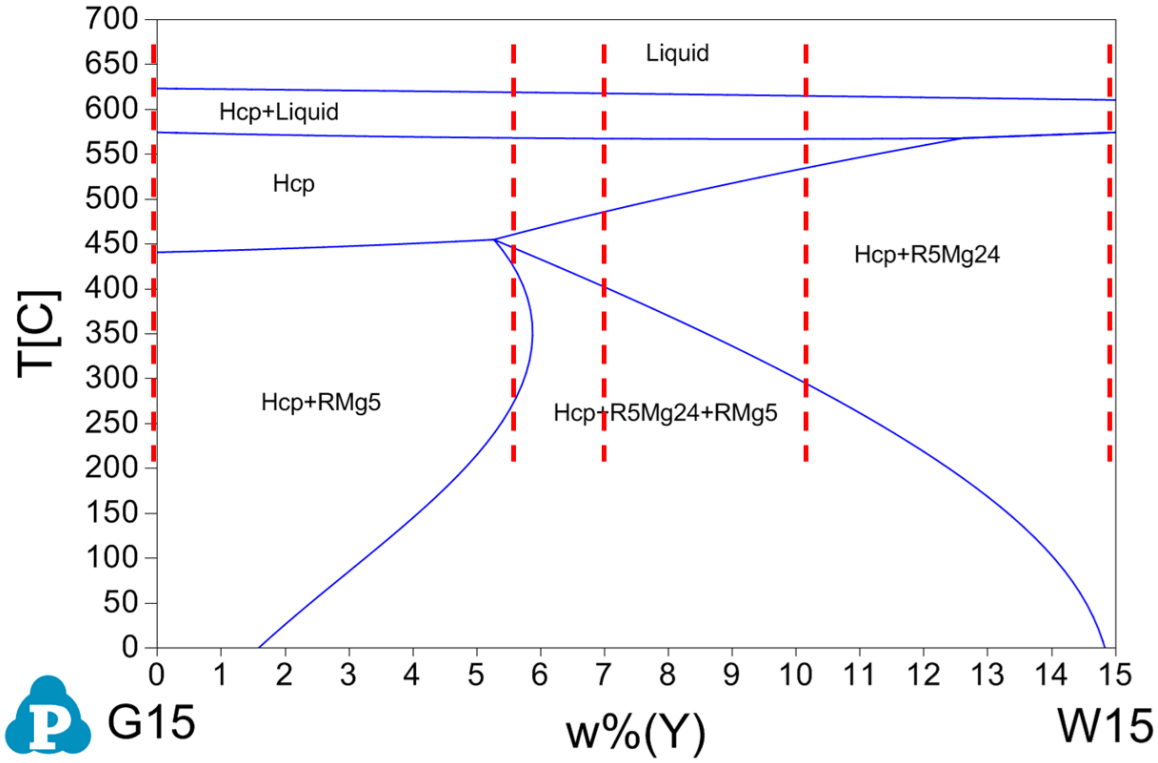

Figure 51. A cross-section of the magnesium rich part of the equilibrium ternary phase diagram of the magnesium-yttrium-gadolinium system, calculated by Pandat. The phase diagram includes the determined solidification "paths" of the examined alloys according to equilibrium.

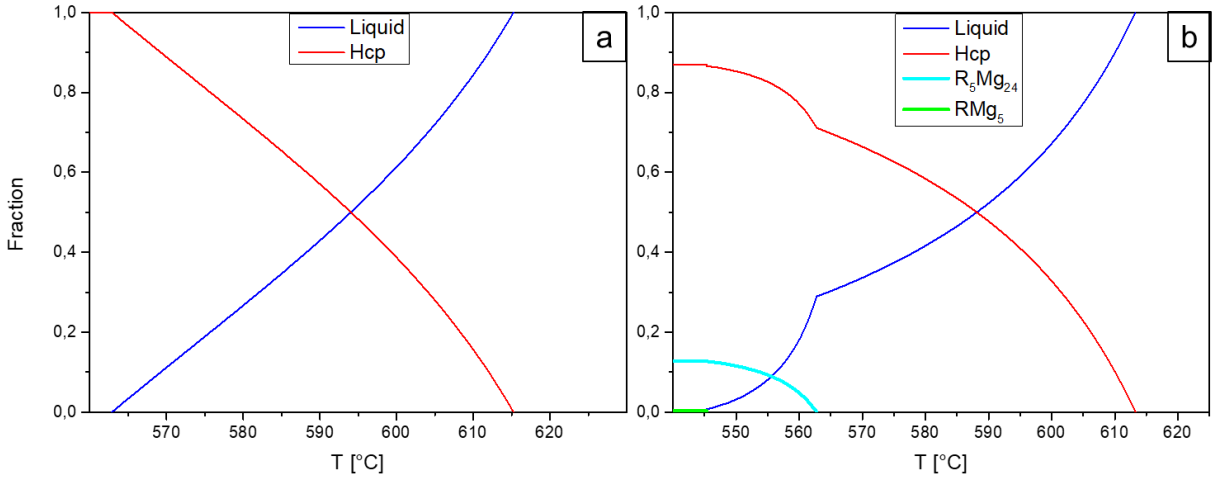

Figure 52. The figure presents the changes of the mole fractions during the solidification of WG105 (black line in Figure 50) according to the calculations of Lever (a) and Scheil (b). Lever rule do not expect any intermetallic phase formation, while Scheil expects 12.69 % R_5Mg_{24} and 0.27% RMg_5. The results of the calculations are presented in Table 5-25 and Table 5-26.

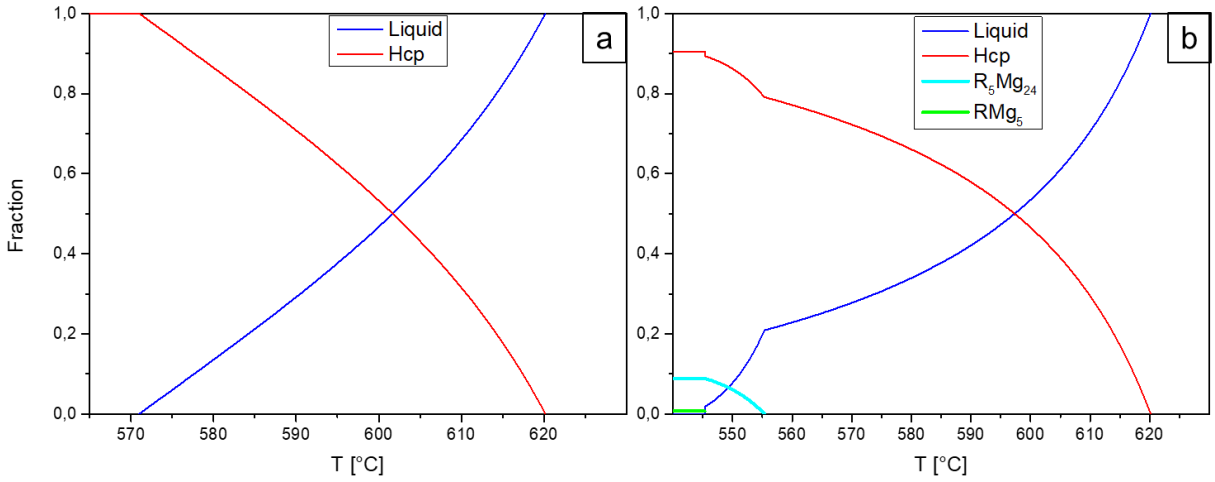

Figure 53. The figure presents the changes of the mole fractions during the solidification of WG77 (red line in Figure 50) according to the calculations of Lever (a) and Scheil (b). Lever rule do not expect any intermetallic phase formation, while Scheil expects 8.82 % mole fraction of secondary R_5Mg_{24} and 0.67% mole fraction of terniery RMg_5 phases. The results of the calculations are presented in Table 5-25 and Table 5-26.

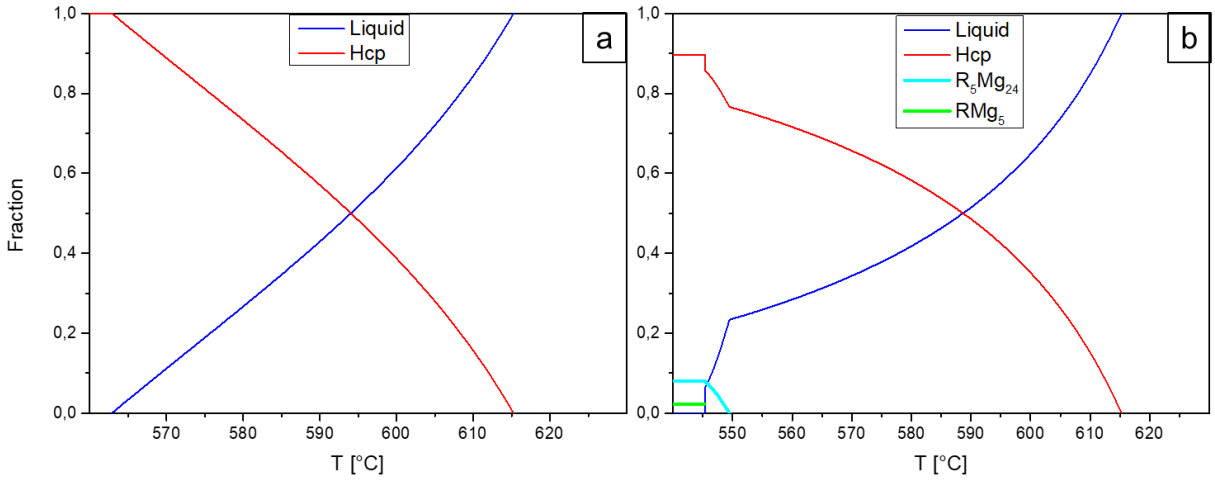

Figure 54. The figure presents the changes of the mole fractions during the solidification of WG510 (green line in Figure 50) according to the calculations of Lever (a) and Scheil (b). Lever rule do not expect any intermetallic phase formation, while Scheil expects 7.98 % mole fraction of secondary R_5Mg_{24} and 2.3% mole fraction of ternary RMg_5 phases. The results of the calculations are presented in Table 5-25 and Table 5-26.

Table 5-25. The table presents the calculated mole/mole fractions of solid phases at the end of the solidification in the ternary alloys.

Alloy	**State**	**mole fraction α-Mg [%]**	**mole fraction IMP [%]**	
			$R_{24}Mg_5$	**R_5Mg**
WG105	Scheil	*87.04*	*12.69*	*0.27*
	Lever	*100*	*0*	*0*
WG77	Scheil	*90.51*	*8.82*	*0.67*
	Lever	*100*	*0*	*0*
WG510	Scheil	*89.73*	*7.98*	*2.29*
	Lever	*100*	*0*	*0*

Table 5-26. The table presents the calculated forming temperatures of the solid phases during the solidification of the ternary alloys and their determined temperature ranges between transformations. The T_L-T_2=ΔT_1 and their full solidification ranges T_L-T_E=ΔT_2.

Alloy	**Model**	**Expected phases**			**Expected T [°C]**			**ΔT_1 [°C]**	**ΔT_2 [°C]**
		1st	2nd	3rd	T_L	T_2	T_E		
WG105	Scheil	α-Mg	R_5Mg_{24}	RMg_5	*613*	*562*	*545*	*51*	*68*
	Lever	α-Mg	-	-	*613*	*564**	-	*49*	-
WG77	Scheil	α-Mg	R_5Mg_{24}	RMg_5	*620*	*555*	*545*	*65*	*75*
	Lever	α-Mg	-	-	*620*	*571**	-	*49*	-
WG510	Scheil	α-Mg	R_5Mg_{24}	RMg_5	*615*	*549*	*545*	*66*	*70*
	Lever	α-Mg	-	-	*615*	*562**	-	*53*	-

* No formation of any secondary phase but the solidification finishes at this temperature.

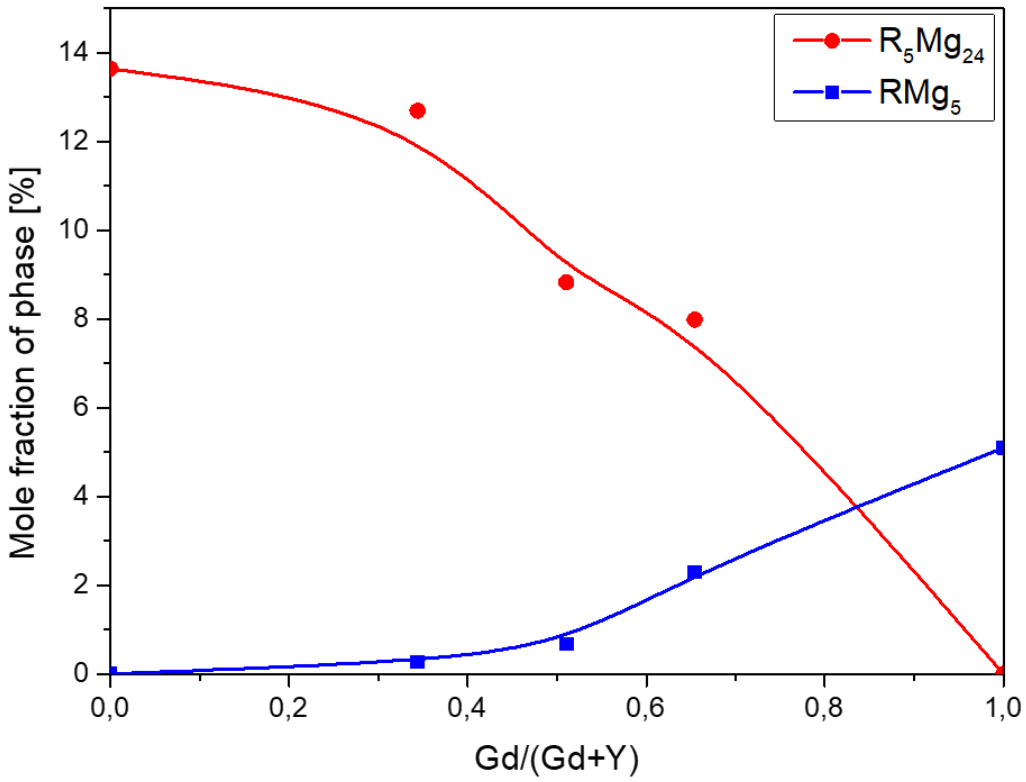

Figure 55. The predicted mole fractions of the intermetallic phases in the investigated alloys. Results were determined using Pandat 2017 using PanMg2017 database.

.

5.6 Microstructure investigation on quenched G15

The in situ SRXRD solidification studies of the binary Mg-Gd alloy (G15) show a solid state intermetallic phase transformation during microstructure evolution. Therefore, this alloy samples were prepared by quenching near the transformation temperatures in order to keep some residual volume fraction of the first intermetallic phase that formed at the higher temperature.

The resultant microstructure has more than one Gd rich phase, but the volume fraction of the metastable phase is very small compared with the stable ß ($GdMg_5$), that a TEM investigation of the area of interest was prepared with Focused ion beam (FIB) milling and lift out using a FEI Helios Nanolab. The preparation is described in more detailed in Chapter 4.3. Figure 56 shows the two steps of the FIB preparation of the TEM specimen. On the left side it is shows how the

interested area was prepared and cut out from the bulk material, and the right side shows the already cut, sample on the Cu sample holder ready for examination in TEM.

Figure 57 presents a TEM-bright field image showing α-Mg and two intermetallic phases identified. These three features of the sample were further analysed using electron diffraction using micro beam electron diffraction techniques and TEM-EDX analysis. The EDX spectra recorded from this phase is presented in Figure 58 as the intermetallic phase type-1with a quantified composition of Mg 80.9±2.5 at. % and Gd 19.10±2.7 at. %. This composition is close to that of GdMg5. The diffraction patterns recorded from this phase, identified was as $GdMg_5$ and shown in the top row Figure 59, which corresponds to <110>, <111> and <112> zones of $GdMg_5$, respectively. The diffraction patterns recorded from the metastable phase Figure 59 (bottom row) correspond to <111> and <343> zones, while the quantified TEM-EDX spectra in Figure 58 (Type-2, blue line) shows a composition of Mg 70±5 at. % and Gd 30 ±5 at. %, which provides a Mg:Gd ratio of ~2.5, thus this phase could be the $GdMg_3$. Cu and Ga peaks observed in the EDX spectra are artefacts due to the Cu grid and the Ga remaining from milling process. The matrix composition is shown alongside in Figure 59 for comparison purposes.

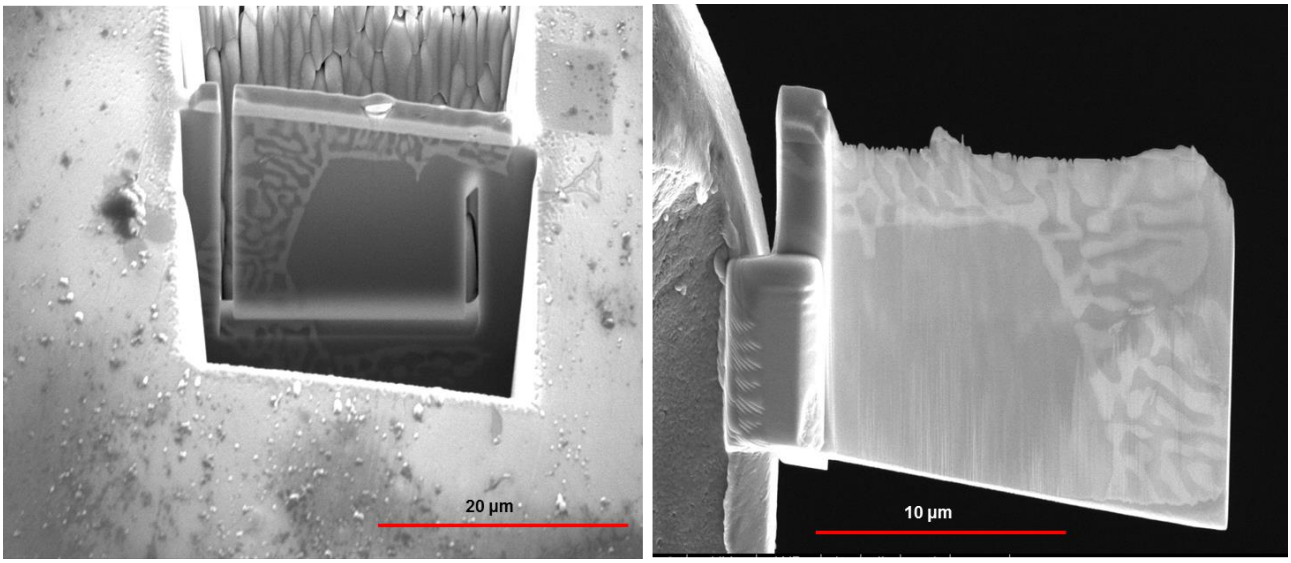

Figure 56. Left side shows how the interested area was prepared and cut out from the bulk material, and the right side shows the already cut, welded and further mild sample on the Cu sample holder.

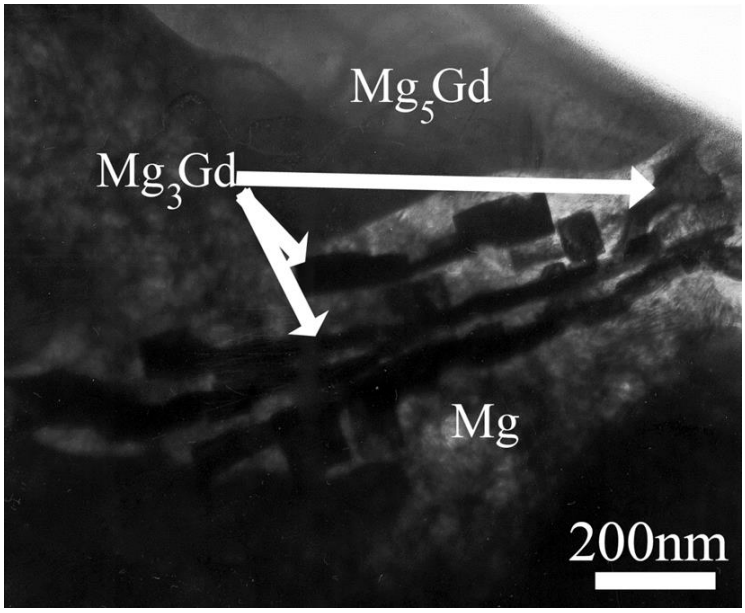

Figure 57. TEM-bright field image of the quench sample. Three Typical area can be observed on the micrograph. The α-Mg matrix and two intermetallic phase [139].

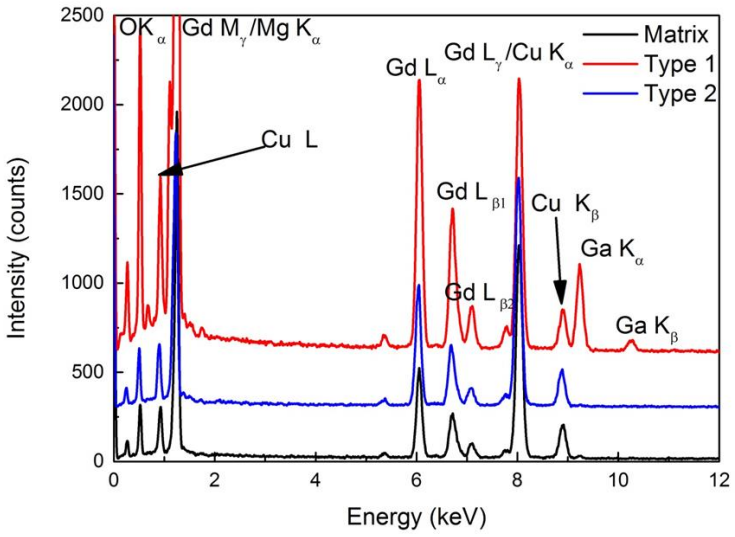

Figure 58. TEM-EDX spectra of the three-different phases, observed on the TEM-bright field image (Figure 57). Black line is the spectrum of the Mg matrix. The red line is a the spectra so called Type 1 which identified as an $GdMg_5$ while blue line is the spectra corresponds to $GdMg_3$ [139].

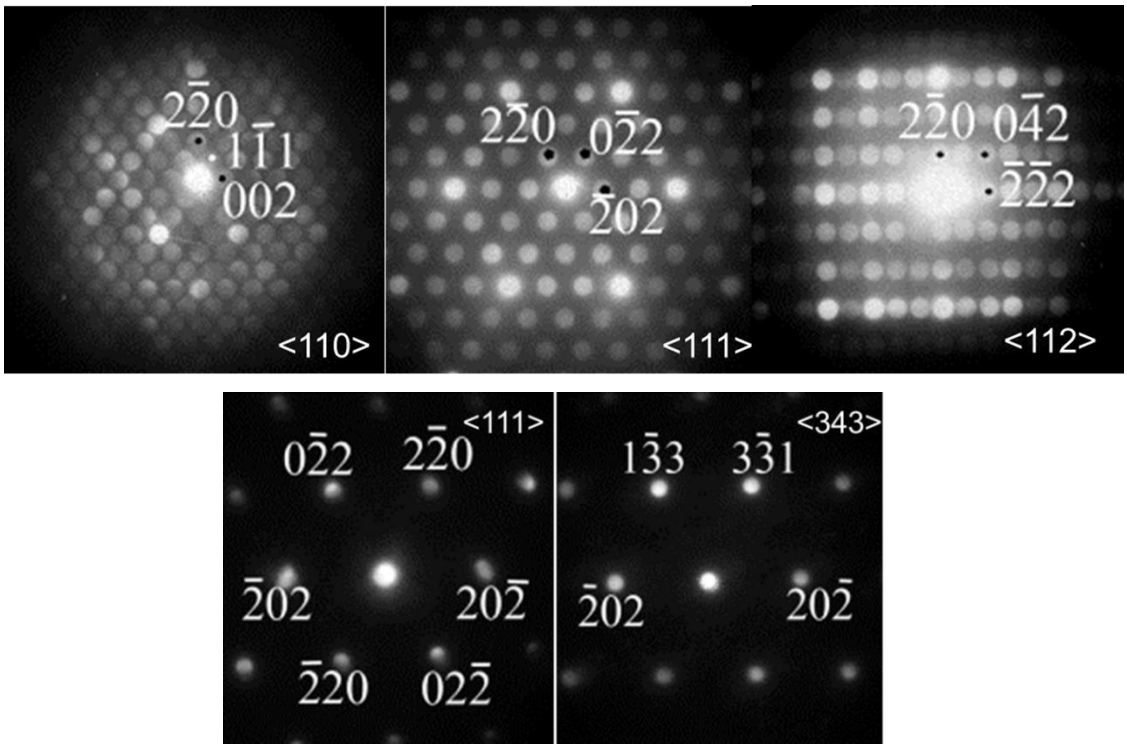

Figure 59. TEM-diffraction patterns recorded from phase Type 1 (red line in Figure 58) identified as $GdMg_5$ (upper row), TEM-diffraction patterns recorded from phase Type 2 (blue line in Figure 58) identified as $GdMg_3$ (lower row) [139].

6 Discussion

Two experimental techniques were utilized to follow the solidification sequences: DSC and SRXRD. DSC gives accurate temperature and heat value of a phase formation, while SRXRD can reveal the structural changes. The techniques can easily complement each other but both have limitations. One possible difficulty of the techniques is the detection limits. Former studies [132] of the same alloy system indicated that low concentration of the alloying elements (wt% (Gd+Y) < 8 %) made it difficult to detect the possible phase changes since the volume fraction of the secondary phases were around the detection limit. Therefore, the alloy selection went up to 15wt% alloying element. This higher amount of alloying element resulted sufficient enough to detect secondary phase formations during the solidification, but still remained far from the eutectic concentration.

The two selected cooling rates (CR) were: 20 and 100 K/min. The 20 K/min cooling rate can be considered as a sand cast material, while 100 K/min CR is around a preheated permanent mould castings. The DSC set up was suited to perform only the 20 K/min CR and was used to correlate with SRXRD measurement results. The experimentally examined results were compared with the thermodynamic assessment of the (in both equilibrium and non-equilibrium conditions) alloys determined by Pandat as well as with results of former studies.

6.1 General discussion about sample environment and set up adjustments

In situ SRXRD experiments during solidification have been already conducted for numerous different metallic materials to study their solidification behaviour especially the phase evolution during solidification [113, 128]. The general advantages and disadvantages are as follows:

Advantages:

- Good time temperature resolution

- Real time observed structural changes
- Possible to see multiply transformations simultaneously.

Disadvantages:

- Small volume fraction changes may not be detectable
- Higher energy X-ray source (can results peak overlapping)
- lower accuracy in the temperature control
- Limitation of sample rotation (evaluation only qualitative unless a fine scaled grains are expected with randomised orientations).

The disadvantages or difficulties of the technique has to be specified for this study. As described in Chapter 2.3, X-ray diffraction has been used for phase identification for over a hundred years. The detection limit depends on the volume fraction of the phases (a) and the interaction cross-sections (b) between the utilized X-ray and phase. Generally, it is stated that laboratory X-ray sources are able the detect phases above ~2% volume fraction. However, it is highly dependent on the observed phases. In this study, synchrotron radiation (because of the brilliance it provides; already several orders of magnitude better resolution compared with the laboratory scaled machines) with 100keV energy was utilized on magnesium alloys with Mg-RE intermetallic secondary phases. The applied energy has a much lower interaction cross-sections profile compared to that with the possible intermetallic phases (R_xMg_y) due to the differences of electron density (atomic number) between the elements {Magnesium (atomic number (Z): 12), Yttrium (Z: 39), Gadolinium (Z: 64)}. Thus, the detection limit is significantly improved.

The higher energy X-ray allows the samples to be examined on a transmission geometry, so the beam has to pass through the sample and sample environment. This has a great advantage on the sample environment, however it makes the resolution lower. The higher the energy of the monochromatic beam, the lowers the angle of diffracted beams. If the lattice parameters of phases that evolve during solidification are close to each other, it is hard to distinguish among them.

The temperature control is more limited compared to commercial DSC or DTA set-ups. The thermocouple is welded on the crucible that holds the sample. The heating of the used experimental system works with a conduction coil. Even if the connection between the crucible and the sample is perfect, a possible heat transfer shift of ±5°C error can be expected. This study used newly designed graphite crucibles. The thermocouple was welded on the Titanium lid of the crucible so higher possible temperature shift is expected. In some cases the temperature shifts are even higher than those expected. Additionally, detecting the start of the solidification has one more difficulty. As the first solidified nuclei (e.g. α-Mg) float in the melt without fixed orientation their detection is difficult, resulting in an uncertain temperature for the existence of the phase detected. Most likely the first phase can be detected at the first time as the system reaches the dendritic coherency point, the temperature where a continuous dendritic skeleton is built up. It can result a couple of °C delay in detection.

Unfortunately, the in situ set ups generally lack the possibility of sample rotation. Without rotating the samples, the diffraction patterns have weaker statistics and only peaks of orientations can be detected which are in a Laue position. This feature makes it impossible to make quantitative evaluation of the measurement and even qualitative evaluation needs to be backed up with complimentary techniques.

Instrumental absorption of diffraction peaks is also a limitation, which can be adjusted by wise design of the experimental set up. In case of the *in situ* solidification measurements the sample holder container (crucible) can be the major absorber of the diffracted peaks. The wall of the crucible has to be as less absorber as it is possible. Therefore, graphite (Z: 6) crucible, which has barely any interaction with the applied 100keV beam, were used instead of commercial steel (Z: 27) crucibles for DSC measurement. However, use of graphite crucibles accurate can result in less temperature control as compared to use of steel crucible.

The examined small samples of the SRXRD experiments typically are packed with great amount of porosity due to the re-melting. However, this do not have any influence to the solidification paths but generate incoherency in the resulted microstructure and appears either empty holes or

condensed areas of RERPs. During the evaluation of the microstructures the empty pores were not counted just extracted from the total areas.

6.2 Discussion of the binary alloys

The binary Magnesium-Yttrium and binary Magnesium-Gadolinium system have been studied by several researchers (Chapter 2.2). However, the solidification path had not been monitored by synchrotron radiation experiments before this study. Therefore, these experimental results (Chapter 5.3) are going to be correlated with thermodynamic calculations and existing literature data, using 20 and 100 K/min cooling rates.

6.2.1 W15 Alloy

Formation temperatures and respective phases

The experimentally measured liquidus temperature (T_L): 612.7°C by DSC (CR: 20K/min.), and 605.2°C and 617.3°C by SRXRD at 20- and 100 K/min CRs, respectively. On the XRD profiles the peaks are belongs to the Mg phase (Figure 17). The calculated result predicts 613.2°C as the start of the solidification, which is in a close agreement with the DSC measurement, but is shifted compared to the SRXRD results. The reasons for the possible errors are described in Chapter 6.1.

As soon as the temperature reaches the eutectic temperature (T_E) the rest of the liquid phase solidifies into a combination of an intermetallic phase and α-Mg. The peaks of the intermetallic phase on the SRXRD line profiles can be indexed with the diffraction peaks of R_5Mg_{24} type phase (Figure 17). The measured temperatures are: 562.6 °C by DSC, and 553.8 °C and 564.2 °C SRXRD 20- and 100 K/min. CRs, respectively. The calculations predict a higher temperature of 574.4°C for the end of the solidification. Although all results determined only two formation temperatures/phases during the solidification, the measured temperatures vary by a larger scale than expected. The measured and calculated temperatures are summarised in Table 6-1.

Table 6-1. The table presents calculated- and experimentally determined T_L and T_E temperatures and the resulted solidification range ($\Delta T=T_L-T_E$) of the W15 binary alloy.

W15 Alloy			
Method and CR [°C]	**Determined temperature [°C]**		**ΔT [°C]**
	T_L	**T_E**	
DSC 20	612.7	562.6	50.1
SRXRD 20	605.2	553.8	51.4
SRXRD 100	617.3	564.2	53.1
Scheil	613.2	574.4	38.8
Lever	613.2	574.4	38.8

The 2ϴ-time graph of the SRXRD experiments (Figure 20) indicates the end of the solidification upon reaching T_E. No more liquid phase is observed below that temperature. The temperature difference between the T_L and the T_E (where the intermetallic phase forms) results in the solidification range of the alloy (ΔT). Despite the fluctuations in the measured temperatures, the ΔT, calculated from the experimentally detected temperatures, are in good correlation to each other (~51°C), but due to the higher expected T_E, the calculation predicts a smaller solidification range of the alloy (~39°C). This observation points out a very important feature of the measurement set up of the SRXRD technique: the measured temperature shift (error) is greater than expected, but this change is consistent for all alloys investigated. Therefore, we can expect that the real temperature values are similar to those determined with DSC. So, the experimental results show a more accurate T_E (~563 °C) than the calculations (574.4°C). This expectation is not clarified with any of the experimental results in this study.

As a summary of this subsection a short list is given as the major conclusions:

- all results show two formation temperature (T_L, T_E),
- SRXRD clarify the order of the phase formations (first α-Mg then β (R_5Mg_{24})),
- only T_L of DSC matches with the predictions,
- greater than expected but consistent temperature shift with SRXRD (DSC clarify),
- wider ΔT than predicted, recorded experimentally.

Intermetallic phases fraction

Only the Y_5Mg_{24} secondary intermetallic phase (IMP) formation was observed both experimentally and predicted calculations and only the fraction of the IMP in the microstructure varies among the results. The area fraction of the IMP in the resultant microstructures are presented in Figure 18, while evaluated results values are presented in Table 5-5. The mole fraction of intermetallic phases was calculated both the Lever-rule and the Scheil-model (Table 5-9). Due to the significant mass difference between Mg and Y the mole fraction is better compares than mass fraction with the experimentally determined area fractions. The area fraction of the IMPs are 4.66 and 10.75 % with CRs of 20 and 100 K/min, respectively. The predicted mole fractions are: 1.05 and 13.52mole% with Lever-rule and Scheil model, respectively. The results are summarised in Table 6-2.

Table 6-2. The fraction of the secondary phase Y_5Mg_{24} in the microstructure of the W15 alloy, determined by experimentally (area fraction of SRXRD samples) and predicted by Pandat both Lever rule and Scheil model (mole fraction).

IMP fraction in W15 [%]		
State	**area**	**mole**
SRXRD20	4.7	-
SRXRD100	10.8	-
Lever	-	0.69
Scheil	-	13.64

The experimental results are between the calculated values. This indicates that both CRs are too fast to fulfil the requirement of an equilibrium-like solidification. However, the cooling rates are slow enough to promote more diffusion of Yttrium in α-Mg during the solidification of the alloy than predicted by Scheil. The secondary phase fraction is more than doubled if the CR is increased from 20 to 100 K/min. Since the solidification range is the same (~51°C) the estimated times of the solidification are: ~2:30 min and ~0:30 min. Thus the ~2 minutes different in solidification time resulted a significant drop (half) of the residual liquid when the melt reaches the T_E.

It should also be noted that the micrographs show brighter particles (RERPs), with higher Y concentration. They will be discussed in the next sub-chapter.

RERPs in the microstructure

The microstructural investigations of the alloy revealed some brighter particles in SEM (Figure 16 and 23.) with higher Y concentration. The SEM-EDX results of the RERPs (EDX analysis number 1, 2 and 5 in Figure 19 and in Table 5-6) show that in addition to the high yttrium concentration, the oxygen and fluorine concentrations are also high. The formation of Y_2O_3 has been already reported previously [87, 88], and formation of Y_2O_3 during the casting process is expected, but the presence of fluoride (F) is not. The source of the fluoride should the from the SF_6 cover gas (~2% SF_6 in Ar) used during the casting process. The SF_6 reacts with the Mg generally to form MgF_2 but it is possible that some of the fluorine reacts with Y rather than Mg [30]. This is not clarified and is beyond the scope this study, but the literature suggests that F_3Y phase has a high thermal stability. The third possible candidate for the yttrium-rich contamination is the formation of possible YH_2. Any RE containing magnesium alloy tends to form REH_2 during exposure to elevated temperature treatments [69], but the detection of hydrogen is not possible using any conventional detection techniques at such small volumes. Unfortunately, the major peaks of all these possible phases overlap on the SRXRD patterns and the volume fraction is too low to identify conclusively which of these 3 phases are prevalent. The SRXRD results show continuous XRD peaks which should belong to any of these phases (Figure 17 and Figure 20). These phases are stable high temperature; therefore, they do not dissolve while the alloy is molten. It indicates that these particles are unlikely to play any role in the solidification paths and they are stable even in the liquid. At the same time, these peaks can be detected from the as cast condition, thus these RERPs are from the casting process. On the other hand, the micrographs show that these particles congregate in segregated areas, mainly in the neighbouring the eutectic regions, thus these particles remain in the liquid and they just fill the residual inter-dendritic spaces at the end of the solidification. The volume fraction of these particles is between 0.3 and 0.4% (Table 5-5.).

Y has been already reported as an extremely reactive element even in solid phase [88], and has tendency to form Y_2O_3 layer on the surface of bulk material. In Liquid phase it can be even more reactive and can vary the concentration significantly and form RERPs. Since the results indicates that none of these particles affect the solidification path of the alloy there was no further study conducted on the particles. The determination of the possible RERPs remains as an open question for future studies.

6.2.2 G15 alloy

Formation temperatures and respective phases

The first phase formation occurs at liquidus temperature (T_L) during cooling. The measured temperatures are: 623.2°C by DSC, 640.2°C and 593.7°C by SRXRD at 20- and 100 K/min CRs, respectively. The SRXRD experiments clarify that the appearing XRD peaks are matching with the HCP-Magnesium peaks. The calculations predict a T_L of 623.8°C. The experimentally detected T_L are have a large range, and only the temperature measured with DSC matches with predicted calculation results.

As soon as the temperature drops below the eutectic temperature (T_E), a secondary phase starts forming. The experimentally measured temperatures are: 544.5°C with DSC, and 561.1°C and 513.4°C with SRXRD at 20- and 100 K/min CRs, respectively. The 2Θ-time graph of the SRXRD experiments (Figure 22 and Figure 23) indicate that this temperature is the end of the solidification because no liquid phase is observed after that. The predicted temperatures of the end of solidification are: 547.8°C and 575.1°C with Scheil and Lever rule, respectively. Lever approach does not predict any secondary phase formation. Thus the solidification should finish at a higher temperature with all the Gd dissolved into the α-Mg. However, all the experimental results show the formation of an intermetallic phase, which indicates that solidification did not fulfil equilibrium conditions. The fluctuation of the measured temperatures using SRXRD is larger than in the case of W15 for this alloy. However, the determined solidification ranges (ΔT) from the experimentally verified temperatures are in good agreement with each other (experiments and calculation: ~78°C). The measured and calculated temperatures are summarised in Table 6-2.

Table 6-3. The table presents calculated- and experimentally determined temperatures of the phase formations and the calculated solidification range (SR) of the G15 binary alloy.

G15 Alloy			
Method and CR [°C]	**Determined temperature [°C]**		**ΔT [°C]**
	Liquidus	**Eutectic**	
DSC 20	623.2	544.5	78.7
SRXRD 20	640.2	561.1*	79.1
SRXRD 100	593.7	513.4*	80.3
Scheil	623.8	547.8	76
Lever	623.8	575.1	48

*Solid phase transformation is observed by SRXRD.

It has been described in Chapter 5.3.2, the peaks appearing at T_E can be indexed with the major diffraction peaks of RMg_3 phase. However, according to literature secondary phase should be the RMg_5.

Metastable phase diagram can be calculated by suppressing the formation of the RMg_5 phase. However, this phase diagram reveals that the formation of the RMg_3 phase requires at least a 20°C degree undercooling (T_E=547.8°C, T_{E_m}=526.7°C) compared with the stable phase formation to RMg_5 phase (Figure 60). This should result in a significantly higher solidification range (ΔT) than the experimental results. Despite the significant thermodynamic stability difference between the IMPs, the SRXRD results show no detectable amount of the RMg_5 phase at the end of solidification is observed without any change in ΔT. However, RMg_3 phase does not stay in the microstructure, and as the 2Θ-time graphs of the SRXRD experiments (Figure 22 and Figure 23) reveal one more phase formation was observed near T_E. While the peaks of the RMg_3 phase disappear, the peaks of the RMg_5 phase appear. These results suggest that this is a complete phase transformation rather than coupled growth of two different phases.

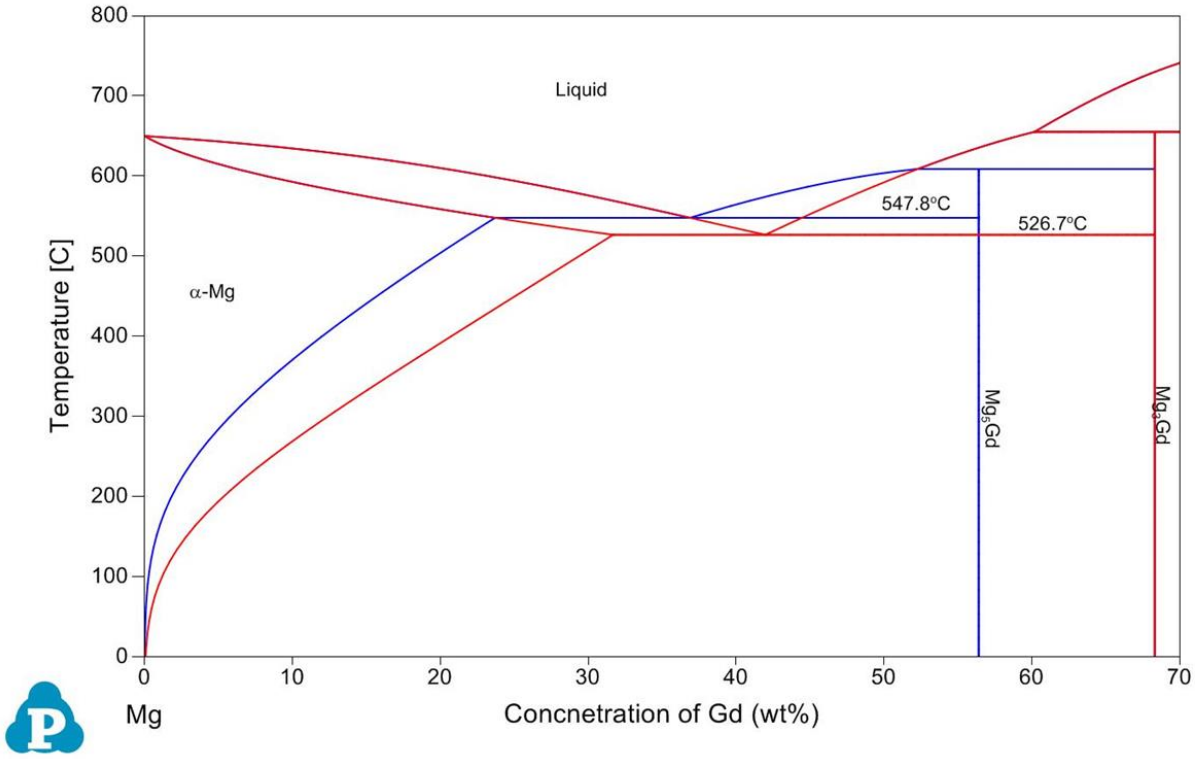

Figure 60. The stable (blue) and metastable (red) phase diagram of Mg-Gd.

The SRXRD results suggest that the initial phase is the RMg_3 phase, independent verification of this experimental results was conducted. In order to keep the RMg_3 phase in the solidified alloy a sample was quenched at a temperature just above the RMg_3 to RMg_5 transformation temperature. The TEM investigations determined the crystal structure of two different intermetallic phases (Chapter 5.6). One was the RMg_5 type structure and the second was a less pronounced phase matching the structure of the RMg_3 phase. Moreover, the TEM-EDX results show that the two phases have different chemical compositions (Chapter 5.6). Szakacs et al. reported that solidification performed even with 5 K/min CR the similar results is observed [139]. All these results show that the thermodynamically stable RMg_5 type phase is not able to form directly from the liquid in the Mg-Gd system. At T_E the solidification finishes with the secondary phase selection of the RMg_3 prior to the formation of RMg_5. Such results suggest that the formation of RMg_3 phase from the liquid is energetically very favourable compared with the formation of RMg_5.

It has been already reported that the formation of RMg_5 can be suppressed in ternary systems with addition of alloying elements such as Zn [140] or Nd [14], and that metastable RMg_3 phase forms even though it is not the thermodynamically stable phase. A small addition of Zn has been reported to stabilise the RMg_3 phase over RMg_5 phase during solidification [141] and has characterised to be a thermodynamically stable phase. The results of this study opens the possibility that during solidification: crystal structure and lattice or orientation matching plays a significantly more important role in the choice of secondary phase selection and this can lead to the formation of thermodynamically and thermally unstable phases.

E2EM method has been utilized successfully recently to understand or predict the crystallographic features between adjacent crystalline phases [15, 16, 17]. Moreover, Easton et al. proved that in RE-Mg systems among the possible R_xMg_y intermetallic phases, the RMg_3 type phase has the most preferable lattice match with the α-Mg and in Mg-Nd binary system this phase can overcome even a $\boldsymbol{\Delta T}$~14°C undercooling instability compared to that of the stable precipitate in the system. In the investigated Mg-Gd system the minimum required undercooling is ~20°C for the formation of $GdMg_3$ compared to that of the stable $GdMg_5$ phase. However, the SRXRD results indicate that the secondary phase selection is able to overcome the Gibbs potential differences between the phases due to the possible high interface energy differences. On the other hand, due to the large discrepancy in the free energy minimisation needed further cooling will provide for sufficient energy to allow a further phase transformation to the thermodynamically stable phase, as the required diffusion distances are likely to remain very small. This can provide the driving force the transformation to the stable $GdMg_5$ phase even at faster CRs and can explain the fact: that the final microstructure containing only the stable RMg_5 intermetallic. Further investigations based on much higher cooling rates may be required to stabilise the $GdMg_3$ phase in the binary system.

This phenomenon could not have been detected with DSC or other techniques that does not concurrently measure both the thermal profile during solidification and the phase and microstructure evolution. Since the phase transformation temperature is close to the eutectic temperature, the peaks of formation (the solid phase transformation from $GdMg_3$ to $GdMg_5$ and the formation of the $GdMg_3$) overlap and would be beyond the resolution of best DSC. Therefore,

the thermodynamic calculations are not able to predict the same solidification path as that observed experimentally with SRXRD.

As a summary of this subsection:

- greater than expected but consistent temperature shift is seen with SRXRD,
- all experimental and calculated results show the same SR (~78°C),
- SRXRD clarifies the first phase formation as α-Mg,
- SRXRD identifies a metastable secondary phase formation at T_E (~547°C),
- the metastable phase can be indexed with the diffraction peaks of the RMg_3,
- SRXRD detects a solid state phase transformation $GdMg_3$ to RMg_5.

Intermetallic phase fraction

As concluded before, the solidification sequence of the alloy consists of four stages. The first stage is the molten stage, second stage commence at T_L, is where liquid and α-Mg coexist. At T_E, beginning of the third stage, α-Mg and the eutectic structure form with the combination of α-Mg and metastable $GdMg_3$. Finally, the in the fourth stage the initial phase $GdMg_3$ transforms to the stable $GdMg_5$. This means that two IMPs appear during the solidification experiments but only one remains in the final room temperature microstructure. The metastable $GdMg_3$ IMP transforms into $GdMg_5$. Therefore, the fraction of the $GdMg_3$ phase is always zero in the microstructures examined.

The area fraction of the intermetallic phase RMg_5 in the solidified microstructures are presented in Figure 25, while the evaluated values are presented in Table 5-7. The calculated results are presented in mole fraction in Table 5-9. The area fraction of the IMP is 4.9 and 10.2 % with CRs of 20 and 100 K/min, respectively. The predicted calculation results are 0 and 4.97 mole% with Lever-rule and Scheil model, respectively. The results are summarized in Table 6-4.

Table 6-4. The fraction of the intermetallic phase $GdMg_5$ in the microstructure of the G15 alloy, determined by experimentally (area fraction of SRXRD samples) and predicted by Pandat both Lever rule and Scheil model (mole fraction).

IMP fraction in G15 [%]		
State	**area**	**mole**
SRXRD20	4.9	-
SRXRD100	10.2	-
Lever	-	0
Scheil	-	5.1

Since the Lever-rule predicts no secondary phase formation, the experimental results indicate that the chosen CRs are far from equilibrium condition, as the solidification ends with the formation of a significant amount of IMP. On the other hand, the mole fraction of the calculation is still difficult to correlate directly since the actual amount of Gd in the alloy is really low due to the high atomic mass. However it can be admitted that the experimentally observed IMP fraction is doubled if the CR is increased from 20 to 100 K/min. The slower the CR is, the more time is available for the Gd to diffuse into the solid phase and this results in a lower (half) volume of residual liquid which reaches the eutectic point. This is similar to that is observed with Y in the W15 alloy, but the solidification range (times) and actual atomic concentrations are different. The determined solidification ranges (ΔT) is: ~78°C, which means ~0:45 and 3:45 min solidification times with CR 100 and 20 K/min, respectively. Additionally the atomic concentration of the Gd in the alloy is around half of the Y concentration in W15. It indicates that the diffusion coefficient of Gd and Y during the solidification are not similar as they are examined equally in former studies in solid states [82].

RERP in the microstructure

As mentioned in the former Chapter 5.3, the microstructural investigations of the alloy revealed some brighter particles with higher amount of Gd (RERPs). These particles are likely gadolinium-hydrides (GdH_2) [69] or some GdO. However, Xin Tong et al found that these Gd rich particles are: GdMg or $GdMg_2$ [83]. The volume fraction of these particles is less than 0.1% (Table 5-7).

The common behaviour of all these particles is that all of them can be found in the inter-dendritic regions, specifically within the eutectic regions (in agreement with literature observations), thus they do not seem to play any role during the solidification of the alloy. It is likely that their volume fraction and cross-section ratio together are so small that the weak diffracted peaks are not detectable during the SRXRD experiments either.

6.3 Discussion of the results of the ternary Mg-Y-Gd alloys

In Chapter 5.4 the results from the solidification experiments of the ternary alloys were presented and showed that all the selected alloys have three stages during the solidification with the formation of α-Mg and an intermetallic phase (except WG510 20 K/min). The three stages are: the melt, formation of α-Mg and the formation of the intermetallic phase R_5Mg_{24}. The intermetallic phase remained constant as R_5Mg_{24} for the Mg-(15-x)Y-xGd alloys (where x=7.5 and 5) but the volume fraction and the chemical makeup of the intermetallic phase changed. The differences and similarities observed during solidification experiments will be compared and discussed with thermodynamic calculations using Pandat Thermodynamic software in this section.

Formation temperatures and respective phases

WG105

The α-Mg and R_5Mg_{24} phases were observed with both CR, as presented earlier and the formation temperatures changed with CR. The α-Mg start to form at the liquidus temperature (T_L), which was determined experimentally as: 616.7°C using DSC, while 622.7°C and 611.4°C using SRXRD at 20 and 100 K/min CRs, respectively. The calculated results are 613°C. The phase identified as α-Mg from the SRXRD peaks.

The next phase to solidify is the intermetallic phase which solidifies at solidus temperature (T_2). The temperatures recorded for T_2 are: 554.9°C with DSC, while 561.3°C and 550.1°C with

SRXRD at 20- and 100 K/min CRs, respectively. The data calculated with Scheil is 562°C, while Lever-rule does not predict the formation of IMP and the solidification complete at T_2=564°C.

Scheil predicts the formation of the R_5Mg_{24} phase at T_2, which is observed during the SRXRD experiment and subsequent data analysis. The measured temperatures vary within ~10°C range deviation but the temperature difference between T_L and T_2 (ΔT_1) remains constant for the alloy regardless to the measurement mode at: ~61°C. These ΔT_1 values are higher than those to be determined from predictions; 49°C and 51°C with Leve-rule and Scheil model, respectively.

However, the SRXRD result does not show any liquid fraction after T_2 (Figure 37), but the Scheil approach expect a significant amount of liquid fraction at this temperature. Moreover, it predicts an additional ~17°C drop of temperature to T_E where the solidification ends (545°C). It would result a ΔT_2: ~68°C, with the formation of the intermetallic phase RMg_5. None of the experimental methods (including microstructure analysis) was able to detect presence of RMg_5 or any further IMP. The values are summarized in Table 6-5 together with the other two ternary alloy.

WG77

The experimentally determined T_L of the WG77 alloy is 623.4°C using DSC, 618.7°C and 614.1°C with SRXRD at 20- and 100 K/min CRs, respectively. The calculations predict 620°C as T_L. All experimental data are in a good correlation with the calculated data.

The temperatures recorded for the secondary phase formation at T_2 are: 551.4 °C using DSC, while 549.3 °C and 547.9 °C with SRXRD at 20 and 100 K/min CRs, respectively. The predicted temperatures for T_S are: 555°C (Scheil) and 570°C (Lever). Scheil model predicts the formation of R_5Mg_{24} phases, it is clarified by SRXRD, while Lever rule does not predict formation of any intermetallic phase but the ends of solidification is at T_2=570°C. The measured values show a ΔT_1=69±3°C. Although, according to the predictions of Scheil the solidification should progress further till the end of the solidification at T_E (545°C), which results a ΔT_2= 75°C, with a formation of the RMg_5 phase. There is no indication experimentally of the formation of this IMP. The

SRXRD result does not show the presence of liquid phase after T_2 (Figure 35). The values are summarized in Table 6-5 together with the other two ternary alloy.

WG510

The start of the solidification of WG510 with the formation of α-Mg at T_L is: 618.1°C using DSC, 605.2°C and 611.3°C with SRXRD at 20 and 100 K/min CRs, respectively. The calculations predict a T_L: 615°C. The SRXRD profiles shows that the α-Mg formation very close to this temperature, but the 20 K/min experiment suggest that another phase form together with α-Mg. The SEM-EDX results show Al in some intermetallic particles in this particular specimen (Figure 45). The EDX results reveal that there are particles with high RE and Al concentration. The R:Al ~ 1:2 atomic ratio and SRXRD peaks are matching with the peaks of the possible RAl_2 phase. This phase has a high temperature stability, so it can easily form. As the solidified particles of this phase float in the melt, their detection is difficult. Most likely that RAl_2 phase is detected at the first time as the system reaches the T_L. The microstructural analysis revealed that the RAl_2 particles are separated from the eutectic region and the microstructure investigation show that this phase sits in the middle of Mg dendrites. It is possible that these RAl_2 phase act as a heterogeneous site for nucleation of α-Mg dendrites. Additionally, the SRXRD revealed that with the decrease in temperature the intensity of the α-Mg peaks become more pronounced. The intensity of the RAl_2 phase remains constant. Thus, the RAl_2 phase from in the liquid and do not continue to form or further grow during further cooling.

Although the start of the solidification differs between each other, but both SRXRD show the formation of the same intermetallic phase following the α-Mg phase. As soon as the temperature become T_2, the IMP R_5Mg_{24} begins to form at measured temperatures of 550.9°C with DSC, 543.7°C and 546.2°C using SRXRD at 20 and 100 K/min CRs, respectively. The determined ΔT_1 is: 67.1°C with DSC, 61.5°C and 65.1°C using SRXRD at CR 20 and 100 K/min, respectively. The Scheil predicts 549°C for the formation of R_5Mg_{24} phase, which results ΔT_1=66°C. The SRXRD shows peaks corresponding to the R_5Mg_{24} phase formation. Lever-rule does not predict any secondary phase with this alloy and solidification should be complete at 563°C (ΔT_1=52°C).

Although, the SRXRD result does not show any liquid phase after the formation of R_5Mg_{24} phase (Figure 46) at T_2. The SM prediction expects the formation of the RMg_5 phase at T_E (545°C), which would show a ΔT_2= 70°C. Neither of the method found formation of RMg_5 phase experimentally. The values are summarized in Table 6-5 together with the other two ternary alloy.

Summary of this section

The solidification experimental results from SRXRD match well (except WG510 SRXRD 20 because of an Al contamination) with the DSC thermal profiles during solidification and show only α-Mg and R_5Mg_{24} phase formation where ΔT_1 are determined from the experimental results. The experimentally determined ΔT_1 are: ~61°C (WG105), ~70°C (WG77) and ~66°C (WG510). The Lever rule does not expect any intermetallic phase formation and much narrower ΔT_1 are determined in each cases, while the Scheil predicts the formation of two different IMP with the 2nd intermetallic phase at T_E (545°C), which results in a much broader ΔT_2 compared with that experimentally observed. However, Scheil values are suitable for determining the solidification ranges of the alloys and these values are generally closer to the experimentally determined ΔT_1.

Table 6-5. The table presents calculated- and experimentally determined temperatures of the phase formations and the calculated temperature ranges between transformations. The T_L-T_2=ΔT_1 and their full solidification ranges T_L-T_E=ΔT_2.

Alloy	Method and CR [°C]	Determined Phase Formation Temperature [°C]			ΔT_1[°C]	ΔT_2 [°C]
		T_L:α-Mg	T_2:R_5Mg_{24}	T_E:RMg_5		
WG105	**DSC 20**	*616.7*	*554.9*	-	*61.7*	
	SRXRD 20	*622.7*	*561.3*	-	*61.4*	
	SRXRD 100	*611.4*	*550.1*	-	*61.3*	
	Pandat (Scheil)	*613*	*562*	*545*	*51*	*68*
	Pandat (Lever)	*613*	*564**	-	*49*	
WG77	**DSC 20**	*623.4*	*551.4*	-	*72.1*	
	SRXRD 20	*618.7*	*549.3*	-	*69.4*	
	SRXRD 100	*614.1*	*547.9*	-	*66.2*	
	Pandat (Scheil)	*620*	*555*	*545*	*65*	*75*
	Pandat (Lever)	*620*	*571**	-	*50*	
WG510	**DSC 20**	*618.1*	*550.9*	-	*67.1*	
	SRXRD 20	*605.2*	*543.7*	-	*61.5*	
	SRXRD 100	*611.3*	*546.2*	-	*65.1*	
	Pandat (Scheil)	*615*	*549*	*545*	*66*	*70*
	Pandat (Lever)	*615*	*562**	-	*52*	

*There is no secondary phase formation, but the solidification ends at that predicted temperature.

The WG510 alloy solidification at CR of 20 K/min has to be excluded from some conclusion as the microstructural investigations of that sample revealed the presence of Al contamination in the alloy. The contamination resulted a different solidification paths with an additional RAl_2 phase formation. The presence of this phase lowered the ΔT_1 significantly. The contamination modified the solidification path of the alloy and created a new system.

WG77 sample with CR of 100 K/min shows a narrower ΔT_1 compare to that of the same alloy examined with CR of 20 K/min SRXRD or DSC. In the same time the microstructure analysis revealed a significant drop of the Gd concentration in the sample with an increased amount of contamination in the microstructure. This will be further discussed in a later subchapter.

Intermetallic phase Fractions

The experimental results reviled that the microstructure of the ternary alloys contains only R_5Mg_{24} type intermetallic phase in the eutectic structure, and some undissolved RE rich particles. The experimental results indicate that the RERPs did not affect the solidification path, therefore they will be discussed in the next sub-chapter. The experimentally determined are fractions are compared with the predicted mole fractions of the IMPs. The values are summarised in Table 6-6.

Table 6-6. The experimentally determined area fractions of the intermetallic phase(s) in the microstructure and calculated mole fraction results of IMPs in the examined ternary alloys.

IMP fraction [%]					
Alloy	**State**	**Secondary**		**Ternary**	
		area	**mole**	**area**	**mole**
WG105	**SRXRD20**	*7.54*	-	-	-
	SRXRD100	*11.42*	-	-	-
	Lever	-	*0*	-	*0*
	Scheil	-	*12.69*	-	*0.27*
WG77	**SRXRD20**	*4.32*	-	-	-
	SRXRD100	*9.51*	-	-	-
	Lever	-	*0*	-	*0*
	Scheil	-	*8.82*	-	*0.67*
WG510	**SRXRD20**	*4.94*	-	-	-
	SRXRD100	*10.78*	-	-	-
	Lever	-	*0*	-	*0*
	Scheil	-	*7.98*	-	*2.29*

Scheil model predicts the formation of two different IMPs: R_5Mg_{24} and RMg_5 in each alloy. On the other hand the Lever Rule does not expect any IMP formation of any of the alloys. The

comparisons between the experimental results and the thermodynamic calculations show that the thermodynamic calculations do not able to predict the correct fractions compare to that the experimental fractions. The RMg_5 phase did not appear in any of the alloys so this fraction is always zero for the experimental results. The Scheil model expects a mole fractions of the RMg_5 phase are: 0.27, 0.69, 2.27 % in WG105, WG77 and WG510, respectively. The expected amount of ternary phase in WG510 should be easily detectable with any of the applied methods.

The experimental CRs are too fast to fulfil the requirements of the equilibrium solidification, thus Lever rule cannot be applied either. The R_5Mg_{24} phase contains a mixture of Gd and Y which sits at the R positions of the crystal structure thus, their contribution will be discussed in the last subchapter of this section.

RERP in the microstructure

The WG510 alloy with a CR of 20 K/min had some Al contamination. This contamination resulted a visible ~ 1% of RAl_2 phase formation. The presence of this phase in the microstructure was not expected and should be considered as a contamination, but this phase has a significant effect on the solidification paths, therefore it has to be mentioned that this is already a different alloy. The evidence that the contamination affected only that certain sample is revealed from the experiment itself. The 2Θ-time profiles (Figure 61) shows the entire experiment. The major peak of the RAl_2 appears only after the melting and not in the original alloy.

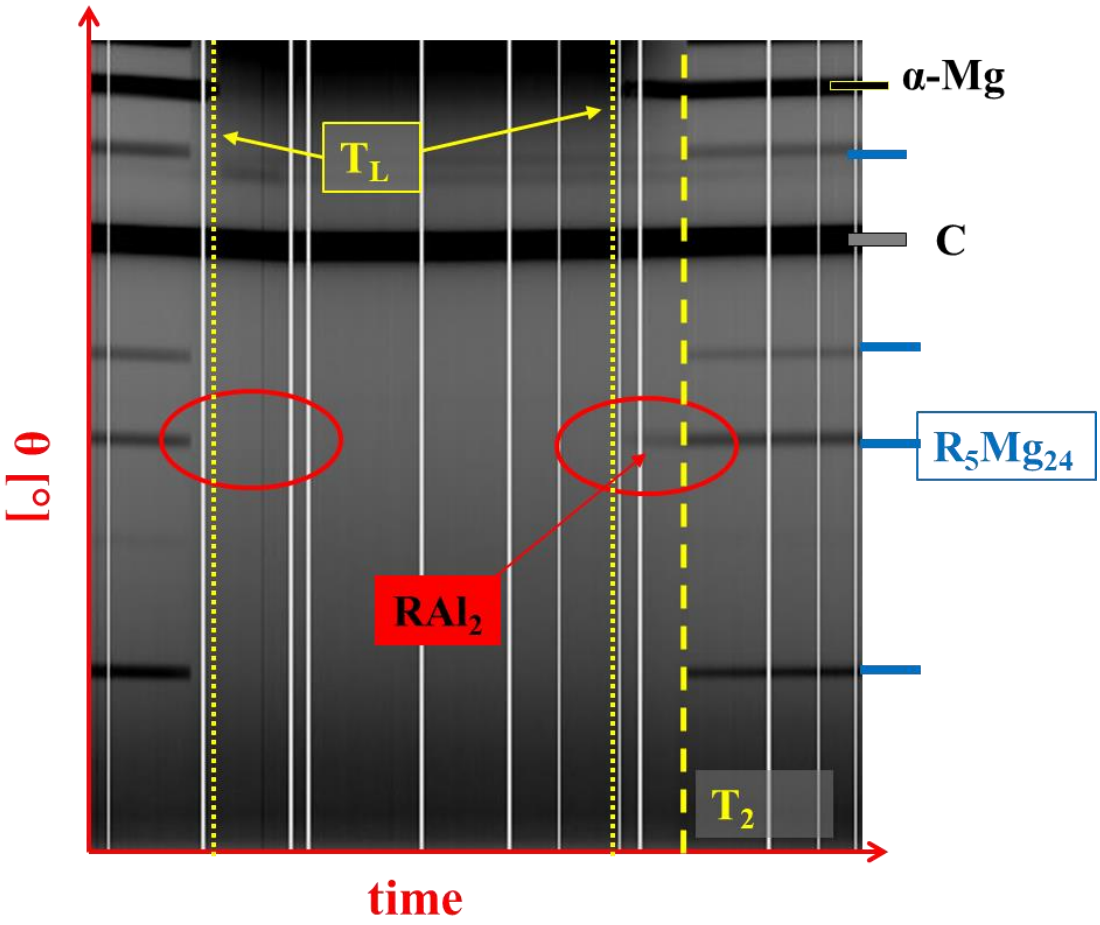

Figure 61. The 2Θ-time diagram of the 20 K/min experiment. Yellow dot lines show the T_L during the heat up (left) and during the cooling/solidification (right). The yellow dash line shows T_2 where the secondary R_5Mg_{24} type phase formation observed. The second XRD peak of the R_5Mg_{24} phase overlaps the strongest XRD peak of the RAl_2 phase. During the solidification this peak appears together with the α-Mg peaks (red circle on the right). However, the heat up stage does not show the presence of the phase, which indicates that the Al contamination occurred during the solidification experiment.

The microstructural investigations of the ternary alloys showed some brighter particles (in SEM) with higher Y and/or Gd concentration and called RE rich particle (Figure 30, Figure 36, Figure 40, Figure 44). Although samples had similar contamination in the microstructure regardless of the CR, the specimens examined with 100 K/min generally showed a more pronounced feature. The SRXRD results show a continuous XRD peaks which could belong to high temperature stable phases, such as rare earth-hydrides, oxides or fluorides. The detection of these phases can be seen

in the as cast condition using XRD, thus these possible contaminations are the results of the production route.

Although the hydride, oxide and fluoride contaminants do not seem to have any effect on the solidification paths but they may have a slight influence on the solidification temperature. Due to a high concentration of rare earth elements in these particles, the total amount of alloying elements available decreases and may shift the T_L and T_2 along with ΔT_1. The experimentally determined ΔT_1s are in a good agreement to each other, however in two specimens (WG510 CR20 and WG77 CR100) the measured temperatures indicates ΔT_1 may be shifted.

WG510 with CR of 20 K/min has a ~5°C narrower ΔT_1 from the Scheil predicted ΔT_1. In this case there is an Al contamination which is described previously.

WG77 with CR of 100K/min has a ΔT_1 value that is ~6 °C smaller than other experimental values. The microstructure investigation of the as-solidified specimen shows the highest area fraction of RE rich particle (~1.8 %) with a significant drop of concentration of Gd. Additionally, this is the only specimens where the intensity of the peaks, which belong to the possible RE rich particles, increase during the experiment. All these results indicate that during the solidification experiments some Gd-hydride or oxide formed resulting (together with the residual contamination from the casting) an unexpectedly strong set of diffraction peaks of RE rich particles (Figure 38). This result shows the sensitivity of the applied set up to the small volume fraction of RERPs. Due to the fact that RE rich particles containing mainly Gd (Z= 64) and Y (39), and they are in a matrix which is mainly Mg (12), even with a total area fraction of less than 2% RERPs in the microstructure, they are detectable in both the SEM (Figure 40) and 2D-XRD patterns from SRXRD.

The RERPs are the result of the casting process, but the samples examined with CR of 100 K/min generally show pronounced particles than the samples examined with CR of 20 or in the as-cast conditions. Therefore, the deeper analysis of these particles took place only after the solidification experiments of 100 K/min. The typical RERPs are discussed together and compared with each other including some RE rich particles from W15.

The same sort of features are observed in alloy WG77 (Figure 40 point: X_1), WG510 (Figure 44: X_5) and the binary W15 (Figure 19: X_2). These particles look similar between the alloys and high level of RE concentration and moderate oxygen concentration is determined from the SEM investigations. Rare earth-hydrides (RH_2) particles tend to form during any high temperature treatment including casting [70]. The Hydrogen cannot be determined with EDX. However, the literature suggest that the presence of these particles is expected and looks similar that observed in prior publications. These particles are more likely that rare earth-hydrides (RH_2). These particles are present everywhere in the microstructure and not confined to the inter-dendritic regions.

Other type of RE rich particles look like an extra "bony" features on the eutectic structure. In the alloy WG105 (Figure 36: X_1) or in WG77 (Figure 40: X_3, X_5) the EDX results are similar: the major element is yttrium, with a smaller concentration of gadolinium and high concentration of oxygen and surprisingly a significant amount of fluorine. The same feature without any Gd is also observed in W15 alloy (Figure 19: X_1). The probability of the formation of Y_2O_3 is high according to literature [87], but fluorine (F) containing particle is unexpected. More likely, that these areas are the combination of Y_2O_3 and some F containing RE particles or MgF_2 particles that form during casting too as a part of protective layer under SF_6 cover gas. However, future TEM analysis is required to determine the exact structure and chemical composition of these particles. These areas were present mainly in three alloys: WG105, WG77 and the binary W15. The WG510 does not show the presence of detectable F. This indicates that the F based particles are similar to that what was expected in W15: YF_3. The increased enrichment of Gd in the alloy results in a lower amount of detectable F. Probably the yttrium has a high tendency to react with the cover gas SF_6 during the casting process. In the WG510 the bright segregated areas more likely the combination of Y_2O_3 and GdO.

However, the results of the temperature measurement indicate that the effect due to the RE rich particles is not significant, and more likely that none of these particles affect the solidification path of the alloy and the strongest XRD peaks of these phases overlaps to each other. Therefore, there was no further study on the particles. These particles probably Y and Gd oxide (Y_2O_3, GdO), rare

earth- hydrides (YH_2, GdH_2) with a high probability of yttrium-fluorides (YF_3). The volume fraction of these particles are presents Table 6-5.

Table 6-7. The results of the area fractions of the RERPs in the ternary alloys with the two examined cooling rates (20 and 100 K/min.).

Alloy	Cooling rate	Volume fraction of cont. [%]
WG105	**20**	*0.36*
	100	*0.76*
WG77	**20**	*0.42*
	100	*1.78*
WG510	**20**	*0.94*
	100	*0.24*

The analysis of the R_5Mg_{24} phase in the ternary alloys

Regardless the alloy composition, level of contamination or the CR, the secondary phase selection during all the solidification experiments is the same. The R_5Mg_{24} is the only intermetallic phase which forms from the liquid at various T_S and remains in the microstructure. However, the volume fraction and chemical makeup of the intermetallic phase ranges among the as-solidified samples. The volume fraction of the R_5Mg_{24} is presented in a former subchapter, therefore in this subchapter focus is on the chemical composition of this phase. The composition was determined with SEM-EDX in three different conditions: as-cast and as-solidified with both CR. The as-cast condition was also used for the TEM investigation to and TEM-EDAX was performed on the phase to confidently identify the structure and chemical composition of the R_5Mg_{24} phase.

TEM investigation showed that there is no other intermetallic phase than R_5Mg_{24} in the eutectic structure (Figure 31, Figure 32, Figure 33). However, the composition of the phase contained both Gd and Y and thus this phase should be considered to be $(Gd,Y)_5Mg_{24}$. The TEM-EDAX also revealed that the only different in the phase in the alloys investigated is the concentration ratio of Gd and Y in the IMP.

WG105 and WG77 have a similar Y:Gd atomic (weight) ratio which are: ~11:5 (5:4) and ~7:3 (4:3). The SEM-EDX analyses of the two alloy in as-cast and as-solidified with CR of 100 K/min conditions are similar (except in case of WG77 CR 100, due to the significant Gd loss). Although, the remarkably close ratio between the two alloys would suggest that the Y atoms can be exchanged ~33% to Gd and would point to a possible maximum solid solubility of Gd in R_5Mg_{24} phase. The same alloys with a CR of 20 K/min investigated with SEM-EDX shows the atomic ratio of Y:Gd close to a 1:1. Additionally, the TEM-EDAX results of the WG510 alloy shows an atomic (weight) ratio of Y:Gd = 1:2 (2:7). However, the results of the SEM-EDX varies among the three conditions but shows a higher Gd concentration compare to that of Y in the intermetallic. The presence of Gd in R_5Mg_{24} is twice as much as Y. The certain alloy has more or less 1:1 atomic ratio of the Y:Gd initially, but the phase produced a 1:2 atomic ratio when analysed with TEM.

The WG510 alloy was expected to be close to eutectic concentration, (Gd:Y~1.2 atomic) and it was expected during the solidification for two different intermetallic phases to form. However, the results indicate that the diffusion of the Gd into the α-Mg was significantly slower and resulted a Gd rich residual liquid phase (Gd:Y= ~2) (which should be already on the other side of the eutectic point between R_5Mg_{24} and RMg_5) when the temperature reach the solidus line. The probability of the formation of RMg_5 phase should be even higher than expected, but it was not observed. It means that the Gd rich side of the phase diagram is more likely to form a $(Gd,Y)_5Mg_{24}$ type secondary phase instead of RMg_5. In order to confirm this hypothesis, further investigations are required.

According to the kinematical scattering theory, X-ray diffraction peaks broaden either when crystallites become smaller than about a micrometre or if large fraction of lattice defects are present [118]. In this study the broadening of the major peaks of the intermetallic phases was compared alloy by alloy with the 100 K/min CR. For a possible better correlation even the binary W15 alloy was included in the analysis. The results of the TEM-EDAX revealed that the phase has a high capacity to exchange or dissolve high amount of gadolinium, probably at the position of Y atoms. In TEM with the change in Gd:Y ratios indicates a possibly detectable change in the measured d-spacing. Both peak shifts and broadening of the peaks are expected in the SRXRD. The two most

intensive peaks of the R_5Mg_{24} phase (<220> and <211>) were compared. The results of the fitting are presented in Figure 47 and Figure 48 while the values are in Table 5-21. There is no detectable peak position change but the full width half maximum values (FWHM) shows a small fluctuation. The maximum differences are 40% compare to the binary values. This indicates some possible extra internal stress induced probably due to the changes in chemical composition. However, the experimental set up was not adjusted according to this type of analyses to make any strong conclusion but the data still provide some indication for promising future work. If the sample environment and beam energy would be adjusted according to this analysis, even these as-solidified samples could provide us both quantitative and qualitative information.

7 Summary and Conclusion

Majority of magnesium alloys are produced in the form of castings; thus their microstructure and consequently macroscopic mechanical properties are determined during the solidification. Therefore, understanding the solidification mechanisms is necessary in order to be in control during the casting process. Mg-RE alloys have been already of interest as light weight, high temperature creep resistant structural materials for transportation, but they have become even more attractive for bio-medical application during the last decades. Mg-Y-Gd alloys could be suitable candidates for both applications, but the microstructure evolution of this system has not been investigated to understand the types of intermetallic phases present during solidification. Szakacs et al reported that [132] in dilute ternary alloys $Mg_{24}(Y,Gd)_5$ phase was prevalent. However, due to the low concentration of Y and Gd it was difficult to follow the microstructure evolution during solidification nor was it possible to conclusively show the formation of various intermetallic phases, thus more concentrated alloys are needed to understand the phase evolution during solidification. In order to evaluate the effect of Gd content in Mg-(15-x)YxGd alloys were investigated (x=0, 5, 7.5, 10, 15). Besides microstructure investigation (LOM, SEM, TEM), *in situ* experiments during solidification were performed on the chosen alloys with synchrotron radiation diffraction and DSC. Using synchrotron radiation-based X-ray diffraction during the solidification of Mg-RE alloys is a powerful tool. Even in a simple well studied binary system (Mg-Gd), it supplies unique information which may result in a revision or modification of thermodynamic database. Moreover, it can extend our ability to make further investigations in realistic casting conditions and make it possible to predict more accurately the solidification sequences of the alloys. Thus we have the opportunity to optimize process routes of an alloy in order to achieve the desired microstructure and property profile of a product for a wide range of applications. The experiment results were correlated with Scheil model calculation using Pandat software [10]. The results of the investigation can be summarized as the following:

1. The binary G15 specimens with *in situ* synchrotron radiation diffraction show the formation of a metastable phase (with a structure of Mg_3Gd phase) at eutectic temperature from the liquid and then it transforms to the expected (both from

calculation and available literature) equilibrium state stable Mg_5Gd regardless from the applied cooling rates [139].

2. The experimental results of the binary W15 alloy consistently produces a narrower solidification range and higher eutectic temperature of the system than it is expected from the determined results from calculations.
3. The Gd addition into the Mg-Y-Gd ternary alloys did not change the route of the solidification paths in neither applied cooling rates, and only one intermetallic phase (structure of R_5Mg_{24} phase) formation can be observed [142]. These results are not in correlation with neither thermodynamic calculations nor the available literature.
4. The formation of RMg_5 type intermetallic phase was observed only in the binary G15 alloy. The formation of the phase was observed only due to a solid phase transformation after the solidification was complete.
5. The intermetallic phase R_5Mg_{24} in the ternary alloys shows a high exchange ratio of RE elements and results an $(Y,Gd)_5Mg_{24}$.
6. The applied cooling rates were not affecting the order of the secondary phase selection, however they resulted different volume fraction of intermetallic phase and varied the chemical composition of the intermetallic phase in the ternary alloys.

8 Future Work

In this study the solidification behaviours of three different Mg-xY-(15-x)Gd alloys were investigated with the total solute content being 15wt% to investigate the phase evolution during solidification of these alloys. Additionally, the two binary alloys were also investigated. Number of general conclusions were drawn and presented in the previous sections. However, further investigations based on different alloy compositions and cooling paths. Some of the pertinent experiments include the following:

1. To verify the formation of $GdMg_3$ phase both *in situ* and *ex situ* solidification experiments with SRXRD or DSC needs to be conducted where investigated specimens are quenched at or close to the intermetallic transformation temperatures. These needs to be investigated both using microscopy techniques to verify the phases and further thermal profiles to determine whether any subsequent thermal signature could be detected that show the solid-state phase transformation from $GdMg_3$ to $GdMg_5$ phase observed at room temperature.

2. The solidification of ternary alloys show that the phase evolution determined through Scheil model calculations and the experimental results do not correspond to each other as no $GdMg_5$ phase was observed in any of the ternary alloys, even though this phase was expected for all three. Alloys with compositions which allow for $GdMg_5$ phase to form as the first intermetallic phase needs to be investigated to see whether this phase will indeed occur during solidification. Based on the liquidus projection of the Mg rich end of Mg-Gd-Y system, Figure 50, an alloy with a composition of approximately 14wt% Gd and 1wt% Y may be suited for such investigation. In this case the solidification path should be

   $$\text{Liquid} \rightarrow \alpha\text{-Mg} + \text{Liquid} \rightarrow \alpha\text{-Mg} + (\text{Gd,Y})\text{Mg}_5 + \text{Liquid} \rightarrow \alpha\text{-Mg} + (\text{Gd,Y})\text{Mg}_5 + (\text{Gd,Y})_5\text{Mg}_{24}$$

   This should verify two different aspects of the alloy, Firstly whether indeed the ternary phase diagram is accurate and also whether the $GdMg_5$ phase remains stable with the

incorporation of Y or as the case with Mg-Gd-Nd system where $(Nd,Gd)Mg_3$ phase is stabilised in place of the $GdMg_5$ phase

3. In order to determine whether indeed the position of the eutectic point observed in the Mg-Gd-Y system calculated based on prior experimental data a composition that would allow the following phase transformation to occur needs to be investigated

$$Liquid \rightarrow \alpha\text{-}Mg + Liquid \rightarrow \alpha\text{-}Mg + (Gd,Y)Mg_5 + (Gd,Y)_5Mg_{24}$$

A composition close to on at 13.5wt%Gd and 1.5wt%Y would be appropriate for this investigation as this combination would allow the alloy to follow a solidification path where α-Mg forms from the liquid and upon further cooling $(Gd,Y)Mg_5$ and $(Gd,Y)_5Mg_{24}$ phases formed concurrently along with Mg at the eutectic point. This would provide pertinent information to verify the existing phase diagram and also the role of Y in stabilising $GdMg_5$ or $GdMg_3$ phase during solidification

4. This investigation was conducted on Mg alloys with rather high concentration of RE elements to allow for the investigation of phase evolution during solidification and the role of cooling rate on the volume of phases detected. However, these alloys are not suited for either structural or bio-implant applications due to the high level of alloying additions. Thus, to develop a novel system that is of use for such applications lower levels of alloying additions with similar wt. ratio of Y:Gd to investigate a combination of mechanical property requirements and corrosion investigation.

5. Recently, Ag has been considered to be in important addition to bio-implants to improve the anti-bacterial properties [143]. However, the solidification paths and phase evolutions of Mg-Y-Ag, Mg-Gd-Ag and the Mg-Y-Gd-Ag system is far from being fully investigated or understood. However, quaternary alloys containing these elements are investigated to at present. To supplement such investigations a phase evolution coupled with solicitation study is necessary.

9 References

[1] A.A Luo,” Magnesium casting technology for structural applications.”, Journal of

Magnesium and Alloys 1 (2013) 2-22

[2] W.J. Joost and P.E Krajewski, “Towards magnesium alloys for high-volume automotive applications.”, Scripta Materialia 128 (2017) 107–112

[3] A.A. Luo and K. Sadayappan, “Technology for Magnesium Castings”, *American Foundry Society*, Schaumburg, IL, (2011) 29-47

[4] M.M. Avedesian and H. Baker, “Magnesium and Magnesium Alloys.”, *ASM International* Materials Park, OH, 1999.

[5] J.A. Dantzing and Rappaz, “Solidification.”, *EPFL Press A Swiss academic publisher distributed by CRC press* (2009)

[6] R. Schmid-Fetzer, “Phase diagrams: The beginning of Wisdom.”, *Journal of Phase Equilibria and Diffusion* 35 (6) (2014) 735-760

[7] G.H. Gulliver,”The quantitative effect of rapid cooling upon the constitution of binary alloys”, Journal of Institute of Metals 9 (1913) 120-157

[8] D.A. Porter and K.E. Easterling, “ Phase transformation in Metals and Alloys.” *Springer-Science+Business Media, B.Y.,* second edition (1992)

[9] A. Costa e Silva, J. Agrens, M. T. Clavaguera-Mora, D. Djurovic, T. Gomez-Acebo, B. J. Lee, Z. Liu, P. Miodownik, H.J. Seifert, “Applications of computational thermodynamics — the extension from phase equilibrium to phase transformations and other properties.”, *CALPHAD* 31 (1) (2007) 53-74

[10] Pandat Software and PanMg database, Release Date: 2017, CompuTherm LLC, Madison, WI, USA, http://www.computherm.com.

[11] S. Delfino, A. Saccone, R. Ferro , “Phase relationships in the neodymium-magnesium alloy system.”, *Metallurgical Transactions A* 21 (8) (1990) 2109-2114

[12] S. Gorsse, C.R. Hutchinson, B. Chevalier, J.-F. Nie,” A thermodynamic assessment of the Mg–Nd binary system using random solution and associate models for the liquid phase.”, *Journal of Alloys and Compounds* 392 (1-2) (2005) 253-262

[13] T.L. Chia, M.A. Easton, S.M. Zhu, M.A. Gibson, N. Birbilis, and J.F. Nie, “The effect of alloy composition on the microstructure and tensile properties of binary Mg-rare earth alloys.”, Intermetallics 17 (7) (2009) 481-490

[14] A. Kielbus, T. Rzychon, L. Litynska-Dobrzynska, G. Dercz, “Characterization of β and $Mg_{41}Nd_5$ equilibrium phases in Elektron 21 magnesium alloy after long term annealing.”, *Solid State Phenom 163* (2010) 106-109

[15] P.M. Kelly and M.-X. Zhang, “Edge-to-edge matching - a new approach to the morphology and crystallography of precipitates.”, *Materials Forum 23* (1999) 41-62

[16] P.M. Kelly and M. -X. Zhang, “Edge-to-edge matching - The fundamentals.”, *Metall. Mater. Trans. A* 37 (3) (2006) 833-839

[17] M. -X. Zhang and P.M. Kelly, “Edge-to-edge matching and its applications: Part 2. Application to the simple HCP/BCC system.”, *Acta Materialia* 53 (4) (2005) 1073-1084

[18] M.A. Easton, M.A. Gibson, D. Qui, S.M. Zhu, J. Gröbner, R. Schmid-Fetzer, J.F. Nie, M.X. Zhang, "The role of crystallography and termodinamics on phase selection in binary magnesium rare earth (Ce or Nd) alloys.", *Acta materialia 60* (2012) 4420-4430

[19] R.H. Mathiesen, L. Arnberg, F. Mo, T. Weitkamp, and A. Snigirev, "Time Resolved X-Ray Imaging of Dendritic Growth in Binary Alloys.", Physical Review Letters 83 (1999)

[20] C. Rakete C. Baumbach, A. Goldschmidt, D. Samberg, C. G. Schroer, F. Breede, C. Stenzel, G. Zimmermann, C. Pickmann, Y. Houltz, C. Lockowandt, O. Svenonius, P. Wiklund, R. H. Mathiesen, "Compact x-ray microradiograph for in situ imaging of solidification processes: Bringing in situ x-ray micro-imaging from the synchrotron to the laboratory.", *Review of scientific instruments* 82 (2011)

[21] J. Verö, M Káldor, „Fémtan" *Nemzeti Tankönyvkiadó*, Budapest 1977

[22] H. E. Friedrich and B. L. Mordike. Magnesium Technology / Metallurgy, Design Data, Applications. 1. *Springer-Verlag*, Berlin, Heidelberg, Germany, 2006.

[23] http://periodictable.com/Elements/012/data.html

[24] http://www.chem-is-try.org/materi_kimia/kimia-anorganik-universitas/ikatan-dan-struktur/struktur-kristal-logam/

[25] K.U. Kainer, "Magnesium alloys and technology.", *Wiley-VCH, Wiheim* (2003)

[26] F. Witte, "The history of biodegradable magnesium implants: A review. "*Acta Biomaterialia*", 6 (2010) 1680-1692

[27] E. F. Emley, "Principles of magnesium technology.", *Pergamon Press / Oxford, New York*, (1966)

[28] Y. M. Kim, C.D. Yim, H.S. Kim, B.S. You, "Key factor influencing the ignition resistance of magnesium alloys at elevated temperatures.", *Scripta Materialia,* 65 (11) (2011) 958-961

[29] P. Boris. "A STUDY OF THE FLAMMABILITY OF MAGNESIUM.", *FEDERAL AVIATION AGENCY*, (1964)1–24

[30] B. Wiese, "The Effect of CaO on Magnesium and Magnesium Calcium Alloys.", Doctoral Thesis, Clausthal Univerity of Technology (2016)

[31] M.P. Staiger, A.M. Pietak, J. Huadmai, G. Dias, "Magnesium and its alloys as orthopedic biomaterials: A review." *Biomaterials* 27 (2006) 1728-1734

[32] F. Witte, V. Kaese, H. Haferkamp, E. Switzer, A Mayer-Lindenberg, C.J. Wirth, H. Windhagen, "In vivo corrosion of four magnesium alloys and the associated bone response.", *Biomaterials* (2005) 3557-3563

[33] N.T. Kirkland, J. Lespagnol, N. Birbilis, M.P. Staiger, „A survey of bio-corrosion rates of magnesium alloys." Corrosion Science 52 (2010)

[34] B.L. Mordike and T. Ebert, "Magnesium Properties-applications-potential", *Material Science and Engineering A* 302 (2001) 37-45

[35] L. L. Rokhlin, *Magnesium Alloys Containing Rare Earth Metals, Structure and Properties*, (London: Taylor & Francis, 2003).

[36] N. Hort, Y. Huang, D. Fechner, M. Störmer, C. Blawert, F. Witte, C. Vogt, H. Drücker,R. Willumeit, K.U. Kainer, F. Feyerabend; "Magnesium alloys as implant materials-Principles of property design for Mg-RE alloys" *Acta Biomaterial* 6 (2010), 1714-1725.

[37] F. Feyerabend, J. Fischer, J. Holtz, F Witte, R. Willumeit, H. Drücker, C. Vogt, N. Hort, "Evaluation of short-term effects of rare earth and other elements used in magnesium alloys on primary cells and cell lines.", Acta Biomater. (6) (2010) 1834-1842

[38] L. Yang, "Development of Mg-Re alloys for medical applications." Doctoral thesis TU Clausthal (2013)

[39] L. Yang, Y Huang, F. Feyerabend, R. Willumeit, C. Mendis, KU. Kainer, N. Hort, "Microstructure, mechanical and corrosion properties of Mg–Dy–Gd–Zr alloys for medical applications", *Acta Biomaterialia* 9 (10) (2013) 8499-8508

[40] F. Witte, J. Fischer, J. Nellesen, C. Vogt, J. Vogt, T. Donath, F. Beckmann, "In vivo corrosion and corrosion protection of magnesium alloy LAE442.", *Acta biomaterialia* 6 (2010) 1792-1799

[41] E. Lukylanova, N. Anisimova, N. Martynenko, M. Kiselevsky, S. Dobatkin, Y. Estrin, "Features of in vitro and in vivo behaviour of magnesium alloy WE43." *Materials Letters* 215 (2018) 308-311

[42] Adam J. Griebel and Jeremy E. Schaffer, "Fatigue performance of Resoloy® magnesium alloy wire.", *European Cells and Materials* (2016)

[43] H. Windhagen, K. Radtke, A. Weizbauer, J. Diekmann, Y. Noll, U. Kreimeyer, R. Schavan, C. Stukenborg-Colsman, H. Waizy, "Biodegradable magnesium-based screw clinically equivalent to titanium screw in hallux valgus surgery: short term results of the first prospective, randomized, controlled clinical pilot study.", *BioMedical Engineering OnLine* 12:62 (2013)

[44] L.L. Rokhlin and N. Nikitina, "Recovery after aging of Mg-Y and Mg-Gd alloys.", *Journal of Alloys and Compounds* 279 (1998) 166-170

[45] Y. Wu and W. Hu, "Comparison of the Solid Solution Properties of Mg-RE (Gd, Dy, Y) Alloys with Atomistic Simulation.", *Research Letters in Physics* (2008)

[46] J Wang *et al*., "Effect of Y on age hardening response and mechanical properties of Mg-xY-1.5LPC-0.4Zr alloys", *Transactions of nonferrous Metals Society of China*, 22 (2002) 1549-1555

[47] I. Stulikova, B. Smola, J. Cizek, T. Kekule, O. Melikhova, H. Kudrnova , "Natural and artificial aging in Mg-Gd binary alloys", *Journal of Alloys and Compounds*, 738 (2018) 173-181

[48] C.H Cáceres and D.M. Rovera, "Solid solution strengthening in concentrated Mg-Al alloys.", *Journal of Light Metals* 1 (3) (2001) 151-156

[49] D. Nagarajan, X. Ren, C.H. Caseres, "Anelastic behavior of Mg-Al and Mg-Zn solid solutions." *Materials Science and Engineering A,* Volume 696 (2017) 387-392

[50] L.Gao, J. ZHOU, Z. SUN, R. CHEN, E. Han, "Electronic origin of the anomalous solid solution hardening of Y and Gd in Mg: A first Principles study.", *Chinese Science Bulletin* (2011) 1038-1042

[51] K.Y. Zheng, X.Q.Zeng, J.Dong, W.J.Ding, "Effect of initial temper on the creep behavior of a Mg–Gd–Nd–Zr alloy", *Materials Science and Engineering A* 492 (2008) 185-190

[52] I.P. Moreno T.K.Nandy, J.W.Jones, J.E.Allison, T.M.Pollock, "Microstructural stability and creep of rare-earth containing magnesium alloys.", *Scripta Materialia* 48 (2003) 1029-1034

[53] B.L. Mordike, "Creep-resistant magnesium alloy.", *Materials Science and Engineering A* 324 (2002) 103-112

[54] J. Bohlen, M.R. Nürnberg, J.W. Senn, D. Letzig, S.R. Agnew, "The texture and anisotropy of magnesium–zinc–rare earth alloy sheets.", *Acta Materialia* 55 (2007) 2101-2112

[55] J. Bohlen, S. Yi, D. Letzig, K.U. Kainer, "Effect of rare earth elements on the microstructure and texture development in magnesium–manganese alloys during extrusion.", Materials Science and Engineering A 527 (2010) 7092-7098

[56] A. Kielbus, T. Rzychon, R. Przeliorz, "Oxidation Behaviour of WE54 and Elektron 21 Magnesium Alloys.", *Defect and Diffusion Forum* (2006) 312-315

[57] X. M. Wang, X.Q.Zeng, Y.Zhou, G.S.Wu, S.S.Yao, Y.J.Lai, „Early oxidation behaviors of Mg-Y alloys at high temperatures.", *Journal of Alloys and Compounds,* 460 (1–2) (2008) 368–374

[58] J. F. Fan, G. C. Yang, S. L. Chen, H. Xie, M. Wang, Y. H. Zhou, "Effect of rare earths (Y, Ce) additions on the ignition points of magnesium alloys.", *Journal of Materials Science,* 39 (20) (2004) 6375–6377

[59] R.H. Buzolin, M.Mohedano, C.L. Mendis, B. Mingo, D. Tolnai, C. Blawert, K.U. Kainer, H. Pinto, N. Hort, „As cast microstructures on the mechanical and corrosion behaviour of ZK40 modified with Gd and Nd additions.", *Materials Science & Engineering* A 682 (2017) 238-247

[60] D. Liu, D. Yang, X. Li, S. Hu, "Mechanical properties, corrosion resistance and biocompatibilities of degradable Mg-RE alloys: A review.", *Journal of Materials Research and Technology* (2018)

[61] Y.Kawamura, M. Yamasaki, "Formation and Mechanical Properties of Mg97Zn1RE2 Alloys with Long-Period Stacking Ordered Structure.", *Materals Transactions 48* (11) (2007) 2986-2992

[62] J-F. Nie, "Precipitation and hardening in magnesium alloys.", *Metallurgical and Materials Transactions A* 43 (11) (2012) 3891-3939

[63] J. Zhang, S. Liu, R. Wu, L. Hou, M. Zhang, “Recent development in high strength Mg-Re based alloys: Focusing on Mg-Gd and Mg-Y systems.”, review *Journal of Magnesium and alloys 000* (2018) 1-15

[64] T.E. Leontis, “The properties of sand cast magnesium-rare earth alloys.”, *Journal of Metals* 185 (1949) 968-983

[65] F. Feyerabend, J. Fischer, J Holtz, F. Witte, R. Willumeit, H. Drücker, C. Vogt, N. Hort, “Evaluation of short term effects of rare earth and other elements used in magnesium alloys on primary cells and cell lines.”, *Acta Biomaterialia 6* (2010) 1834-1842

[66] H. Bassett, A. Silverman, K.A. Jensen, G.H. Cheesman, J. Bernard, N. Bjerrum, E.H. Büchner, W. Feitknecht, L. Malatesta, A. Ölander, H. Remy, *Nomenclature of Inorganic Chemistry,* International Union of Pure and Applied Chemistry (1960) 5523-5544

[67] K.A. Gschneidner and Leroy Eyring, *Handbook on the Physics and Chemistry of Rare Earths* Volume 20 (1995)

[68] E.M. Savitsky and V.F. Terekhova, *Metals Science of the Rare Earth Metals,* Nauka Moscow, (1975)

[69] Y. Huang, L. Yang, S. You, W. Gan, K. U. Kainer, N. Hort, “Unexpected formation of hydrides in heavy rare earth containing magnesium alloys”, *Journal of Magnesium and Alloys,* 4 (3) (2016) 173-180

[70] M. Vlcek, J. Cizek, F. Lukac, P. Hruska, B. Smola, I. Stulikova, H. Kudrnova, P. Minarik, T. Kmjec, T. Vlasak, “Hydrogen absorption in Mg-Gd alloy”, *International Journal of Hydrogen Energy* 42 (2017) 22598-22604

[71] R. Ferro, S. Delfino, G. Borzone, A. Saccone, G. Cacciamani, “Contribution to the evaluation of rare earth alloy systems.”, *Journal of Phase Equilibria 14* (3) (1993) 273-279

[72] P.J. Apps, H. Karimzadeh, J.F. King, G.W. Lorimer, “Phase composition in magnesium-rare earth alloys containing yttrium, gadolinium or dysprosium”, *Scripta Materialia,* 48 (5) (2003), 475-481.

[73] M.G. Lentschig, P Reimer, U L Rausch-Lentschig, T Allkemper, M Oelerich, G Laub, "Breath-hold gadolinium-enhanced MR angiography of the major vessels at 1.0 T: Dose-response findings and angiographic correlation.", *Radiology. 208* (2) (1998) 353–357

[74] J.F. Nie, “Effect of precipitate shape and orientation on dispersion strengthening in magnesium alloys.” *Scripta Materialia 48* (2003) 1009-1015

[75] B. Smola, I. Stulíková, J. Pelcová, B.L. Mordike, “Significance of stable and metastable phases in high temperature creep resistant magnesium-rare earth base alloys.” *Journal of Alloys and Compounds 378* (2004) 196–201

[76] E.M. Savitskii, V.F. Terekhova, I.V. Burov, I.A. Markova, “Diagramma Sostoyaniya Splavov System Mg-Gd”, *Khim* 6 (7) (1961), 1734-1739.

[77] P. Manfrinetti and K. A. Gshneidner Jr., “Phase equilibrium in the La-Mg (0 – 65 at.% Mg) and Gd-Mg systems”, *Journal of Less Common Metals,* 123 (1-2) (1986), 267-275.

[78] T. B. Massalski, *Binary Alloy Phase Diagrams*, (Materials Park Ohio: ASM International 1990).

[79] D. Nagarajan, "Anelasticity in cast Mg-Gd alloys.", *Materials Science & Engineering A 695* (2017) 14-19

[80] G. Cacciamani, S. De Negri, A. Saccone, R. Ferro, "The Al–R–Mg (R=Gd, Dy, Ho) systems. Part II: Thermodynamic modelling of the binary and ternary systems" *Intermetallics,* 11 (11-12) (2003) 1135-1151.

[81] M. Hampl, C. Blawert, M.R. Silva Campos, N. Hort, Q. Peng, K.U. Kainer, R. Schmid-Fetzer, "Thermodynamic assessment and experimental study of Mg–Gd alloys" *J. Alloy Compd.,* 581 (2013) 166-177.

[82] S.K. Das, Y.B. Kang, TK. Ha, IH. Jung, "Thermodynamic Modeling and Diffusion Kinetic Experiments of Binary Mg-Gd and Mg-Y Systems", *Acta Materialia*, 71, 2014, 164-175*

[83] X. Tong, G. You, Y, Wang, H. Wu, W. Liu, P. Li, W. Guo, "Effect of ultrasonic treatment on segregation and mechanical properties of as-cast Mg-Gd binary alloys.", *Materials Science & Engineering A* 731 (2018) 44-53

[84] L Gao, R.S. Chen, E.H. Han, "Solid solution strengthening behaviors in Mg-Y single phase alloys*.", Journal of alloys and Compounds* 472 (2009)

[85] M Suzuki, H. Sato, K. Maruyama, H. Oikawa, "Creep deformation behavior and dislocation substructures of Mg–Y binary alloys.", Materials Science and Engineering: A (2001) 751-755

[86] X. Liu, D.Shan, Y. Song, E. Han, "The influence of yttrium element on the corrosion of Mg-Y binary magnesium alloys.", *Journal of Magnesium and alloys 5* (2017) 26-34

[87] A. C. Hänzi, P. Gunde, M. Schinhammer, P.J. Uggowitzer, „On the biodegradation performance of an Mg-Y-RE alloy with various surface conditions in simulated body fluid.", *Acta biomaterialia 5* (2009) 162-171

[88] M. Liu, P. Schmutz, P.J. Uggowitzer, G. Song, A. Atrens, "The influence of Yttrium (Y) on the corrosion of Mg-Y binary alloys.", *Corrosion science 52* (2010) 3687-3701

[89] E.D. Gibson, O.N. Carlson, Trans. ASM 52 (1960) 1084–1096.

[90] A.A. Nayeb-Hashemi and J.B. Clark, Phase Diagrams of Binary Magnesium Alloys, *American Society for Metals, Metals Park, OH,* (1988)

[91] M. Giovannini, A. Saccone, R. Marazza, R. Ferro, "The isothermal section at 500 °C of the Y-La-Mg ternary system.", *Metallurgical and Materials Transactions A* 26 (1) (1995) 5-10.

[92] H.D. Zhao, G.W. Qin, Y.P. Ren, W.L. Pei, D. Chen, Y. Guo, „The maximum solubility of Y in α-Mg and composition ranges of $Mg_{24}Y_{5-x}$ and Mg_2Y_{1-x} intermetallic phases in Mg-Y binary system.", *Journall of alloys and Componds* 509 (2011) 627-631

[93] K. Bermudez, S. Brennan, Y. H. Sohn, "Intermetallic Phase Formation and Growth in the Mg-Y System" *Magnesium technology* (2012) 145-148

[94] J. Gröbner and R. Shmid-Fetzer, "Thermodynamic modeling of the Mg–Ce–Gd–Y system.", Scripta Materialia 63 (7) (2010) 674-679.

[95] Z. Du, C. Guo, C. Li, W. Zhang, "Thermodynamic modeling of the La-Mg-Y system and Mg-based alloys database.", *Rare Metals 25* (5) (2006) 492-500

[96] C. Guo, Z. Du, C. Li, "Thermodynamic description of the Ce-Mg-Y and Mg-Nd-Y systems." *International Journal of Materials Research 99* (2008) 650-688.

[97] C. Guo, Z. Du, C. Li, "A thermodynamic description of the Mg–Pr–Y system.", *Calphad* 32 (1) (2008) 177-187.

[98] A. Kula, X. Jia, R.K. Mishra, M. Niewczas, "Flow stress and work hardening of Mg-Y alloys.", International Journal of Plasticity 92 (2017) 96-121

[99] J. Zhang, M. Xu, X. Teng, M. Zuo, „Effect of Gd addition on microstructure and corrosion behaviors of Mg–Zn–Y alloy.", Journal of Magnesium and Alloys 4 (4) (2016) 319-325

[100] F. Shi, C. Wang, Z. Zhang, „Microstructures, corrosion and mechanical properties of as-cast Mg–Zn–Y–(Gd) alloys.", *Transactions of nonferrous Metals society of China 26* (7) (2015) 2172-2180

[101] M. Giovannini, A. Saccone, H. Flandorfer, P. Rogl, R. Ferro, " On the systematics of Phase Equilibria in Complex Magnesium-Rare earth Systems: Gd-Y-Mg System." *Zeitschrift für Metallkunde 88 München Carl hanser Verlag* (1997) 372-378

[102] G. Yongchun, J. Li, J. Li, Z. Yang, J. Zhao, F. Xia, M. Liang, "Mg-Gd-Y system phase diagram calculation and experimental clarification.", *Journal of Alloys and compounds 450* (2008) 446-451

[103] C. Gao, Z. Du, C. Li, "A thermodynamic description of the Gd–Mg–Y system.", *Computer Coupling of Phase Diagrams and Thermochemistry 31* (2007) 75–88

[104] S. Pang, G. Wu, W. Liu, M. Sun, Y. Zhang, Z. Liu, W. Ding, „Effect of cooling rate on microstructure and mechanical properties of sand-casting Mg-10Gd.-3Y-0.5Zr magnesium alloy.", *Material Science and Engineering A* 562 (2013) 152-160

[105] S. Liang, D. Guan, X. Tan, L. Chen, Y. Tang," Effect of isothermal aging on the microstructure and properties of as-cast Mg-Gd-Y-Zr alloy.", *Material Science and Engineering A 528* (2011) 1589-1595

[106] T. Honma *et al.*, "Chemistry of nanoscale precipitates in Mg–2.1Gd–0.6Y–0.2Zr (at.%) alloy investigated by the atom probe technique.", *Materials Science and Engineering A 395* (2005) 301–306

[107] N. N. Greenwood and A. Earnshaw, "Chemistry of elements", *Butterworth-Heinemann Oxford* (1997)

[108] B.D. Cullity, "Element of X-ray Diffraction.", *Addison-Wesley Publishing Company* (1978)

[109] https://www.xos.com/XRD

[110] W. Reimers, A. Pyzalla, A. Schreyer, H. Clemens, “Neutrons and Synchrotron Radiation in Engeineering Materials Science, From Fundamentals to Material and Component Characterization.”, 1. *Wiley VCH Verglag Weinheim*, (2008)

[111] E. Lefshin, “X-ray Characterisation of Materials.”, *Wiley-VCH Verlg GmbH, Weinheim*, (1999)

[112] E.E. Koch, D.E. Eastman, Y. Farges, “Synchrotron radiation—a powerful tool in science, Handbook of Synchrotron Radiation”, *North-Holland Publishing Company, Amsterdam*, (1983)

[113] P. Staron, T. Fischer, T. Lippmann, A. Stark, S. Daneshpour, D. Schnubel, E. Uhlmann, R. Gerstenberger, B. Camin, W. Reimers, E. Eidenberger, H. Clemens, N. Huber, A. Schreyer, “In Situ Experiments with Synchrotron High-Energy XRaysand Neutrons.”, *Advanced Engineering Materials*, 13:658-663, (2011)

[114] W.H. Bragg and W.L. Bragg, “The reflexion of X-rays by Crystals.”, *Proc. R. Soc. London* 88 (605), (1913) 428-438

[115] https://www.pharmatutor.org/pharma-analysis/structure-of-organic-compounds-applications-of-x-ray-diffraction-spectroscopy

[116] C. Kittel, “Introduction to Solid State Physics.”, 3rd edition *New York: John Wiley & Sons*, (1966)

[117] W. H. Zachariasen, “Theory of X-Ray Diffraction in Crystals.”, *New York: Dover*, (1967).

[118] T. Ungár, “Microstructural parameters from X-ray diffraction peak broadening.”, *Scripta Materialia 51*(2004) 777-781

[119] D. Tolnai, P. Townsend, G. Requena, L. Salvo, J. Lendvai, H.P. Degischer, “In situ synchrotron tomographic investigation of the solidification of an AlMg4.7Si8 alloy”, *Acta Materialia* 60 (6-7) (2012) 2568-2577

[120] S. Shuai, E. Guo, A.B. Phillion, M. Callaghan, T. Jing, P.D. Lee, “Fast synchrotron X-ray tomographic quantification of dendrite evolution during the solidification of Mg-Sn alloys.”, *Acta Materialia* 118 (2016) 260-269

[121] Y. Miao, K. Mo, Z. Zhou, X. Liu, K.C. Lan, G. Zhang, M. K. Miller, K. A. Powers, J. Almer, J. F. Stubbins, “In situ synchrotron tensile investigations on the phase responses within an oxide dispersion-strengthened (ODS) 304 steel.”, *Materials Science and Engineering A*, 625 (2015) 146-152

[122] P. Erdely, P. Staron, E. Maawad, N. Schell, H. Clemens, S. Mayer, “Lattice and phase strain evolution during tensile loading of an intermetallic, multi-phase γ-TiAl based alloy.”, *Acta Materialia* (2018) 193-205

[123] S. Hanke, P. Staron, T. Fisher, V. Fitseva, J.F. Santos, “A method for the in-situ study of solid-state joining techniques using synchrotron radiation - observation of phase transformations in Ti-6Al-4V after friction surfacing. “ *Surface and Coatings Technology* 335 (2018) 355-367

[124] S.S. Babu, J.W. Elmer, J.M. Vitek, S.A. David, "Time-resolved X-ray diffraction investigation of primary weld solidification in Fe-C-Al-Mn steel welds", *Acta Materialia* 50 (2002) 4763-4781

[125] O. Shuleshova, D.H. Moritz, A. Voss, W. Löser, *Intermetallics* 19 (2011) 688-692

[126] D. Tolnai, G. Szakács, G. Requena, A. Stark, N. Schell, K.U. Kainer, N. Hort, "Study of the Solidification of AS Alloys Combining In Situ Synchrotron Diffraction and Differential Scanning Calorimetry.", *Materials Science Forum* 765 (2013) 286-290

[127] B. Wiese, C.L. Mendis, D. Tolnai, A. Stark, N. Schell, H-P. Reichel, R. Brückner, K.U. Kainer, N. Hort, "CaO dissolution during melting and solidification of a Mg-10 wt.% CaO alloy detected with in situ synchrotron radiation diffraction." *Journal of Alloys and Compounds 618* (2015) 64-66

[128] D. Tolnai, C.L. Mendis, A. Stark, G. Szakács, B. Wiese, K. U. Kainer, N. Hort, "In Situ Synchrotron Diffraction of the Solidification of Mg-RE Alloys", *Magnesium Technology 2013* (2013) , Pages 253-257

[129] D. Tolnai, C.L. Mendis, A. Stark, G. Szakács, B. Wiese, K.U. Kainer, N. Hort, "In situ synchrotron diffraction of the solidification of Mg4Y3Nd.", *Materials Letters* Volume 102-103, (2013) 62-64

[130] N. Iqbal, N.H. van Dijk, S.E. Offerman, M.P. Moret, L. Katgerman, G.J. Kearley, "Real-time observation of grain nucleation and growth during solidification of aluminium alloys.", *Acta Materialia*, 53 (2005) 2875-2880

[131] W. J. Boettinger, J. A. Warren, C. Beckermann, A. Karma, "Phase-field simulation of solidification", *Annual Review of Materials Scie,* 32 (2002) 164-19

[132] G. Szakács, B. Wiese, C.L. Mendis, D. Tolnai, A. Stark, N. Schell, M. Nair, K.U. Kainer, N. Hort, "In Situ Synchrotron Radiation Diffraction during Solidification of Mg4Y and Mg4YxGd Alloys (x = 1, 4 wt. %)." *Magnesium Technology 2014* (2014) pages 213-218

[133] F.R. Elsayed, N. Hort, M.A. Salgado-Ordorica, K. Kainer, „Magnesium Permanent Mold Casting Optimization.", *Material Science Forum 690* (2011) 65-68

[134] Rueden, C., Dietz, C., Horn, M., Schindelin, J., Northan, B., Berthold, M. & Eliceiri, K. (2016). ImageJ Ops [Software]. http://imagej.net/Ops.

[135] https://www.mt.com/de/en/home/products/Laboratory_Analytics_Browse/TA_Family_Browse/Crucibles/High_Pressure.html#overviewpl

[136] http://www.perkinelmer.com/pdfs/downloads/009299B_01%20PRD.pdf

[137] http://www.esrf.eu/computing/scientific/FIT2D/index.html

[138] P. Villars, and K. Cenzual, Pearson's Crystal Data — Crystal Structure Database for Inorganic Compounds (on CD-ROM), Ohio: ASM International, Materials Park, USA, Release 2012

[139] G. Szakács, C.L. Mendis, D. Tolnai, A. Stark, N. Schell, H. Ovri, M. Wolff, K. U. Kainer, J. Gröbner, R. Schmid-Fetzer, N. Hort, "In situ synchrotron radiation diffraction during

solidification of Mg15Gd: effect of cooling rate.", *Magnesium Technology 2015* (2015) pages 79-78

[140] J. Gröbner, S. Zhu, J.F. Nie, M.A. Gibson, R. Schmid-Fetzer, "Metastable phase formation in ternary Mg-Gd-Zn alloys." *Journal of alloys and compounds* 675 (2016) 149-157

[141] J. Gröbner, A. Kozlov, X.-Y. Fang, S. Zhu, J.-F. Nie, M.A. Gibson, "Phase equilibria and transformations in ternary Mg-Gd-Zn alloys.", Acta Materialia 90 (2015) 400-416

[142] G. Szakács, C. L. Mendis, D. Tolnai, M. Vlcek, F. Lukác, I. Stulíková, B. Smola, M. Wolff, R. Schmid-Fetzer, N. Schell, K.U. Kainer, N. Hort, "As Solidified Microstructure Investigation of Mg15Y and MgxYyGd (x+y=15wt.%) Ternary Alloys.", *Magnesium Technology 2016* (2016) 23-27

[143] D. Tie, F. Feyerabend, N. Hort, D. Hoeche, K.U. Kainer, R. Willumeit, W.D. Mueller, "In vitro mechanical and corrosion properties of biodegradable Mg-Ag alloys." *Materials and corrosion 65* (6) (2014) 569-576